Decay studies of proton-rich nuclei in the mass 70 region and investigating their effects on the astrophysical rp-process

Laura Sinclair

Doctor of Philosophy

University of York
Physics

September 2016

Dedication

"I love you."

"Me too."

For Steven Lomax and

Bill 'Sparky' Lomax.

Abstract

Proton-rich A$\sim$70 nuclei have been subject to many experimental investigations due to their accessibility since the advent of radioactive ion beams and improved experimental developments in sensitive tagging techniques. Nuclear structure data in this region are also of astrophysical significance since the (rapid proton capture) *rp*-process, which is believed to take place in X-ray bursts, occurs in the vicinity of the N=Z line, with rapid proton-capture chains and subsequent β-decays allowing for the seeding of heavy elements in the A$\approx$ 100 region. Therefore the structure and decay properties of N $\approx$ Z nuclei can have an impact on *rp*-process reaction rate calculations.

The nuclide ^{72}Kr, with a β-decay half-life of 17.1(2) s, is a potential waiting point of the *rp*-process. However, its lifetime in a stellar environment is reduced by the two-proton capture reaction ^{72}Kr(p,γ)^{73}Rb(p,γ)^{74}Sr. One of the main goals of the experiment was to measure the proton-separation energy, S_p, of ^{73}Rb, by extracting the β-delayed spectrum following the decay of ^{73}Sr. To gain a complete picture of the two-proton capture branch for the ^{72}Kr waiting point in the *rp*-process the half-life of ^{74}Sr needs to be measured.

An experiment was carried out at the Radioactive Isotope Beam Factory, RIKEN. The nuclei of interest were produced by the fragmentation of a 345 MeV/nucleon ^{124}Xe beam on a 555 mg/cm^2 ^{9}Be target. The effects of the half-lives and proton-separation energy measured, in this work, on the effective lifetime of ^{72}Kr have been explored using one-zone, one-dimensional reaction network calculations for the astrophysical *rp*-process. At the proton drip-line, a search for new isotopes and the nature of the decay of ^{76}Y was conducted. The location of the drip line is of important interest for the *rp*-process. An estimate of the half-life and an upper limit of the half-life for ^{72}Rb and ^{73}Rb have been determined, respectively. Following these measurements, proton emission calculations have been performed by L.S. Ferreria and E. Maglione and the results are discussed in this work.

Contents

List of Figures

List of Tables

Acknowledgements

As I was writing my acknowledgement section, I realised how incredibly lucky I am to have such a great support network. I would like to thank everyone who has supported me during my postgraduate studies at York, and apologies if I have not named you.

Bob Wadsworth. A great man and supervisor. One who has encouraged me throughout my PhD, and allowed me to ask any question, no matter however trivial. He encouraged me to think through problems in detail and gave me the opportunity to explore various places around the world. None of this would have been possible without him.

A big thank you to my collaborator Giuseppe Lorusso. The man who thought up an interesting experiment. Giuseppe gave me the opportunity to learn first hand about the experimental set up and data analysis, and he gave me so much of his time. Working lunches and dinners were definitely needed. His enthusiasm for physics is second to none, and he truly appreciates the beauty of physics and research.

Thank you to Paul Davies for all of his hard work, from working over 20 hours straight on the actual thesis experiment, to guiding me throughout the PhD. His input on data analysis has been invaluable.

Philip Adsley has provided much physics, career and life advice. He is a man truly passionate about physics, and he is a source of inspiration. Thank you to Frank Browne for our near daily conversations; his encouragement, support and input have definitely kept me going. Dunc, my travel buddy and a great friend. Thank you for our long discussions about proton emission calculations often starting in a coffee shop and ending up in the pub.

My time at RIKEN was a special part of my life. The IPA team: Simon, Daniel and Zena, the staff: P-A, Pieter and Shunji - they all made it an incredible experience. My six months at RIKEN gave me time to grow as a person and a physicist. I would like to give a honourable mention to Team WAS3ABi of Xu, Wu, and Lucy.

I was very lucky to have the opportunity to do a second long-term attachment at the

University of Jyväskylä, learning how to assemble the vacuum-mode separator MARA and participating in many experiments. The staff and students there were kind and welcoming. I met some truly incredible people from the ERAMUS/international community. Special honours to Dajana (my Balkan sister), George, Jörg and Giovanni.

The support of my family has been invaluable. My Mum is the strongest person I know, with the biggest heart. Without her none of this would have been possible. My little brother, Stuart, who is the most funny, smart and brilliant person I know, thank you for everything, I could not ask for a better brother. To my Dad, who I love dearly and who has spent many years driving me around the country for sport and hobbies. Bill, who sadly did not get to see me finish my PhD, treated me like one of his children and may have boasted about me more than my mum does (and that is *a lot*). Thank you to my Gran, the head of the family. She took me in whenever I needed it, made brilliant cups of tea (and bacon sandwiches) and gave me her love. The support of my (rather large) family has been incredible and I appreciate the role everyone has played.

To my friends: for their love and support, for their time and just for being such incredible people and a source of inspiration. In no particular order: Amelia, who has been an incredible friend for many years, who pushes me to better myself as a person in many different ways, thank you for welcoming me with open arms into your life. To my Manchester friends Lexie, Claire, Lauren, Fiona and Peter; despite not living in the same city or country or continent for many years we have remained close. Even as our lives have evolved, you have continued to play a huge role in life. My Kristina, a kind hearted and great friend, who never fails to make me laugh. Thank you to Anna, who helped me secure my dream job and for her support over the years. Thank you to my hiking buddies Emily, Szonja, David and Thöm, my friends who have endured me, even when I arranged trips to walk many miles, often in the rain without a map. To Bren; thank you for everything. Thanks to my York friends Nic, Abby, Keith, Stephen, Jennifer and Monther.

Laura Clark (*a superstar*), Annika, Dan, Leendert, Lucy and Chris Abel: your suggestions and support are much appreciated, and I owe you much. Lastly, I would like to thank Chris McPeake and Jan for all of their support and encouragement over the years.

Declaration

The work in this thesis was performed at the University of York, supervised by Prof. B. Wadsworth. Additionally, research was undertaken in extended research visits to Nishina Centre, RIKEN. I declare that the work presented in this thesis has not been submitted previously for a degree in this or any other university. All sources are acknowledged as references.

Chapter 1

Introduction and motivation

The nucleus is a quantum many-body system of a finite size, consisting of two distinct types of fermion (protons and neutrons), and interacts via the strong, electromagnetic and weak forces. Protons and neutrons, as fermions, must obey the Pauli exclusion principle, meaning that no two protons, or two neutrons, may occupy the same quantum state. To date, over 2500 nuclei have been produced and studied, 300 of which are stable nuclei. It is suggested there could be as many as an additional 5000 unique nuclei [1]. Nuclei can be pushed to many limits, in terms of the number neutrons and protons that can make up a nucleus of a given mass. The exploration of the chart of the nuclides is moving far from the so-called "valley of stability" and towards the so-called drip-lines which represent the limits of proton-neutron imbalances. Since the advent of radioactive ion beam (RIB) production, physicists have been able to further the boundaries of experimentally accessible nuclei further. This has pushed exploration towards more proton-rich and more neutron-rich at the drip-lines and to the extremes of isospin. By exploring the properties of these nuclei, a greater understanding of the nuclear force, nuclear astrophysics and the formation of the elements can be obtained.

There are two important features present in nuclear structure, these being collective effects and single-particle (SP) effects. The concept of nuclear shell structure was triggered by the observation of particularly stable nuclei with specific proton and neutron numbers, analogous to that of the shell structure in atomic physics. Close to the line of stability, nuclei with neutron, N, and proton, Z, numbers of; 2, 8, 20, 28, 50, and 82 (and 126 for neutrons) are known as the magic numbers, at which large gaps in the single-particle energy spectra occur near the Fermi energy. For doubly magic numbers, the nucleus is spherical, but between the magic numbers the nuclei are generally deformed, the majority

of them being prolate (rugby-ball shaped) [2] and a minority being oblate (smartie shaped). The single-particle effect is dominant in near-spherical nuclei, occurring in the presence of a strong spin-orbit interaction. Collective effects are expected to dominate in deformed nuclei.

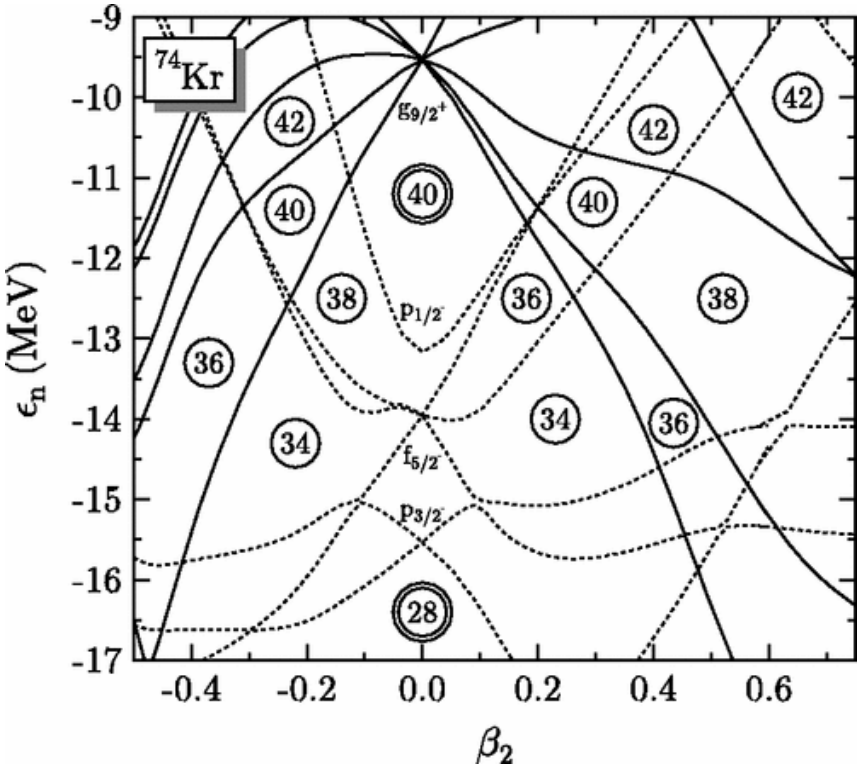

Figure 1.1: Nilsson plot of neutron single-particle energies, with positive parity (solid lines) and negative parity (dotted lines) as a function of the intrinsic mass deformation $\beta_2^{(i)}$, as obtained for ^{74}Kr. Negative deformation is oblate and positive deformation is prolate. Figure reproduced from [3].

In the neutron deficient mass 70 region, which lies midway between the spherical ^{56}Ni and ^{100}Sn nuclei, large single-particle energy gaps exist at nucleon numbers of 34 and 36 (oblate), 34 and 38 (prolate) and 40 (spherical). Oblate, prolate and, in some cases spherical shapes are predicted to coexist within a very small energy range of a few hundred keV for some nuclei in the N, Z = 30-40 region [4]. The close proximity of the competing energy minima makes it difficult to calculate the ground state shapes of nuclei, leading to discrepancies for theoretical predictions. These gaps are key drivers for nuclear shape co-existence which is known to be present in the region. The A$\sim$70, N=Z region of the nuclide chart, where valence nucleons may occupy the *fpg* shell. This is of interest due to the

deformation-driving effects of the $g_{9/2}$ intruder orbital [5, 6]; the $g_{9/2}$ orbital intrudes into the fp negative-parity orbitals for both prolate and oblate deformed shapes (see Fig. 1.1). This gives more stability to deformed shapes and has a role in increasing collectivity as the mid-shell point, located between the closed shell regions of (N,Z) 28, 28 and (N,Z) 50, 50 is approached. These nuclei are predicted to have a large quadrupole deformation in their ground state [7].

Protons and neutrons can fill identical orbitals for N=Z nuclei. As the nucleons sit in the same orbital, leading to the possibility of strong neutron-proton interactions due to maximum spatial overlap of the wave-functions.

Nuclear structure is also of astrophysical significance. The rapid-proton (rp) capture process, thought to take place in X-ray bursts, occurs in the vicinity of the N=Z line, with rapid proton-capture chains and subsequent β-decays allowing for the seeding of heavy elements in the A$\approx$ 100 region. Therefore, the structure of N $\approx$ Z nuclei can have impact on rp-process reaction rate calculations.

Therefore, A=70–80, N=Z nuclei provide a good opportunity to investigate shape coexistence and np-pair correlations. The A=70–80 region is of special interest due to the rapid shape changes that can occur as a function of nucleon number, with strong shape coexistence expected which other N=Z regions are less prone to. There are limited data for N<Z nuclei in the fpg shell region for A=60 and upwards. Therefore, detailed experimental spectroscopic information is vital in order to deduce the actual shapes of nuclei and also determine the degree of shape mixing. Hence, there is an urgent need for more experimental work in this mass region to help distinguish between the various models.

1.1 Radioactive ion beam facilities

State-of-the-art radioactive beam facilities, such as the RIKEN Radioactive Isotope Beam Factory (RIBF) at the Nishina Center, Japan, allow access to some nuclei for the first time in human endeavour, meaning that information on binding energies, excited state structures and β-decay half-lives can be discerned for isotopes. Two methods of particular use in RIB facilities are Isotope Separation On Line (ISOL) [8] and in-flight separation [9]. The method of in-flight separation was used for the present work. Projectile fragmentation is a reaction mechanism which is used to produce highly exotic nuclei. In this process a primary beam of nuclei is accelerated to high energies (hundreds of MeV/u) and fired into

a light target, typically Beryllium or Carbon; the beam is fragmented into smaller nuclei with some nucleons being knocked out of the beam nucleus. Using this fragmentation technique, and other similar reactions, nuclei very far from stability can be accessed [10].

1.2 Nuclear structure

Many of the nuclei of interest that were produced in this work are self-conjugate (N=Z) exotic nuclei, at or very close to the limits of binding i.e. they lie at the proton drip-line. The aims of experimental investigations in medium-mass self-conjugate nuclei are to answer questions about deformation, shape coexistence, neutron-proton pairing and isospin symmetry.

1.2.1 Isospin symmetry

In the early 20^{th} century it became clear that the nuclear force acted similarly on protons and neutrons. Heisenberg [11] proposed treating protons and neutrons as two quantum states of a particle called the nucleon. The near identical behaviour of protons and neutrons in the nuclear potential gives rise to the quantum number associated with this, called *isospin*, with the value T, formalised by Wigner [12]. The isospin quantum number is analogous to the spin quantum number. The projection of the isospin on the z-axis is characterised as t_z = -1/2 for protons and t_z = +1/2 neutrons.

The nucleon's isospin state is determined by the projection in an abstract space, known as the isospin space. Isospin symmetry is the exchange symmetry between protons and neutrons, with an associated isospin quantum number, T. The isospin of a nucleus is given by the vector sum of the single nucleon isospin. In a nucleus formed from neutrons, N and protons, Z, the total projection is T_z = (N-Z)/2. States of the same isospin in nuclei with the same mass number are named isobaric analogue states (IAS).

The impact of isospin is expected to be maximal near the N=Z line and the charge symmetry can be investigated by looking at the IAS. The energy differences between IAS occur as a result of isospin non-conserving forces, such as the Coulomb interaction as explained by Ref. [13]. The ground state of odd-odd N=Z nuclei should be $T = 0$, however the $T = 1$ structure can be lowered such that the ground state becomes $T = 1$. Two types of state coexist near the ground state; particles coupled with space/spin symmetry and isospin antisymmetry $T = 0$ states, or particles coupled with space/spin antisymmetry

and isospin symmetry $T = 1$ states.

A consequence of isospin symmetry is the considerable similarity of the structure of mirror nuclei - nuclei with the number of protons and neutrons interchanged. Isobaric sets of nuclei with $T_z = -1, 0$ and 1, known as isobaric triplets, must all have $T = 1$ states with almost identical properties due to isospin symmetry. In-depth information regarding isospin symmetry breaking effects can be obtained through detailed knowledge of Coulomb energy differences (CEDs) between IAS for members of the same triplet [13].

1.2.2 np-pairing

The Pauli exclusion principle does not prevent a proton and a neutron from occupying the same space-spin orbital and forming a *pn* Cooper pair, see Ref. [14], if they are coupled to T=0 [15] as shown in Fig. 1.2b. N=Z nuclei are unique in that strong neutron-proton T=0 pairing can occur. In non-N=Z nuclei the pairing of nucleons is dominated by like-nucleons, i.e. T=1 pairing. In N=Z nuclei the *np*-pairing is predominately between neutrons and protons. However, it is still possible for some *np*-interaction effects to play a role in nuclei close to the N=Z line.

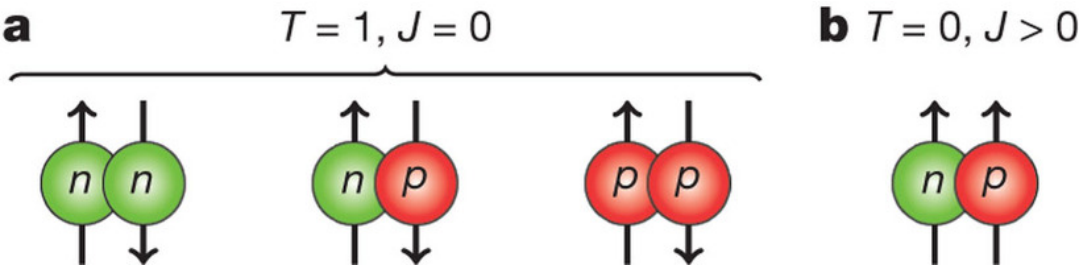

Figure 1.2: Schematic diagram illustrating the possible pairing schemes in nuclei. a) The possible pairings leading to isospin $T = 1$ and $J = 0$. Due to the Pauli exclusion principle the isovector components are restricted to spin zero. b) The neutron-proton pairing leading to $T = 0$ and $J>0$. This is due to the Pauli exclusion principle, which will only allow for non-zero components of angular momentum. Figure reproduced from [16]

For *np*-pairing, two configurations are possible, as seen in Fig. 1.2. Of key interest at the present time is the isoscalar pairing (i.e. $T = 0$, $J = 1$), where the nucleons can couple to give a final spin ranging from 1 to J_{max}. At present there is limited experimental evidence for the effects of *np*-pairing or *np*-interactions. The pair types for *np*-pairing can yield $T = 1$, $J = 0$, and $T = 0$, $J = 1$ (or more up to the maximum for the pair) states,

e.g. for a $g_{9/2}$ pair, J can run from 1 to 9.

The first indications of the importance of the maximal spin-aligned np pairs in the mass 90 region at low-spin was suggested in ^{92}Pd [16]. Evidence for the presence of strong isoscalar np-interaction has been revealed through the observation of a spin-gap isomer[1] in ^{96}Cd [17] and studies of ^{94}Pd decay [18]. It is expected that isoscalar (T=0) np-pairing is important in all N=Z nuclei. However, its role in the A=70–80 region is not yet clear. In this region, calculations suggest that $T = 1$ np-pairing will dominate (i.e. less effect from the T=0 np-pairing) [15, 19]. There is a long standing question over the effects of $T = 0$ np-pairing on the structure of such nuclei [15, 20].

1.2.3 Deformation

It was suggested in 1953 that the nucleus could be considered to be a highly compressed liquid drop which undergoes quantised vibrations and rotations. Rotational motion can be observed in nuclei with non-spherical equilibrium shapes [21]. These nuclei can have substantial distortions from a spherical shape and are often described as deformed [21]. It can be imagined that if the nucleus has x-axis symmetry, and can rotate around the y-axis and the z-axis. In addition to this it may oscillate from prolate to oblate as well as vibrate [22]. The collective model[2] provides a good description of even-even deformed nuclei [22].

The coupling between collective vibrations and degenerate excitations of individual nucleons plays an important role in inducing nuclear ground state deformation. In nuclei, pairing correlations[3], see Ref. [23], can also compete with the deformation driving particle-vibration coupling [24]. Rotational excitations can only occur in deformed nuclei. The deformation parameter, β, is related to the eccentricity of the resulting ellipsoid:

$$\beta = \frac{4}{3}\sqrt{\frac{\pi}{5}}\left(\frac{\Delta R}{R_{av}}\right), \tag{1.1}$$

in which, $R_{av}=R_0A^{1/3}$ is the average radius and ΔR is the difference between the semi-major and semi-minor axis. For $\beta > 0$ the nucleus is prolate, for $\beta < 0$ it is oblate and

[1] A spin gap is believed to occur due to a large difference in the spins between the isomeric state the states below it.

[2] The collective model combines the liquid drop model and shell model to explain magnetic and electric properties of nuclei.

[3] There is evidence for pairing correlations including the oddeven staggering in drip-line nuclei.

for $\beta = 0$ it is spherical.

1.2.4 Shape coexistence

The atomic nucleus has the ability to minimise its energy by adopting different deformed nuclear shapes [25], as mentioned in the previous section. In nuclei there are the various arrangements of the nucleons [26]. The arrangements involve sets of energy eigenstates with different electric quadrupole moments and transition rates [26] and the distributions of proton pairs and neutrons pairs with respect to their Fermi energies. As a consequence of deformation, this can lead to competing minima in the nuclear potential energy surface residing very close together in some nuclei.

Establishing a nuclear energy level scheme may give circumstantial evidence in favour of shape coexistence, but a complete picture can only be obtained from nuclear matrix elements [27]. Shape coexistence in the Z∼34, N∼40 region extends from the stability line to the proton-drip line [26]. The study of this region has been difficult because the features are not as distinctive as in other regions of the nuclear chart. This may be due to the presence of strong shape mixing [26]. Shape coexistence in this region of interest was first proposed in ^{72}Se [28]. The role of sub-shells, in this region, is becoming evident as an important feature for understanding shape coexistence and collectivity [26]. The work in Ref. [4] provides direct experimental evidence of shape coexistence in the A∼70 region for even-A Kr isotopes. Also, the work of Ref. [29] identified the second 0^+ state in ^{72}Kr, which is believed to be a prolate state, whilst the 0^+ ground state is expected to be oblate. The mean-field describes a potential U, which is experienced by all nucleons. In Ref. [4], it was found that the prolate and oblate minima are almost degenerate and there is no sharp minimum for either shape (oblate and prolate). This implies that the calculations do not predict a well-defined prolate or oblate shape for the ground states of ^{72,74,76,78}Kr, thus suggesting shape coexistence and the presence of strong shape mixing.

1.3 Nuclear structure at the proton drip-line

As one moves away from the valley of stability towards more and more neutron-deficient nuclei, (i.e. decreasing the numbers of neutrons) the binding energy of the last proton, (proton-separation energy) S_p, decreases. The border between bound and unbound systems for the proton drip line is determined by the change in sign of the proton-separation

energies, i.e. the proton drip-line is crossed when S_p becomes negative. At the proton drip line, the potential barrier can help confine the protons, which in turn can impact on proton emission. However, when the penetration probability is large enough, proton emission can compete with β-decay. Due to Coulomb repulsion, the proton drip line lies closer to the valley of β stability when compared to the neutron drip line. For almost all elements up to protactinium (Z = 91), the proton drip line has been reached for odd-Z elements [30]. Beyond the drip line (S_p¡0) a considerable number of proton emitters have been observed [31–34]. Measuring proton emission can allow one to study nuclear structure, even beyond the proton drip line. Information can be extracted on the nuclear wave-function, and can serve to constrain nuclear mass models, see Refs. [35,36] for further detail.

1.4 Nuclear astrophysics

Results of investigations in the mass 70 N≈Z region can have implications for the astrophysical rapid proton-capture (*rp*)-process. Type I X-ray bursts provide the necessary conditions for the *rp*-process. Once breakout from the hot-CNO cycle is reached, at T_9 (GK) >0.8, nuclear burning occurs via a series of (p,γ) reactions (the *rp*-process), (α,p) reactions (the αp-process) and β^+-decays. Rapid proton-capture chains and subsequent β-decays allow for the seeding of heavy elements to extend up to the A∼100 region. The details of these will be discussed in the following sections.

1.4.1 Type I X-ray bursts

In 1976, the discovery of X-ray binaries was reported by Grindlay *et al.* [38] and Belian *et al.* [39]. Space observatories were required to view the emissions of these high-energy photons. Type-I X-ray bursts occur in low-mass X-ray binary systems, where a neutron star and a low-mass main sequence star are in a binary system [40–43]. Type I X-ray bursts are characterised by large increases in the X-ray flux from neutron star binary systems. Due to the close proximity of the neutron star and the companion star, and the intense gravitational field of the neutron star, the companion star overflows its Roche lobe[4]. Therefore, Hydrogen- and Helium- rich matter from the outer layers of the companion star

[4]The Roche limit is the minimum distance in which the smaller body, held together by its self-gravity, can orbit a larger body.

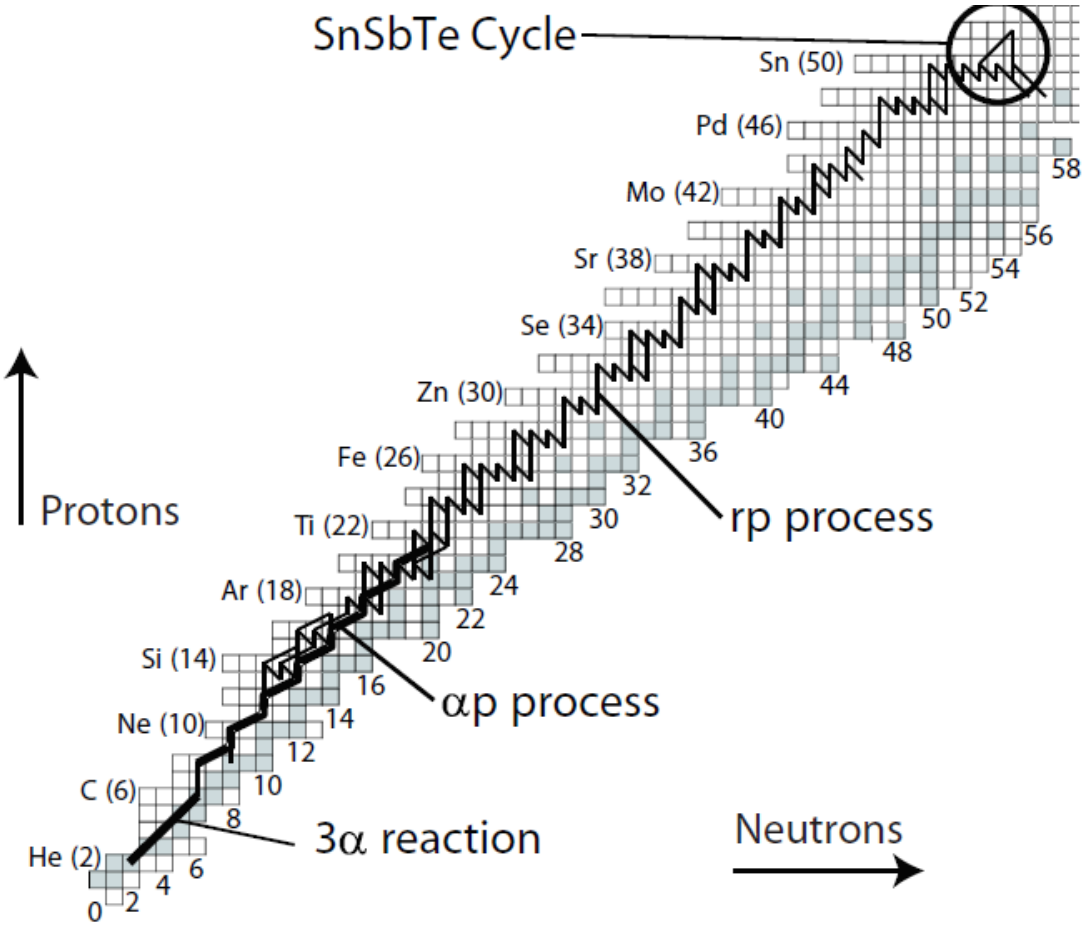

Figure 1.3: An illustration of the triple α-process, breakout from the hot-CNO cycle, (α,p) reactions (the αp-process), and (p,γ) reactions and β^+-decays (*rp*-process). Note the endpoint of the *rp*-process with Sn-Sb-Te cycle. Figure reproduced from [37].

are drawn into an accretion disk around the neutron star [44]. The temperature of the atmosphere rises until the temperature is high enough to cause thermonuclear runaway, at T_9 >0.5, releasing a sudden burst of X-rays.

In X-ray bursts, thermonuclear runaway is triggered by the 3α reaction which is strongly temperature-dependent. The breakout from the HCNO-cycle occurs via ^{14}O(α,p) and ^{18}Ne(α,p)^{21}Na. The thermonuclear runaway proceeds via the αp-process, a sequence of (α,p) and (p,γ) reactions up to ^{41}Sc. The αp-process provides seed nuclei for the *rp*-process and then continues up to ^{56}Ni. Fig. 1.3 displays the evolution of reactions in an X-ray burst.

An artists' impression of an accretion environment is shown in Fig. 1.4. Matter slowly accretes onto the surface of the neutron star, forming an electron degenerate atmosphere

Figure 1.4: An artist's impression of an X-ray burst environment. Figure reproduced from [45]. Type I X-ray bursts are thermonuclear explosions in the atmosphere of a neutron star. The *rp*-process begins with the accretion of Hydrogen and Helium rich matter onto a neutron star (left hand side) from nearby companion star (right hand side).

on the surface. A neutron star has a typical mass of 1.4 $M_\odot$, a radius of between 10 and 20 km, and a density of the order of 10^{14} g/cm^3. The companion star is typically metal poor with a mass of 1.5 $M_\odot$ or less. Burst duration can range between tens and hundreds of seconds, with temperatures ranging from 1 to 1.5 GK. The X-ray burst process is recurrent; when the burst is over, the binary system will return to a quiescent state. The neutron star will once again accumulate Hydrogen and Helium and the process is repeated. Understanding the mechanism of X-ray bursts provides information about the neutron stars involved [37], and is crucial to determining the relative abundances of stable isotopes formed during the burning process. The tail of the burst peak is typically long relative to the rise time indicating explosive ignition and the gradual consumption of Hydrogen as the burst proceeds. This leaves the light-curve as the only feasible observable to probe the behaviour of the X-ray burst. A question is, although not likely [46] due to

the gravitational fields of the neutron star, do X-ray bursts contribute to observed galactic isotopic abundances by ejecting matter during bursts?

1.4.2 The *rp*-process

The *rp*-process involves a sequence of fast proton radiative captures (p,γ) and β^+-decay (β^+,ν) reactions beginning at ^{41}Sc and is responsible for nucleosynthesis on the proton-rich side of the valley of stability up to A$\sim$100 [44]. This proceeds through the exotic mass region, close to the proton drip-line. Fig. 1.5 displays an illustration of the *rp*-process. The *rp*-process requires a high temperature (i.e. T_9>1) environment, with a large proton flux to progress.

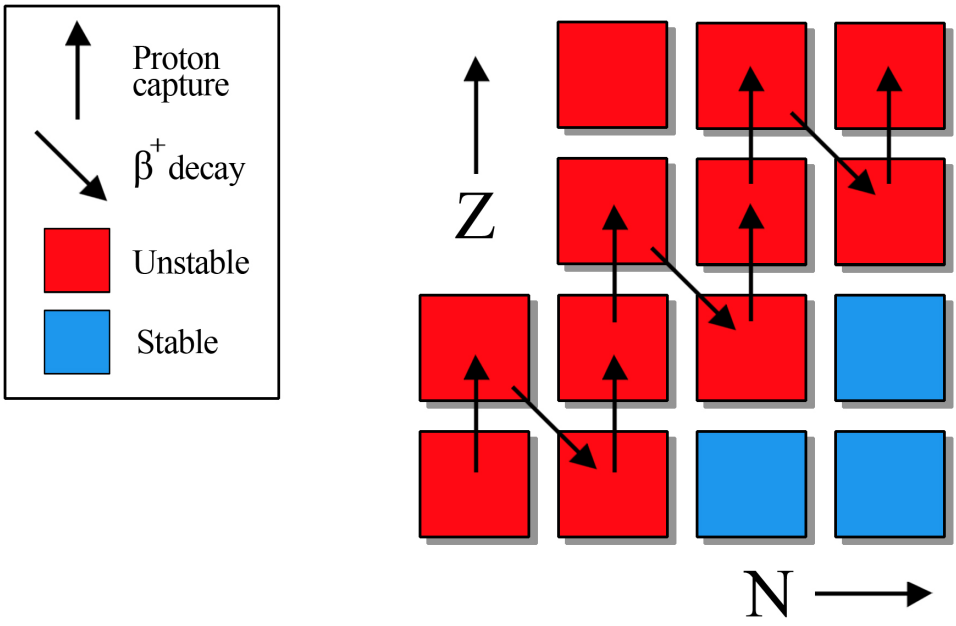

Figure 1.5: An illustration of the *rp*-process. The rapid, consecutive proton captures result in a progression to higher masses. When proton capture becomes inhibited, the process must progress either through a β-decay or the near prompt capture of two consecutive protons. Figure from [47].

Depending on the parameters and ignition conditions of the X-ray burst, state-of-the-art reaction network calculations suggest that the *rp*-process can extend into A$\sim$100 [48], with an endpoint of the Sn-Sb-Te cycle [49], where the process ends due to the nuclei becoming α-unbound. Detailed reaction rates depend on nuclear structure, nuclear masses

and the lifetimes of relevant nuclei for such calculations [50].

1.4.3 Waiting points

The nucleosynthesis path is controlled by waiting points, where photo-disintegration rates and capture rates are equal and therefore wait for β^+-decay to occur. The waiting points' β^+-decay half-lives are on the timescale of the duration of the X-ray bursts and therefore, determine the rate of nucleosynthesis and isotopic abundances in the *rp*-process. Network calculations [44] indicate that the even-even N=Z nuclei nuclei, such as ^{64}Ge, ^{68}Se and ^{72}Kr, beyond ^{56}Ni represent the major waiting points. Usually, waiting point nuclei have even-Z, as the odd-Z nucleus following a proton capture is not as well-bound [51]. Along the reaction path of the *rp*-process, β^+-decay half-lives, nuclear masses and proton-separation energies for the unbound nuclei determine the processing timescale and final composition.

The nuclide ^{73}Rb is thought to be proton-unbound [52], hence one-proton capture is not a possible pathway out of ^{72}Kr for the *rp*-process, making ^{72}Kr a potential waiting point [44]. However, due to the Coulomb barrier and angular momentum barrier, the half-lives of proton unstable nuclei can be long enough for rapid successive two-proton capture to occur. Such a reaction could effectively bypass the waiting point nuclei, thereby reducing the half-life of the A=72 bottleneck. Fig. 1.6 represents two-proton capture on ^{72}Kr.

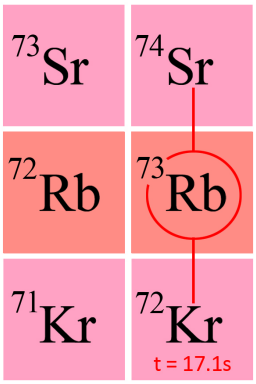

Figure 1.6: An illustration of the two-proton capture on ^{72}Kr. Although ^{73}Rb is expected to be proton-unbound, two-proton capture may be possible. If two-proton capture is not possible then the *rp*-process is forced to wait for the slow β-decay of ^{72}Kr ($T_{1/2}$=17.1(2) s [53]). Figure from [47].

The nuclide ^{68}Se is also a potential waiting points, with ^{69}Br being proton unbound.

In recent years direct measurements of S_p for ^{69}Br have been performed by break-up and β^+-decay measurements [54, 55]. As a result, the status of ^{68}Se as a waiting point is now known [56, 57]. The masses of ^{68}Se [58] and ^{72}Kr [59] have been measured to high precision with Penning traps.

The two-proton capture reaction introduces a large uncertainty into the reaction network calculation because the reaction rate depends on the proton-separation energy, S_p, of ^{73}Rb. To constrain the rate of the reaction of ^{72}Kr(2p,γ)^{74}Sr in X-ray burst conditions, knowledge of the proton separation energy, S_p, of ^{73}Rb is needed.

1.5 Thesis overview

This thesis reports decay studies of nuclei in the A$\sim$70 proton-rich region were the subject of investigation in the RIBF97 experiment, conducted at the RI Beam Factory (RIBF), operated by the RIKEN Nishina Center. The region of the nuclear chart involved for the mass 70 region is shown in Fig. 1.7.

One of the main aims of the present work was to measure the proton-separation energy (S_p) of ^{73}Rb and to determine the lifetimes of nuclei beyond the N=Z line. The nuclide ^{72}Kr, with a β-decay half-life of 17.1(2) s [53], is a potential waiting point of the astrophysical *rp*-process. However, its lifetime in a stellar environment is significantly reduced by the two-proton capture reaction ^{72}Kr(p,γ)^{73}Rb(p,γ)^{74}Sr, whose reaction rate is highly sensitive to the characteristics of the low-energy states of the intermediate nucleus, ^{73}Rb, and in particular to the proton-separation energy of ^{73}Rb. The present best estimate for the S_p of ^{73}Rb is -710(100) keV [59], which is based on the high precision mass measurement of ^{73}Kr and calculated Coulomb Displacement Energies (CDE). By studying the β-decay of ^{73}Sr, one can obtain the proton-separation energy, S_p for ^{73}Rb. To gain a complete picture of the two-proton capture branch for the ^{72}Kr waiting point, the measurement of half-life of ^{74}Sr was required. Another goal was to probe the proton drip-line for the elements of Y and Zr by searching for ^{75}Y and ^{77}Zr, and studying the decay of ^{76}Y.

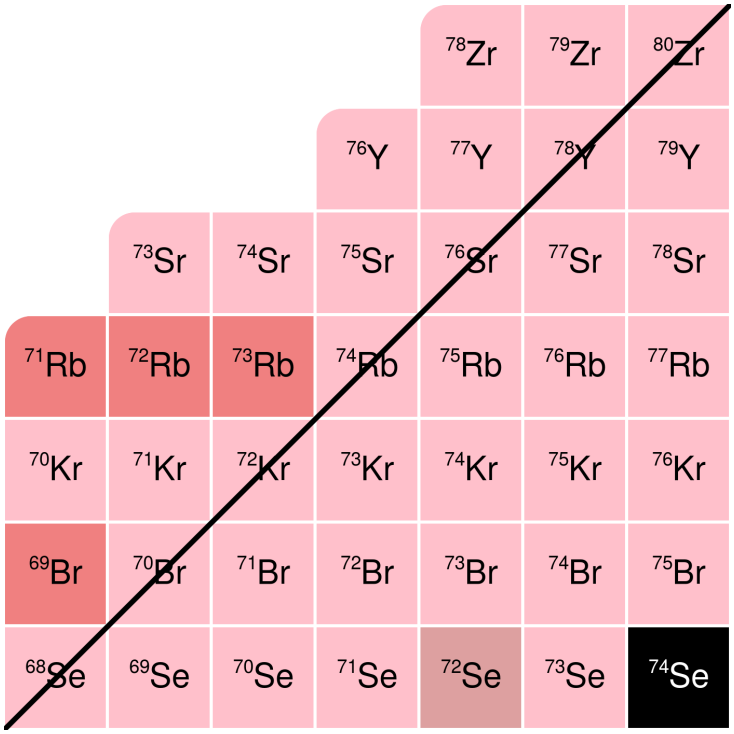

Figure 1.7: An illustration of the nuclear chart, expanded about the mass 70 region, which is of interest for the present work. The black line shows the N=Z line. Colours indicate the decay modes of the nuclei; light pink nuclei (i.e. ^{74}Sr) β-decay, bright pink are proton unbound (e.g. ^{73}Rb), dark-pink nuclei proton decay (e.g. ^{72}Se) and black nuclei (i.e. ^{74}Se) are stable. Figure adapted from [60].

An outline of the theoretical considerations and models of direct relevance to this work are described in Chapter 2. Details of the set-up of the experiment performed at RIKEN is described in Chapter 3, whilst the details of the data analysis are given in Chapter 4, including particle identification and data merging. The results and analysis of the β- and γ decay spectroscopy of the mass 70 region deduced from this experiment are presented in Chapter 5. In Chapter 6, the measurement of lifetimes of nuclei beyond the N=Z line and proton emission calculations are presented. In Chapter 7, the astrophysical impact of the β-decay studies are investigated by performing reaction network calculations. Chapter 8 draws conclusions from the analysis and discusses the potential for future work in the proton-rich mass 70 region.

Chapter 2

Theoretical considerations

2.1 β-decay

β-decay involves either the emission of an electron (β^--decay) (eqn. 2.1), or a positron (β^+-decay) (eqn. 2.2) which competes with capturing an electron (electron capture) (eqn. 2.3). These processes are governed by the weak force. In the β^+-decay process a proton is transformed into a neutron, with the nucleus emitting a positron, this is a process which occurs on the proton-rich side of the valley of stability. The basic decay processes are:

$$ {}^{A}_{Z}X_N \rightarrow {}^{A}_{Z+1}X'_{N-1} + e^- + \bar{\nu}_e, \tag{2.1} $$

$$ {}^{A}_{Z}X_N \rightarrow {}^{A}_{Z-1}X'_{N+1} + e^+ + \nu_e, \tag{2.2} $$

$$ {}^{A}_{Z}X_N + e^- \rightarrow {}^{A}_{Z-1}X'_{N+1} + \nu_e + X_{ray}, \tag{2.3} $$

with the parent nucleus, X, and the daughter nucleus, $X^{'}$, mass, A, proton number, Z, and neutron number, N. The energy released in a β-decay, is used to define the energy difference, Q, between the two ground-states of the parent and the daughter nuclei:

$$ Q_{\beta^-} = [M_P - M_D]c^2, \tag{2.4} $$

$$ Q_{\beta^+} = [M_P - M_D - 2m_e]c^2, \tag{2.5} $$

where M_P and M_D are the atomic masses of the parent and daughter nuclei, respectively, m_e is the mass of the electron and c is the speed of light.

In contrast to α- and γ decay, β^+-decay is a three-body process. An electron neutrino must be emitted with the positron, as a requirement for lepton number conservation. β particles form a continuous distribution with any energy from zero up to the total accessible energy, or end-point, given by the β-decay Q-value. A schematic figure showing the β-particle energy distributions expected from a β-decay of a given Q-value is shown in Fig. 2.1 and is described as:

$$N(T_e) = \frac{C}{c^5}(T_e^2 + 2T_e m_e c^2)^{1/2}(Q - T_e)^2(T_e + m_e c^2), \tag{2.6}$$

with kinetic energy, T_e, intensity, N, and a constant, C.

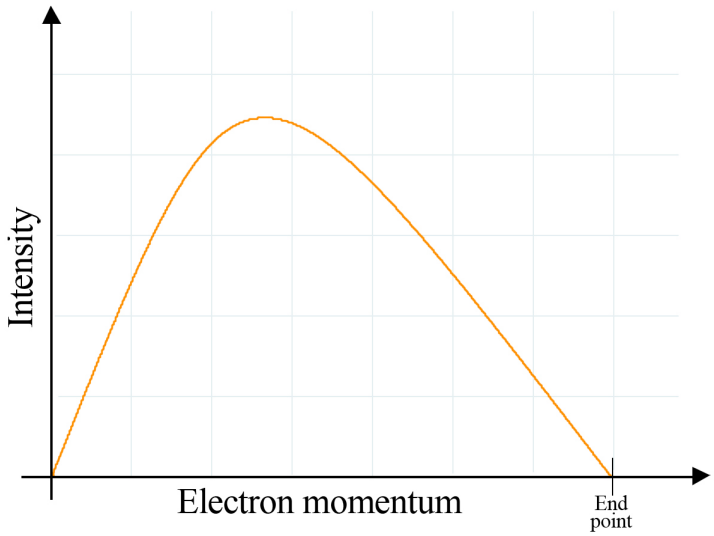

Figure 2.1: Schematic figure showing the expected momentum distribution for β-decay of a given Q-value. Figure from [47].

2.1.1 Fermi decay

In 1934, Fermi proposed a description of the β-decay process based on the neutrino hypothesis [61]. The transition rate for β-decay between an initial state i and final state f, λ, is given by Fermis Golden Rule [21, 61]:

$$\lambda = \frac{2\pi}{\hbar}|V_{fi}|^2\rho(E_f), \tag{2.7}$$

where the matrix element V_{fi} is the integral of the interaction between the initial and final states, and the factor $\rho(\mathrm{E}_f)$ is the density of final states.

2.1.2 Total β-decay rate

The transition probability for β-decay is often referred to in terms of the $log_{10}fT_{1/2}$ of the transition. The Fermi integral, *f*, is a dimensionless quantity given by [21]:

$$f(Z', E_0) = \frac{1}{(m_e c)^3 (m_e c^2)^2} \int_0^{p_{max}} F(Z', p) p^2 (E_0 - E_e)^2 dp, \tag{2.8}$$

where E_0 is the maximum electron energy, i.e. the decay end-point, E_e and p are the kinetic energy and momentum of the electron (or positron) respectively and Z' is the atomic number of the daughter nucleus. The function $F(Z', E_0)$ is known as the Fermi integral. The comparative half-life gives a measure of changes in the nuclear matrix element, M_{fi}, [21]:

$$fT_{1/2} = ln(2) \frac{2\pi^3 \hbar^7}{g^2 m_e^5 c^4 |M_{fi}|^2}, \tag{2.9}$$

with

$$\lambda = \frac{ln2}{T_{1/2}}. \tag{2.10}$$

2.1.3 Angular momentum and parity selection rules.

β-decays are classified by two characteristics. The first is dependent on the total orbital angular momentum, L, and parity, π, (in this case carried by the positron and a neutrino). Conservation of angular momentum dictates that the difference between the angular momentum of the initial state, J_i, and the angular momentum of the final state, J_f, must be equal to the total angular momentum of the lepton pair. The β-decay can be classified as an allowed transition (L = 0, π =+1) or a forbidden transition (L $\neq$ 0, π = (-1)^L). Furthermore, within the allowed transition, a β-decay can be further distinguished by the total spin, S, carried by the positron and neutrino. For Fermi (F) decay, in which the positron and neutrino have anti-parallel spins, i.e. S = 0,

$$J_i = J_f + L. \tag{2.11}$$

Whilst for Gamow-Teller (GT) decay, in which positron and neutrino are emitted with parallel spins, i.e. $S = 1$,

$$J_i = J_f + L + 1. \tag{2.12}$$

Table. 2.1 provides a summary of the selection rules for β-decay:

Table 2.1: Classification of β-decays and selection rules with respect to the orbital angular momentum, L, the change in nuclear momentum, ΔJ, for Fermi and Gamow-Teller decays and the change in parity.

Transition	L	ΔJ	$\Delta\pi$
Super allowed	0	0	No
Allowed	0	0,1	No
First forbidden	1	0,1	Yes
Second forbidden	2	1,2	No

2.1.4 β-delayed emission

In 1916, Rutherford and Wood observed β-delayed α-decay [52]. β-decays are able to populate excited states in their daughter nuclei, this allows for decay processes to occur which may otherwise be energetically forbidden. β-delayed particle emission (in this work, β-delayed proton emission and β-delayed γ emission are of interest) is a two-step process. The first step is through the β-decay process, the daughter nuclide is formed in an excited state, which is unstable against particle emission (or gamma emission, if particle emission is not possible). The second step is the particle emission from the excited states of the "emitter" nucleus. The characteristic timescale of this particle (or gamma) emission process is governed by that of the β-decay of the parent. In the case of β-delayed proton decay, the decay from the excited levels of the emitter nucleus occurs if the excited state is above the proton-separation energy, S_p, for the emitted proton. When moving from the valley of stability towards more neutron-deficient nuclei the binding energy of the last proton, S_p gets smaller and smaller (i.e. less bound) and eventually the proton drip-line is crossed when S_p becomes negative. Proton emission is possible, though it may be less probable than β-decay, due to Coulomb repulsion and centrifugal barriers [1]. The states above the proton-separation energy, S_p, are unbound against proton emission.

2.2 γ decay

The measurement of γ radiation has long been used as a means to probe properties of the excited states (i.e. spins and parities) within the nucleus. γ-decays are transitions between internal states within the same nucleus. These occur when the nucleus emits a γ-ray to de-excite from a higher-lying state. The nucleus can also de-excite by the emission

of atomic electrons, a process known as electron internal conversion.

Selection rules are associated with transitions. If the initial and final spins of the states of the nucleus are J_i and J_f, then:

$$\mathbf{J}_i = \mathbf{J}_f + \mathbf{L}. \tag{2.13}$$

Consequently, L can take the following values in integer steps:

$$|J_i - J_f| \leq L \leq J_i + J_f. \tag{2.14}$$

Where L represents the multipolarity of the radiation, and $L = 1$, corresponds to dipole radiation, $L = 2$ to quadrupole radiation, and $L = 3$ to octupole and so forth. Radiation with multipolarity L is denoted EL or ML for electric and magnetic type, respectively. In addition, parity conservation requires:

$$\pi(ML) = (-1)^{L+1}, \tag{2.15}$$

and

$$\pi(EL) = (-1)^{L}. \tag{2.16}$$

2.3 Nuclear masses and their effect on nucleosynthesis

A nuclear reaction is a process that involves one or more atomic nuclei. Nuclear reactions can occur when the nuclear densities of the target and the projectile overlap [21]. At a small overlap elastic or inelastic scattering and few-nucleon transfer through direct reactions may occur. Two particles, i.e. a nucleus X and a particle a, can interact, producing two particles, a nucleus Y and a particle b such as,

$$a + X \rightarrow Y + b, \tag{2.17}$$

or

$$X(a, b)Y. \tag{2.18}$$

The reaction Q-value, Q, is the energy released in a nuclear reaction by the conservation of energy and is defined as:

$$Q = (M_a + M_X - M_b - M_Y)c^2. \tag{2.19}$$

where the entrance channel reactants a and X have ground state masses M_a and M_X, and the exit channel products b and Y have ground state masses M_b and M_Y.

Nuclear masses are important for reaction network calculations for the *rp*-process. Proton- and neutron- decays can occur if they are energetically allowed and are governed by nuclear binding energies, i.e. the masses of nuclei.

The atomic mass for a neutral atom with protons, Z and neutrons, N, is defined as:

$$M_A(Z,N)c^2 = Z(M_p + M_e)c^2 + NM_nc^2 - BE(Z,N), \tag{2.20}$$

or the nuclear mass can be given in terms of the atomic mass by,

$$M_{Nuc}(Z,N)c^2 = M_A(Z,N)c^2 - ZM_ec^2 + BE_e(Z). \tag{2.21}$$

where BE(Z, N) is the total binding energy of the atom and M_e, M_p, and M_n are the free electron, proton, and neutron masses, respectively.

The proton-separation energy, S_p, can be defined as the amount of energy that is required to remove a single proton from the nucleus and is given by,

$$S_p(Z,N) = BE(Z,N) - BE(Z-1,N), \tag{2.22}$$

$$= [-M(Z,N) + M(Z-1,N) + M_H]c^2, \tag{2.23}$$

$$= -Q_p. \tag{2.24}$$

For proton decay from the ground state, the proton-separation energy, S_p is equal in magnitude but opposite in sign to the ground state proton decay Q-value, Q_p. A key goal of the present work is to determine the ^{73}Rb proton-separation energy, which is equivalent to the ^{72}Kr(p,γ) ground state capture Q-value, in order to evaluate the strength of the waiting point nuclide ^{72}Kr.

2.4 Beyond the drip-line

As one moves away from the "valley of stability" towards more proton-rich nuclei, β^+-decay is usually the favoured decay mode. However, as the proton drip-line is approached, the nuclear force is no longer sufficient to bind the last proton. As the proton becomes more unbound, decay by emission of a proton can compete with β^+-decay. In some nuclei

it becomes the dominant mode of decay. The balance between these two decay modes depends sensitively on both the Coulomb and centrifugal barriers. As the proton has a positive energy, it experiences a Coulomb and centrifugal barrier that classically would bind it inside the nucleus.

In certain cases, decay by two-proton emission is also possible [62]. Proton decay from the ground state has been observed in many odd-Z nuclei between I (Z=53) and Bi (Z=83) [33]. Even-Z proton emitters have not been observed as they have extra binding energy, due to the residual pairing interaction that makes them more stable than neighbouring odd-Z nuclei. Proton decay of nuclei residing close to the N = Z line, with Z $<$ 50, are of particular interest as a potentially important input to calculate the path of the *rp*-process [63].

2.5 Proton emission calculations

The study of nuclei beyond the proton drip-line can test nuclear structure models. The decay energy and width yields information on the nuclear wave-function, therefore relatively simple observables can provide constraints on nuclear models beyond the proton drip-line [33]. Proton emission is a quantum-mechanical tunnelling effect, like α-decay. The proton must tunnel through a barrier which is commonly considered to be a superposition of a Coulomb potential, a nuclear potential with a spin-orbit interaction term, and a centrifugal potential as shown in Fig. 2.2. For spherical nuclei, proton emission studies have been shown to provide information on the wave-functions of the parent state through the Wentzel-Kramers-Brillouin (WKB) approximation. The WKB approximation method is used to calculate the transmission through the barrier in order to obtain estimates for single particle lifetimes and provide information on the angular momentum, decay energy, and half-life of the proton. The WKB approximation is a semi-classical approach, which can be used to solve the Schrödinger equation and obtain reasonable transition probabilities. It has been used successfully in many calculations of α-decay and typically provides half-lives that are within a factor of $\sim$2 of the actual experimental measurements. For proton decay from spherical nuclei, simple WKB calculations of the penetrability, based on a phenomenological single particle Woods-Saxon potential, have been quite successful in reproducing experimental values [64].

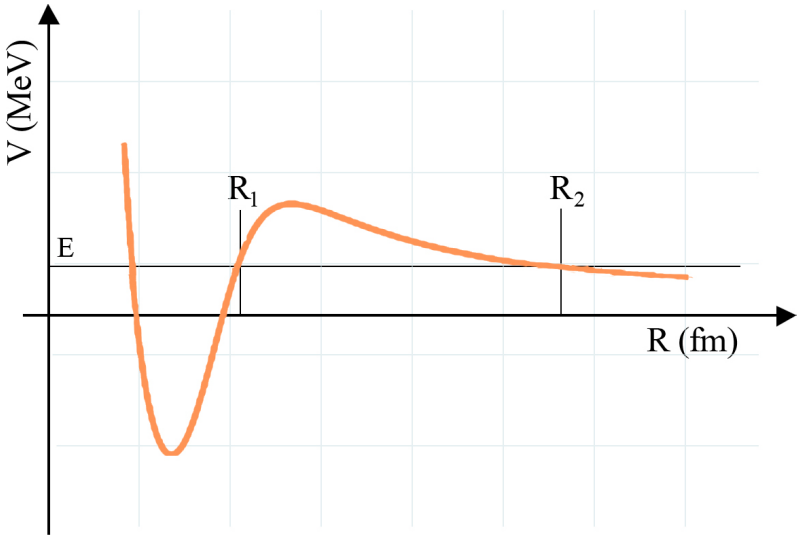

Figure 2.2: A schematic figure of the typical potential for the WKB approximation. The barrier is a superposition of a Coulomb potential, a nuclear potential (with a spin-orbit term), and a centrifugal potential. For a given excitation energy, E there are two classical turning points with regard to the barrier denoted as R_1 and R_2. Figure from [47].

In order to determine the wave-function, Ψ, for deformed nuclei one has to instead solve the full coupled channel problem for resonances [65]. The proton is a resonance state that can be found by solving the Schrödinger equation,

$$i\hbar\frac{\partial\Psi(x,t)}{\partial t} = \left[-\frac{\hbar^2}{2m}\frac{\partial^2}{\partial x^2} + V(x)\right]\Psi(x,t), \tag{2.25}$$

where $V(x)$ is a potential in 1D. The outgoing wave boundary conditions are, without or with the Coulomb interaction, e^{ikr} or the Coulomb functions, $G + iF$, respectively. This gives solutions with complex energy in the fourth quadrant (positive real part and negative imaginary part). The time evolution operator, $\phi(x) = e^{\frac{-iEt}{\hbar}}$, in this case is decaying in time as $e^{\frac{Im(E)t}{\hbar}}$. The wave-functions, after a long time, disappear with a decay width, Γ, given by:

$$\frac{\Gamma}{2} = -Im(E), \tag{2.26}$$

one can then derive the half-life from the width, Γ:

$$T_{(1/2)} = \frac{\ln(2)\hbar}{\Gamma}. \tag{2.27}$$

The half-life is dependent on the spectroscopic factor, $\sigma = \frac{T_{exp}}{T_{theo}}$. The spectroscopic factor measures the probability, after the proton decay, that the daughter nucleus is left in the

ground state. It also contains information on the nuclear structure of both the parent and daughter nuclei. The Coulomb barrier is lower and is linearly dependent on the charge of the emitted particle. The centrifugal barrier is higher and depends inversely on the mass, implying a stronger sensitivity to the orbital angular momentum.

For nuclei in which either neutrons or protons are close to a magic number, the strongest part of the residual interaction is the pairing interaction that energetically favours identical particles with angular momentum zero. This can be treated in the Bardeen-Cooper-Schrieffer (BCS) formalism [14] and the daughter ground state wave-function can be written as a condensate of pairs with angular momentum zero. In constrast, the parent wave-function is given by the odd proton on a single particle level close to the Fermi surface coupled to the same condensate. In this case the spectroscopic factor is the probability, u^2, that the single particle level of the outgoing proton is empty in the daughter nucleus. Using angular momentum conservation, one notices immediately that the outgoing proton has the angular momentum of the odd-proton, i.e. the angular momentum of the single particle level closest to the Fermi surface. Since the half-life depends strongly on the angular momentum, in this case it is possible to determine the position of the Fermi surface and the properties of the mean field far from stability.

Small proton decay widths, Γ, can be hard to find from $Im(E)$ in equation. 2.26. An alternate approach is then to use a formula derived by Maglione *et al.* [66].

$$\Gamma_{lj}(R) = \hbar/T = \frac{\hbar^2 k}{\mu} \frac{R^2 |\Psi_{lj}(R)|^2}{F_{lj}^2(R) + G_{lj}^2(R)}, \tag{2.28}$$

where R is distance from the centre of the nucleus at which the outgoing wave-function, Ψ_{lj}^{out}, is matched to the solution Ψ_{lj} of the Schrödinger equation. The indices l and j are the orbital angular momentum and the total angular momentum of the proton, respectively. $v = \hbar k/\mu$ is the velocity of the proton.

For nuclei where both neutrons and protons reside away from magic numbers, there is a need to take into account the residual quadrupole interaction between unlike particles. This interaction gives rise to rotational bands, and can be treated by a transformation, similar to the Bogoljubov [67]. The symmetry that is broken is the rotational invariance, giving rise to a deformed mean field and to the Nilsson levels. A simple WKB calculation of the penetrability is not possible in this case, since the potential is no longer spherically symmetrical. This theoretically difficult problem has been solved by either finding resonances in a deformed potential [66], by integrating the coupled-channels Schrödinger

equation [68], and the results are generally found to be in good agreement with the experimental data.

The angular momentum of the ground state of rotational odd-odd or odd-even nuclei can be quite different from the angular momentum of the spherical single particle levels. The spectroscopic factor then depends on the amplitude of the component of the Nilsson wave-function with angular momentum equal to that of the ground state, as well as the BCS probability, u^2. Therefore, for these nuclei it is possible to get detailed information on small components of the wave-function, which may not be detectable by other means.

Using the formalism described in Maglione *et al.* [66] calculations for proton emission for deformed nuclei have been performed and have been found to agree well with experimental data. These calculations have used the adiabatic approximation for the single proton and the core, i.e. the moment of inertia of the nucleus is supposed to be infinite. Recently, this model has been adapted to include the Coriolis interaction, see Fiorin *et al.* [68], which gives the core a finite moment of inertia. This more realistic approach results in good agreement with known experimental data [69, 70], if the calculation is performed using quasi-particles [71]. One can use the Nilsson model in which the wave-function does not have a well-defined angular momentum. This works for very large nuclear deformations. To take the residual pairing interaction into account, the diagonalisation of the Coriolis interaction has to be calculated between quasi-particle states. Therefore, pairing is introduced in the calculation in a consistent way, not as just an external spectroscopic factor as in the adiabatic model.

The non-adiabatic approach can also be employed for the cases where deformed nuclei are observed to decay to the first excited state of the daughter nucleus. The experimental data gives rise to further constraints to the theoretical interpretation, in this case angular momentum conservation allows the proton to escape with different angular momenta, since the first excited state of the daughter nucleus has angular momentum different from zero. In this case, theoretical calculations have also been able to reproduce the experimental data [72] using the rotational spectrum of the daughter nucleus.

For the case of decay of odd-odd nuclei, the angular momentum is determined by the Nilsson level occupied by the odd neutron in the daughter nucleus following proton decay [73]. Different angular momentum values of the odd neutron, will allow different values of the angular momentum of the escaping proton. Therefore, the odd neutron contributes actively in the decay. The neutron, by the coupling of its angular momentum, can influence

the half-life. Therefore, the odd neutron behaves as an "influential spectator". The non-adiabatic quasi-particle method has been successfully used to describe these proton decays from odd-odd nuclei where the angular momentum of the neutron has an effect [74].

2.6 Nuclear reaction network calculations for X-ray bursts

To study nucleosynthesis reaction network calculations can be performed to simulate astrophysical conditions. To obtain an accurate understanding of various astrophysical conditions, information from nuclear structure is needed to provide an input in network calculations. Nuclear reaction network calculations are performed to follow the time evolution of isotopic abundances, to find the reaction path for the *rp*-process and to determine the amount of energy released by nuclear reactions [44, 48, 75–78]. In this thesis, Type I X-ray bursts (described in Section. 1.4.1) are of interest. To accurately model X-ray bursts requires detailed nuclear physics information from 690 nuclei. For the *rp*-process, nuclear data (for example, half-lives, separation energies and masses) are vital. Any significant uncertainties in these nuclear physics quantities will affect the reliability of these network calculations.

Parametrised one-zone calculations and intensive hydrodynamic calculations [76] are two methods used for nucleosynthesis nuclear reaction network calculations. One-zone calculations relate the history of the neutron star's accreted envelope with the time evolution of the temperature, T, and density, ρ, in a single layer of the envelope. This approach was used to overcome the time limitations that arise in the computationally intensive hydrodynamic calculations. One-zone calculations have been used to calculate the impact of nuclear uncertainties on the final X-ray burst yields [49].

Early *rp*-process simulations reached an endpoint at ^{56}Ni, and consistently found that not all of the hydrogen was consumed [49]. In 2001, Schatz *et al.* [49] performed nuclear reaction network calculations, for an X-ray burst, that included all known proton-rich nuclei from Hydrogen to Xenon. Nuclear and reaction-rate data were used from REACLIBV2, provided by JINA Reaclib database [79]. The REACLIBV2 included the NON-SMOKER [80] code that uses Hauser-Feshbach theory to calculate (p,γ) reaction rates. The X-ray burst model determined that the endpoint of the *rp*-process to be the Sn-Sb-Te cycle. Schatz *et al.* [49] demonstrated that the *rp*-process cannot proceed beyond $^{107,108}_{52}$Te, since known ground state α emitters create a process terminating cycle, and all of the hydrogen is burned. In Fig. 2.3 the path of the *rp*-process calculated by Schatz *et al.* [49] is

shown on the chart of nuclides.

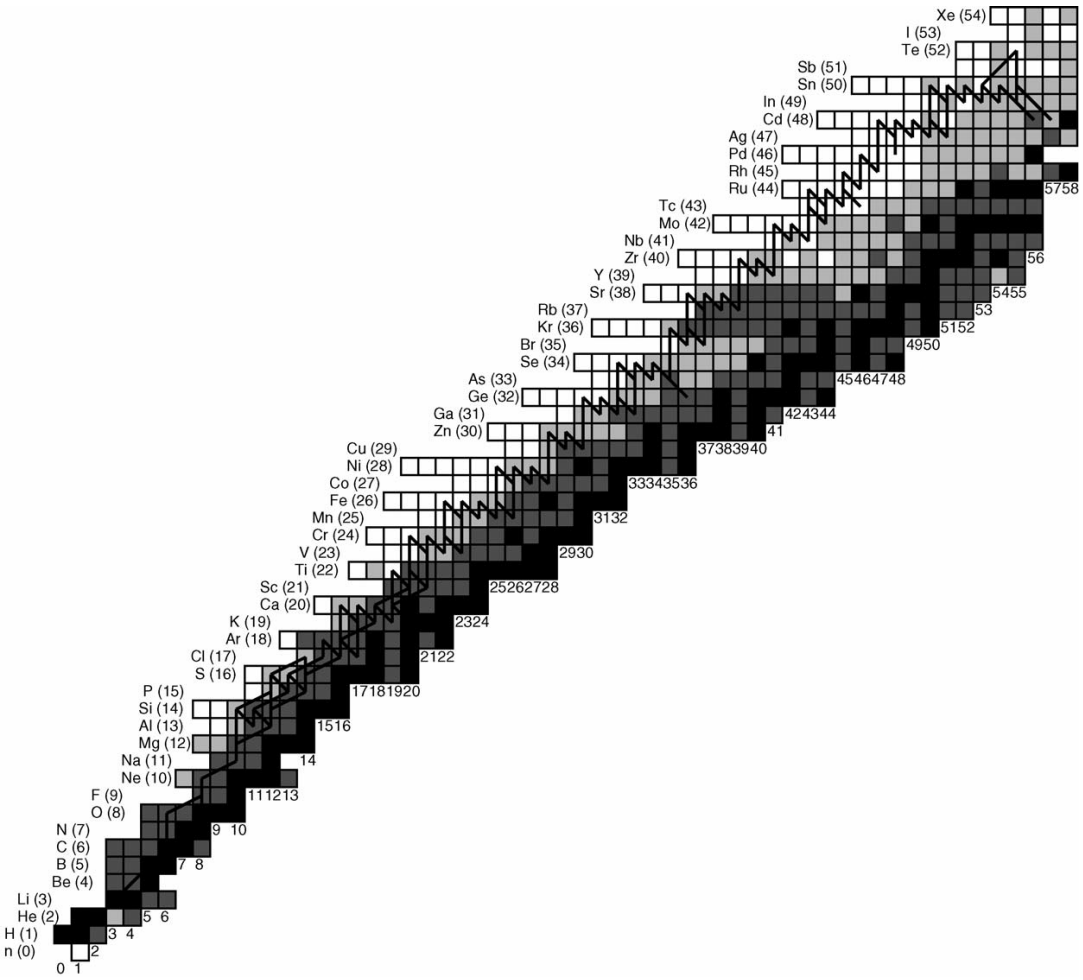

Figure 2.3: The path of the *rp*-process from [49] on the chart of nuclides. Stable nuclei are black, nuclei with experimentally known masses are grey, dark grey for uncertainties of less then 10 keV, light grey for larger uncertainties. Note the endpoint of the *rp*-process with Sn-Sb-Te cycle.

2.7 Nuclear structure information for the *rp*-process

As mentioned previously, β-decay half-lives, precise mass measurements and (p,γ) cross sections [44] are important parameters for the *rp*-process. The latter two of these require different experiments to the measurements described in this thesis, and will therefore not be discussed further. The *rp*-process consists of a series of proton capture reactions, (p,γ), photodissociation reactions, (γ,p), and β^+-decay. Rapid proton captures occur on the seed nuclei, and drives the path towards the proton drip-line, and is interspersed with β^+-

decays that drive the composition toward the valley of stability. If the β^+-decay lifetime is short enough, it can compete with the proton capture process.

As mentioned in Section. 1.4.3, ^{72}Kr is a waiting point in the *rp*-process and ^{73}Rb is expected to be proton-unbound [52]. To determine the effective lifetime of a waiting-point nucleus (Z, N), the binding energy of the $(Z+1, N)$ nucleus must be known. Proton capture on ^{72}Kr populates unbound states in ^{73}Rb, that proton decay back to ^{72}Kr, meaning β^+-decay must occur for the *rp*-process to proceed. The capture of two protons can bypass the waiting point. The effective lifetime of ^{72}Kr can be long enough, due to the Coulomb barrier, for the *rp*-process to proceed via sequential two-proton capture in X-ray burst conditions, but this is dependent on the proton-separation energy of the unbound nuclide ^{73}Rb.

As the mass of ^{73}Rb cannot be measured directly β-delayed proton emission can be used to deduce the proton-separation energy. Proton emission following a Fermi-allowed β-decay can provide limited information on excited states in the daughter nucleus. The Fermi β-decay of ^{73}Sr decays into the IAS of the daughter nucleus, ^{73}Rb and this IAS branch is predicted to be about 50% [81]. Fig. 2.4 shows the anticipated β-delayed proton decay scheme of ^{73}Sr, where the ground-state spin of ^{73}Sr, along with spin and energy of ^{73}Rb levels are the ones expected from mirror-nucleus symmetry in ^{73}Kr. As the proton-separation energy of ^{73}Rb corresponds to the proton capture Q-value for the reaction ^{72}Kr(p,γ)^{73}Rb (S_p =-Q_p), knowledge of the proton-separation energies for ^{73}Rb is essential for the estimation of the effective lifetime of ^{72}Kr.

Based on such spin assignments and a population of the IAS of 50% [81], it is reasonable to expect a significant population of low-energy states in ^{73}Rb, and in particular of the ground state, which could be fed by an allowed GT transition. The decay between ^{73}Sr and ^{73}Rb has the angular momentum difference, $\Delta I = 1$. This expectation is somewhat supported by the known decay of the light odd-A Sr isotopes such as ^{75}Sr and ^{77}Sr, which populate the ground state of their respective daughters with intensities I_β= 90% [82] and I_β= 80% [83], respectively. In the case of ^{75}Sr, the ground state is fed directly. In the second case the ground state is fed by the decay of the first excited state, which is fed directly. The observation of the β-proton decay would allow for the extraction of the proton-separation energy, S_p for ^{73}Rb. The proton-separation energy S_p = -710 keV is predicted by CDE calculations [59]. As ^{73}Kr is the mirror nucleus to ^{73}Rb, nuclear model calculations and experimental data can guide the understanding of the possible

level structure for ^{73}Rb. If isospin were an exact symmetry, one could exactly predict the structure of ^{73}Rb from the structure of the mirror nucleus ^{73}Kr.

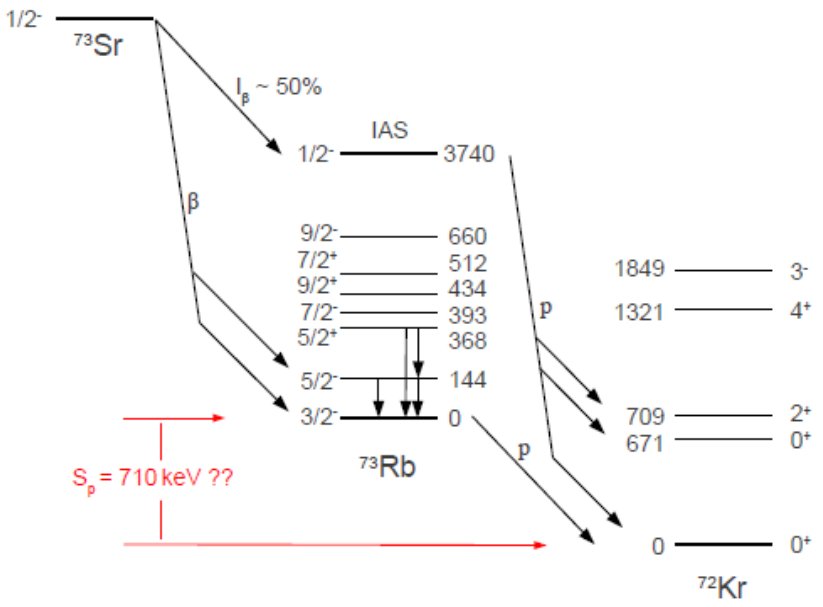

Figure 2.4: The anticipated decay scheme of ^{73}Sr. The energy and spin of states in ^{73}Rb are inferred from mirror-nucleus symmetry in ^{73}Kr. The estimated S_p value comes from CDE calculations [59]. Models predict that there should be a branching ratio of around 50% in the β-decay to the ground state of ^{73}Rb, see text for details. Figure from [84].

The first measurement of the β-delayed proton decay of ^{73}Sr was performed in 1993 by Batchelder *et al.* [81]. Due to the experimental set-up, only proton decays above an energy of ∼2.5 MeV were observed. The Fermi β-decay to the IAS in ^{73}Rb was reported to be 3.75(4) MeV and a β-branching to IAS of ∼50%. A lower limit for the half-life of ^{73}Sr of $T_{1/2} > 25$ ms was deduced. Pfaff *et al.* [52] determined an upper limit of 30 ns for the half-life of ^{73}Rb, which indicated that ^{73}Rb is proton-unbound by at least 680 keV. Table. 2.2 compares the previous values calculated for the S_p for ^{73}Rb.

Kaneko *et al.* [87] has recently calculated the proton (S_p) and two-proton (S_{2p}) separation energies in the region of interest. These are shown in Fig. 2.5. The Q_{syst}(EC) value used in the Skyrme Hartree-Fock calculations corresponds to $S_{2p} = 3.74$ MeV, and is in reasonable agreement with the GXPF1A calculations. The results of these shell model calculations are also in reasonable agreement with the prior calculations given in Table. 2.2.

Table 2.2: Previous values given for the proton-separation energies, S_p, for ^{73}Rb.

Nuclide	S_p (keV)	Source
^{73}Rb	<-680	From the upper limit of τ [52]
^{73}Rb	-550(320)	Theoretical [85]
^{73}Rb	-600(150)	AME-2003 [86]
^{73}Rb	-710(100)	CDE calculations [59]

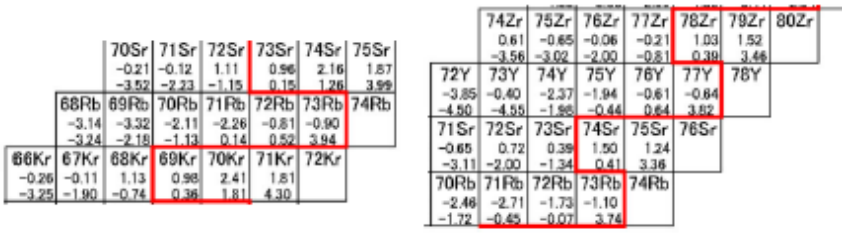

Figure 2.5: Proton and two-proton-separation energies, in the region of interest, from shell-model calculations using the GXPF1A (left) and the JUN45 (right) shell-model effective interactions. The nuclide is followed by the calculated proton and two-proton-separation energy values. The red line indicates the proton drip-line. Figure reproduced from [87].

Chapter 3

Experimental set-up and preliminary data analysis

The thesis experiment, RIBF97 was performed at the Radioactive Isotope Beam Factory (RIBF), which is operated by the RIKEN Nishina Center [88]. The facility is an in-flight RI beam separation facility [88]. The experiment was conducted in the framework of the EURICA (the EUroball at RIken Cluster Array) campaign. One of the main goals of RIBF97 was to measure the proton-separation energy (S_p) of ^{73}Rb by studying the β-delayed protons following the decay of ^{73}Sr. Another goal was to determine the half-life of ^{74}Sr, to gain a complete picture of the two-proton capture branch for the ^{72}Kr waiting point in the *rp*-process. The location of the drip line is of important interest for the *rp*-process. The final goal was to probe the proton drip-line for the elements of Y and Zr by searching for ^{75}Y and ^{77}Zr, and investigating the decay mode of ^{76}Y. For RIBF97, BigRIPS (Big RIKEN Projectile Fragment Separator) was adjusted to two settings, one for a maximum transmission of ^{73}Sr and the other for ^{74}Sr. The RIBF97 experiment was performed in June and July 2013 with a total beam-on-target time of two days.

In the experiment, radioactive beams were produced following fragmentation and these were identified and separated by the fragment separator BigRIPS, and then transported by the ZeroDegree spectrometer (ZDS) to the focal plane. At the final focal plane, an array of HPGe detectors, EURICA, surrounded an active stopper, Wide-range Active Silicon-Strip Stopper Array for Beta and ion detection (WAS3ABi). This set-up was used for the study of γ decaying isomers and β-γ spectroscopy of nuclei. In the following sections, an introduction is given to the production, separation and identification of the RI beams, followed by a detailed description of the detectors used for the studies of the stopped

nuclei.

3.1 Primary beam production

The accelerator facility at the RIBF consists of a multistage accelerator system to produce the ^{124}Xe beam at an energy of 345 MeV/u for RIBF97. The schematic diagram of the accelerator system is shown in Fig. 3.1. The ^{124}Xe beam was produced by the fixed-energy mode [89]. The fixed-energy mode injects 28 GHz microwaves from a gyrotron superconducting electron cyclotron resonance (SC-ECR) ion source. The ions were accelerated through the RIKEN Heavy Ion LINAC (RILAC2) [89], RIKEN Ring Cyclotron (RRC), fixed frequency Ring Cyclotron (fRC), Intermediate-stage Ring Cyclotron (IRC) and then the Superconducting Ring Cyclotron (SRC). After exiting the SRC accelerator, the ^{124}Xe beam has an energy of 345 MeV/u. The primary beam intensity ranged from 30 to 35 pnA.

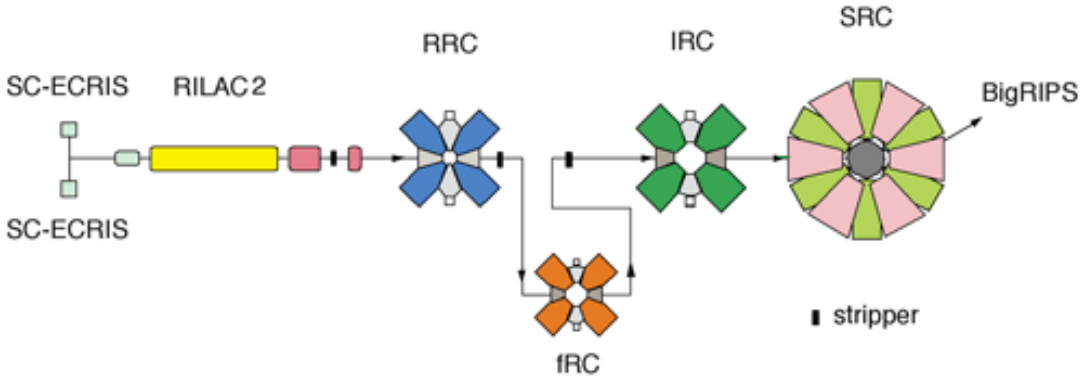

Figure 3.1: A schematic diagram of the accelerators used in the fixed-energy mode at RIBF. The ions are accelerated through the RIKEN Heavy Ion LINAC (RILAC2) [89], RIKEN Ring Cyclotron (RRC), fixed frequency Ring Cyclotron (fRC), Intermediate-stage Ring Cyclotron (IRC) and then the Superconducting Ring Cyclotron (SRC). After exiting the SRC accelerator, the ^{124}Xe beam had an energy of 345 MeV/u. Image adapted from [90].

Two charge strippers were used to increase the charge states of ^{124}Xe for further acceleration, the first of which was located at the exit of the RRC, while the second is located between the fRC and the IRC [89]. The ^{124}Xe beam at 345 MeV/u impinged on a 555 mg/cm^2 thick ^{9}Be production target of BigRIPS, (see Fig. 3.2). In this work, ^{9}Be was selected as the target material due to a high number of atoms per unit volume, which allows

for a more accurate measurement of the fragment energies generated in the reaction [91], and minimises the energy loss as particles pass through the target. Furthermore the high density maximises the number of reactions per second.

3.2 BigRIPS

BigRIPS is a two-stage RI beam separator [88], which is in operation at the RIBF [92]. BigRIPS, a superconducting fragment separator, similar to the FRS (FRagment Separator) at GSI Helmholtz Centre for Heavy Ion Research facility, can be used to transport, separate and identify cocktail beams produced following projectile fragmentation of stable isotopes or by in-flight fission of uranium isotopes [88]. It should be noted that GSI has beam energies of up to 2 GeV/A while RIKEN is currently limited to 345 MeV/u [92].

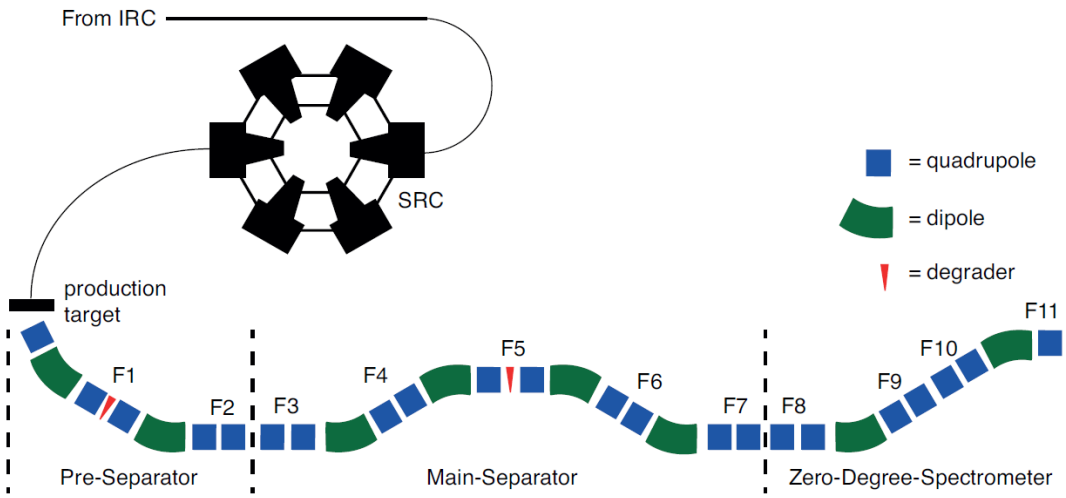

Figure 3.2: Schematic layout of the experimental set-up from the IRC and SRC to the production target, the two stages of BigRIPS and the delivery of the beams through ZDS to the focal plane. Degraders are located at F1 and F5. A beam dump is located at the target position. There are two parallel plate avalanche counters (PPACs) per foci located at; F3, F5 and F7. A Multiple Sampling Ionisation Chamber (MUSIC), was used to measure energy loss, and is located at F7. Plastic scintillator counters are located at F3 and F7. The flight path is 46.6 m between F3-F5 and F5-F7, see text for details of their use. Figure reproduced from [93].

Shown in Fig. 3.2 is a schematic diagram of the BigRIPS experiment displaying all the quadrupole and dipole magnets used for beam focussing and bending. The positions of

the beam-line detectors used for particle identification, the dipole magnets (DN) and foci (FN) are all indicated. The different focal planes are labelled as F1 to F11. Each of the stages will be discussed in detail below.

The first stage spans from the production target (PT or F0) to F2, whilst the second stage spans from F3 to F7, with a flight path of 46.6 m. A beam line spectrometer located between F8-F11 was used to transport the tagged ions to the final focal plane, F11.

3.2.1 First Stage: Beam production, collection and separation

The first stage of BigRIPS was used to produce, collect and separate the primary RI beams [94]. This stage begins at the production target (PT or F0) and continues until F2. This stage comprises a two-bend achromatic spectrometer, which consists of four superconducting triplet quadrupoles (STQs) and two room-temperature dipoles (RTDs) with a bending angle of 30°. Fig. 3.3 displays the production of a heavy-ion beam, impinging on a target and converted into a RI beam.

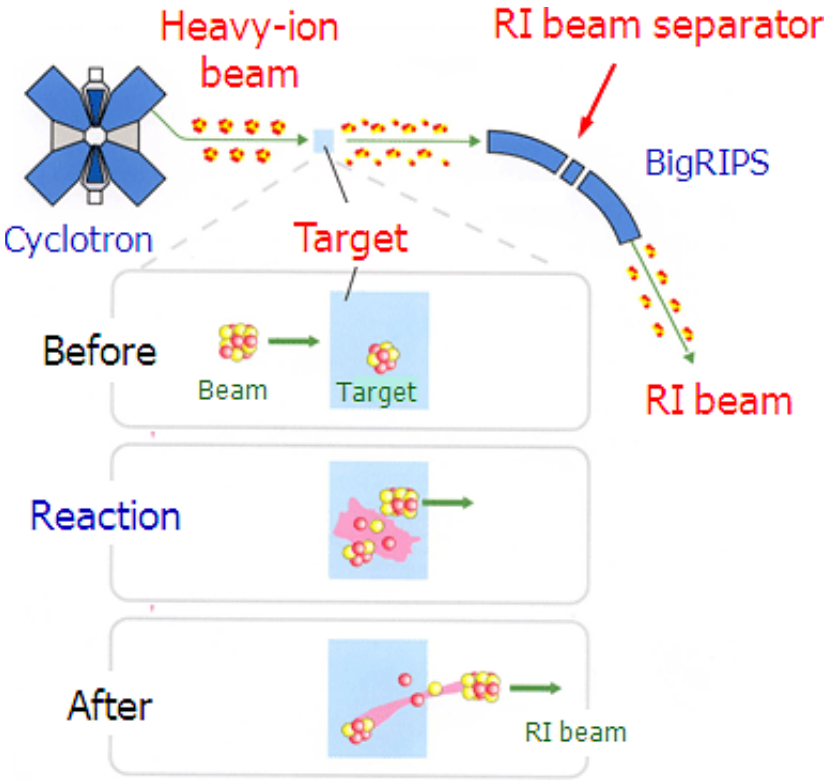

Figure 3.3: Schematic figure showing the production of radioisotopes using a heavy-ion primary beam and RI beam separator. Figure reproduced from [95].

The separation was performed by the Bρ-ΔE-Bρ method. To transport ions with a

certain magnetic rigidity, Bρ, to the main separator, a value for the magnetic field B in both dipole magnets is selected see Fig. 3.2. Bρ is defined as [92]:

$$B\rho = \frac{\gamma m_o v}{q} = \frac{A}{q}, \tag{3.1}$$

with the bending radius ρ, of the ion in the magnetic field, relativistic factor γ, and the mass m_0, a charge, q, and velocity v of the ion.

The wedge-shaped degrader located at the focal plane F1 is momentum dispersive, this provides a further selection criteria. The dipole introduces dispersion, therefore ions with a range of momenta will experience different energy losses. The projectile fragments of the primary beam are collected by BigRIPS. Efficient collection of these fragments was made possible by large acceptances. The angular acceptances of BigRIPS are ±40 mrad horizontally and ±50 mrad vertically, with momentum acceptance of ±3% [94].

3.2.2 Second Stage: Separation and particle identification of secondary beam production, via fragmentation reactions, with the ToF-Bρ-ΔE method

The role of the second stage of BigRIPS is to identify of RI-beam species, in an event-by-event mode and delivering tagged RI beams to the experimental focal plane, which is located at F11. The nuclei of interest in this thesis were identified using the BigRIPS spectrometer [92]. The magnetic rigidity (Bρ), energy loss (ΔE) and time-of-flight (ToF) of ions were used to deduce the atomic number Z and the mass-to-charge ratio (A/Q). This is known as the ToF-Bρ-ΔE technique. This method relies on a combination of ion optics and reaction kinematics [96]. A brief description of the detectors and procedures used for the measurements of ToF, Bρ and ΔE are discussed in the following sections. For a more detailed description please refer to Ref. [94].

3.2.3 ToF measurements and PPACS

The Time-of-Flight, ToF, was used to determine the mass-to-charge ratio A/Q and for the velocity correction of the energy loss measurements. The ToF of a heavy ion was measured using two thin plastic scintillation counters located at the focal planes F3 and F7, i.e. the beginning and end of the second stage of the BigRIPS. Small beam spots at these achromatic foci allow ToF measurements with good time resolution [94]. For the position measurements of ions, PPACs detectors were used. The PPACs were developed

at RIKEN [97]. Two PPACs are positioned at each of the focal planes located at F3, F5 and F7. The PPACs are used for beam tracking and to calculate the angle of the ions at the focal plane with respect to the main beam axis. An incident particle ionises the gas between a cathode and an anode. The free electrons and the ions are then detected in the anode/cathode due to the separation by the applied high voltage.

The detectors used at BigRIPS have an anode between two cathodes, with one cathode to measure the position in x- direction and the other one for the position measurement in y-direction. The PPACs are filled with C_3F_8, at a pressure of 30 Torr. The use of C_3F_8 is to improve the efficiency of the PPAC since the large energy-loss of the ions gives larger analog output signals [94]. The voltage applied is usually less than 2000 V and must be adjusted according to the beam energy and the expected energy loss of the heavy ions.

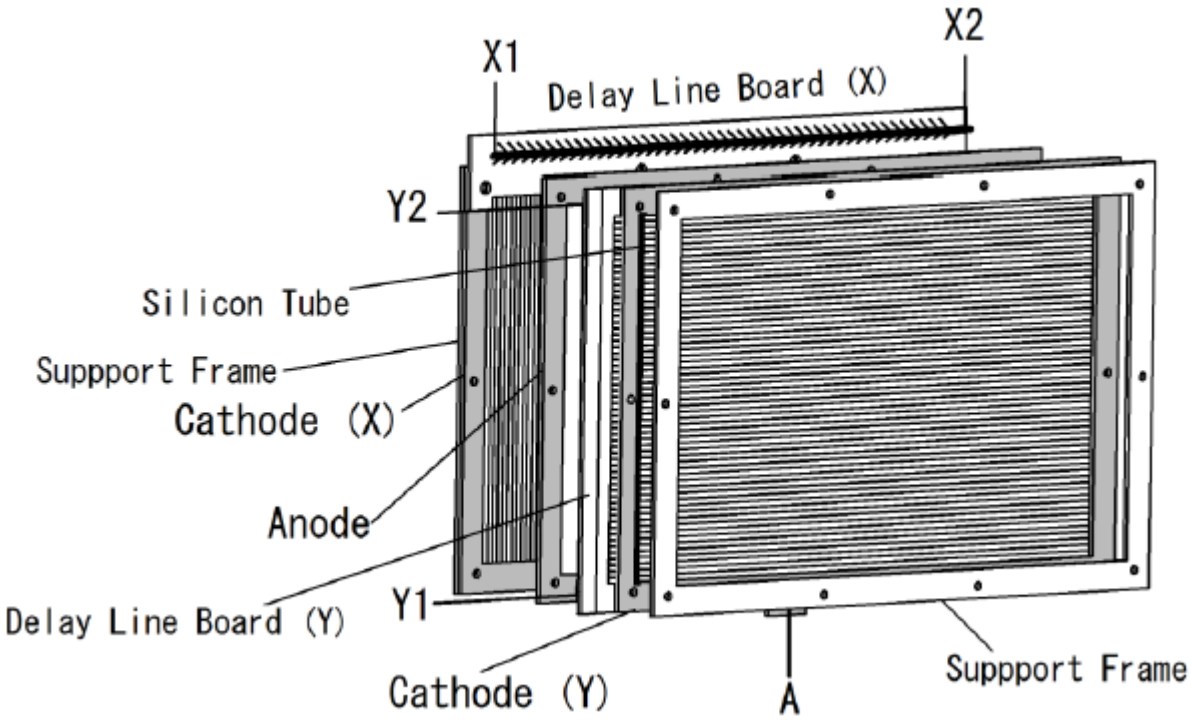

Figure 3.4: A schematic figure giving an expanded view of a PPAC. The active area of the detector is 100×100 mm^2. Figure reproduced from [94].

The cathodes have a strip width of 2.4 mm and have a spacing of 0.15 mm and are shown in Fig. 3.4. In both cases the signals are fed into a delay-line with signal readout on both sides. The signals are processed by a Constant-Fraction-Discriminator (CFD) and fed into a Time-to-Digital-Converter (TDC). From the time-difference between the left and

the right side of the delay-line, the $x(y)$-position can be calculated after a time-to-position calibration has been performed.

The ToF can then be calculated by:

$$ToF = \frac{L}{\beta c} = \frac{distance}{velocity}, \tag{3.2}$$

where L is the flight path length (flight path = 46.6m), $\beta = v/c$ (v the velocity of the particle and c is the speed of light).

3.2.4 Bρ

To measure magnetic rigidity, Bρ, the trajectory reconstruction was made in the two halves of the second stage of BigRIPS i.e. F3-F5 and F5-F7. As previously discussed, two sets of PPACs are mounted at focal planes F3, F5 and F7 to measure the trajectories of the particles, i.e. the position and the angles of the fragments. Ion-optical transfer matrix elements up to the third order, deduced from experimental data, are used for the trajectory reconstruction. The absolute Bρ value of fragments on the central trajectory, called the central Bρ value, was determined by using the magnetic fields of the dipole magnets measured by NMR (nuclear magnetic resonance) probes and the central trajectory radii of the dipole magnets deduced from the magnetic field-map data.

The ToF and ΔE measurements are calibrated by using the central Bρ value obtained. As the PPAC detectors and the energy degrader at F5 give rise to energy loss, the two-fold Bρ measurement mentioned above was needed to deduce the A/Q value of fragments in combination with the ToF measurement between F3 and F7. The A/Q was calculated as:

$$\frac{A}{Q} = \frac{B\rho}{\beta\gamma}\frac{c}{m_u}, \tag{3.3}$$

where c is the speed of light, m_u = 931.494 MeV is the atomic mass unit, A and Q represent the atomic mass and the charge (charge state) number of the particle.

3.2.5 ΔE from Multi-sampling ionisation chamber

The energy-loss, ΔE, of the ions is used to deduce the nuclear charge, Z. The energy loss was measured by two Multiple Sampling Ionisation Chambers, MUSIC [98]. The chambers are filled with pure CF_4 at room temperature and atmospheric pressure. Each of the detectors has one cathode and eight anode strips, which are used to measure the energy loss. For each MUSIC, one obtains eight energy loss measurements from which a

geometrical average is calculated to reduce statistical error. Ions passing through the gas create electron-ion pairs, and because of an applied electric field, the electrons travel to the anodes. The number of electrons created after the ionisation is directly proportional to the energy deposited by the beam particle. The energy-loss of heavy ions in matter is well-described by the Bethe-Bloch formula:

$$\frac{-dE}{dx} = \left(2\frac{e^2}{4\pi\epsilon_o}\right)\frac{4\pi Z^2 N_A Z_A \rho}{mc^2\beta^2 A}\left[ln\left(\frac{2mc^2\beta^2}{I}\right) - ln(1\beta^2) - \beta^2\right]. \tag{3.4}$$

Where e is the electronic charge, ϵ_o the vacuum permittivity, N_A the Avogadro constant, m is the rest mass of the electron, and I is an experimentally determined parameter describing the average ionisation potential and excitation energy of the absorber material. The absorber material is defined by its atomic number Z_A, mass A, and density ρ. The only two variables in the Bethe-Bloch formula of the beam particle are atomic number Z and the relativistic factor β. Hence, the energy loss, ΔE, of the beam particle in the ionisation chamber can be written as:

$$\frac{-dE}{dx} = Z^2 f(\beta). \tag{3.5}$$

In this expression, the dependence of the energy loss, ΔE, on the atomic number Z can be seen. The function f(β) is independent of the individual beam particle and therefore, a calibration with a primary beam and a known atomic number Z_P can be performed to determine the atomic number Z_F of an unknown fragment created in the primary target:

$$\frac{-dE_F}{dx} = \frac{Z_F^2}{Z_P^2}\frac{dE_P}{dx}. \tag{3.6}$$

3.3 ZeroDegree spectrometer

After being separated and identified in BigRIPS, the ions of interest were transported by the ZeroDegree spectrometer (ZDS) to the final focal plane, F11, where an active stopper was placed. The ZDS is a beam line spectrometer which is located between F8 and F11. ZDS is designed as a two-bend achromatic system with anti-mirror symmetry, consisting of two dipoles and six STQs [92].

3.4 Detectors for decay spectroscopy

At the final focal plane, F11, an active stopper WAS3ABi was surrounded by EURICA. Fig. 3.5 shows a photograph of the focal plane set-up used in RIBF97. The details of WAS3ABi and EURICA are discussed in the next sections.

Figure 3.5: A photograph of the set-up of the F11 focal plane for RIBF97. EURICA and the chamber with the active stopper WAS3ABi.

3.4.1 EURICA

EURICA, shown in the schematic diagram in Fig. 3.6, comprises twelve cluster detectors. Each of the twelve EURICA clusters is composed of seven tapered, hexagonal high-purity Germanium (HPGe) crystals [99]. The clusters were arranged in a spherical structure. One of the crystals is central, whilst the remaining six crystals are placed in a surrounding ring [99]. EURICA was used to detect the β-delayed γ-rays and isomer γ-rays emitted from radioactive isotopes with a high energy resolution [100].

For each of the 84 crystals in the EURICA, the signal was divided by the preamplifiers into two channels for the energy and timing measurements. One of the signals were sent to the Digital-Gamma-Finder (DGF) modules, and the other signal was processed by analogue timing electronics.

The 84 signals in the digital branch, for energy and timing, were distributed to 24 DGF modules, each with four channels at a clock frequency of 40 MHz, corresponding

to 25 ns time steps. The inbuilt ADC (Analog-to-digital converter) digitises the signals. For each DGF channel, the trigger is validated by a GFLT (General First Level Trigger) that corresponds to the main trigger i.e. the signal of the F11 plastic scintillator, or WAS3ABi. The main trigger is also fed into one channel of each DGF crate to check the validity of the system synchronisation and to provide a time-reference signal to calculate the time-difference between the trigger and the detection of γ-rays.

The timing branch of the crystals comprising a Timing-Filter-amplifier (TFA), a Constant-Fraction-Discriminator (CFD) and a Time-to-Digital-Converter (TDC). The 25 ns digital timing resolution of the DGF is unsuitable for the timing measurement of short-lived isomers (i.e. in the $\sim$100 ns range). The signals from the CFD are fed into two separate TDC modules, the short-range-TDC (TDCs) with a full range of 1 μs and 0.31 ns/channel and the other long-range-TDC (TDCl) with a full range of 800 μs and 0.73 ns/channel. This provides good timing resolutions for a broad range of isomers.

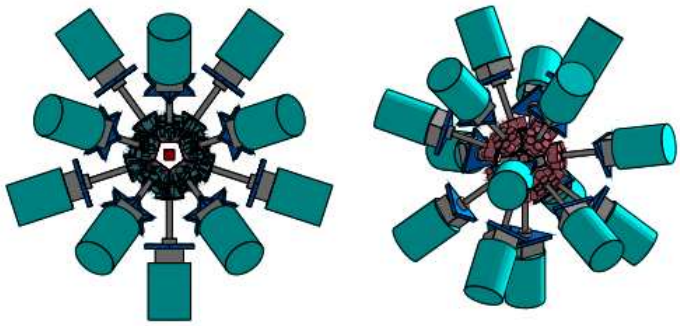

Figure 3.6: Schematic figure of the Ge array, EURICA, used for the detection of γ-rays. Figure reproduced from [101].

It should be noted that for RIBF97, only 48 crystals of the 84 Ge crystals were available for use due to a major incident, which involved the warm up of over half of the Ge detectors just prior to this experiment. This incident meant that nearly half of the EURICA detectors were not available during this experiment.

3.4.2 Ge-Array: calibration and absolute efficiency

Prior to, and after the experiment, several calibration measurements were performed with various radiation sources. The measurements were used for two different purposes, for the energy calibration of the EURICA Ge-Array and to determine of the absolute efficiency

of the EURICA set-up. The energy calibration of EURICA was performed with a ^{152}Eu source. For each crystal the 121-, 244-, 344-, 778-, 964- and 1408-keV peaks were fitted. This calibration was performed within the framework of the campaign.

3.4.3 Active Stoppers

An active stopper was used to both stop the secondary beam of interest and to detect the subsequent decay modes. The secondary beam is a cocktail of different nuclei, many of the nuclei produced in the work have half-lives of the order of ∼ms. The WAS3ABi chamber surrounded by EURICA is shown in Fig. 3.7.

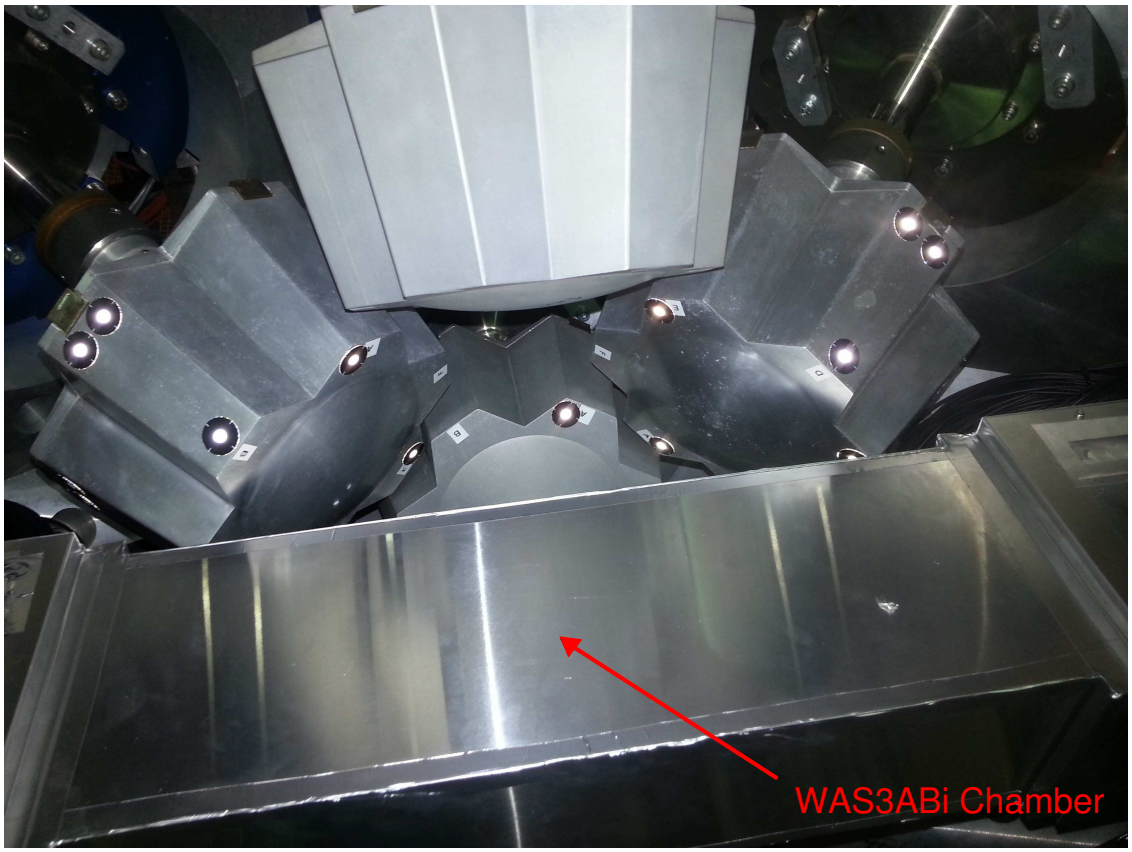

Figure 3.7: A photograph of the chamber with the active stopper WAS3ABi surrounded by the EURICA. EURICA, and the active stopper are located the focal plane F11.

Opening a gate for the data acquisition for each implanted nucleus to observe a β-decay is not practical, therefore a different approach was used. For this work, ion implantations and β-decays were treated as separate events, and the data acquisition could be triggered by either event. β-ion correlation was subsequently performed in an offline analysis, to be

discussed in Section. 4.5. The ions were implanted into a strip of the highly segmented DSSSD. A search for β-decays using position and timing information were used to correlate the observed β-decays with a detected ion, to be discussed in the next chapter. β-decay events deposit less energy in comparison to the several $\sim$GeV observed in the stopping process of an ion in the DSSSD.

3.4.4 WAS3ABi

For RIBF97, the β counting system WAS3ABi was employed for β-decay spectroscopy being specially designed to work in conjunction with EURICA. The WAS3ABi chamber was surrounded by EURICA for γ-ray detection. Fig. 3.7 displays the WAS3ABi chamber and some of the EURICA detectors. The double-sided silicon-strip detector in WAS3ABi was supported by four aluminium rods inside an aluminium chamber, with thickness of 0.2 mm as shown in Fig. 3.8. The WAS3ABi chamber was maintained at a temperature of 10°C [102] by injecting cooled dry-nitrogen gas for noise reduction in the DSSSD. The cooling gas flowed through the chamber for the duration of the experiment to reduce leakage current in the silicon detector.

In this experiment, WAS3ABI was configured in a one-off mode consisting of a single highly segmented silicon detector, used as an active stopper in conjunction with two plastic scintillators located in the chamber. The beam was degraded and implanted into the silicon detector. The detector used for WAS3ABi was a Micron Model BB13, with 128×128 segmentation, providing a total of 16384 pixels, 1 mm thick, with a 485-μm strip pitch as shown in Fig. 3.9. This provided an active surface area of 62.03×62.03 mm for the Si chip. The 1 mm thickness and $\sim$500 μm pitch were designed to reduce the summing effect. The high segmentation and narrow strip pitch allows for a higher implantation rate. The two kinds of plastic scintillator, each 3 mm thick, were used to provide good detection efficiency for the light ions and electrons. These were to veto implants and to improve detection efficiency for decays that were not detected in the DSSSD. For the experiment, a high voltage (HV) of around 400 V was applied to the DSSSD to fully bias the detectors.

3.4.5 Electronics of the active stoppers

Each strip of the 128×128 DSSSD was connected to an electronics channel. The full read-out of all strips was performed. The charge signal from the silicon strip was amplified through the charge-sensitive preamplifier (Clear-Pulse CS-520). The amplified signal was

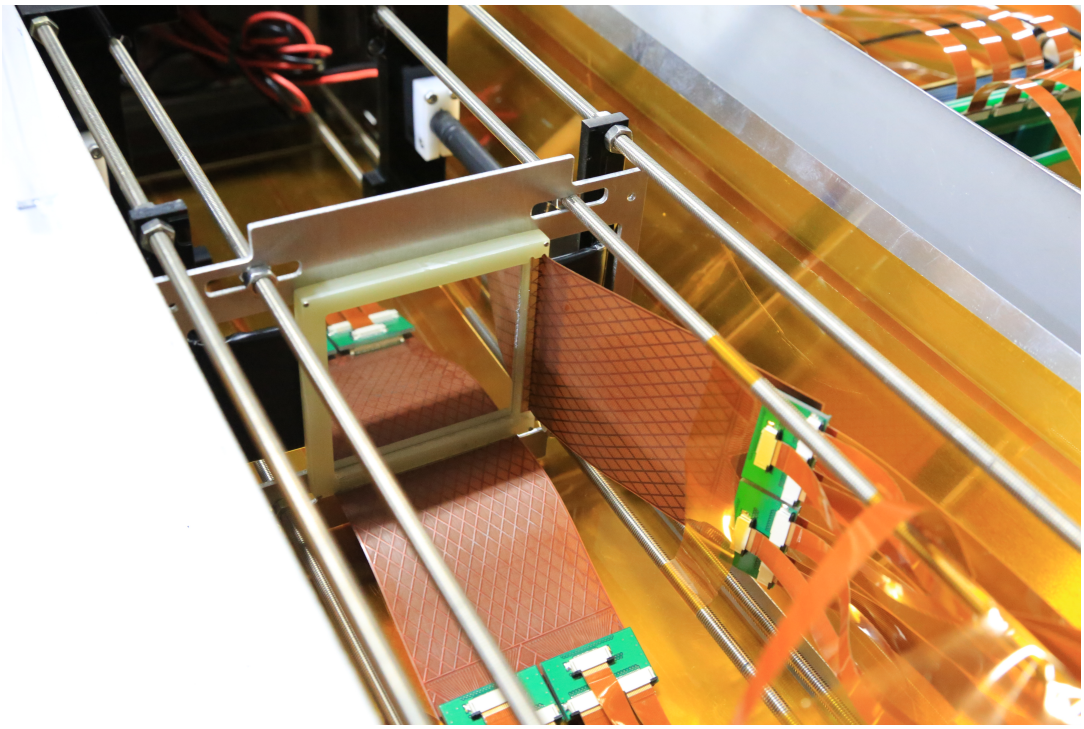

Figure 3.8: A photograph showing the overview of inside the WAS3ABi chamber and the silicon detector. The silicon detector was supported by four aluminium rods inside an aluminium chamber. This chamber acted as a light shield to avoid the absorption of emitted low-energy γ-rays. Photo courtesy of J. Wu and S. Nishimura [103].

then passed through into the shaping amplifier (CAEN N568B) [104]. One output signal from the shaping amplifier (with a shaping time of 0.2 μs) was fed into an Analog to Digital Converter (ADC) (CAEN V785), which corresponds the pulse height to a digital number, for the energy measurement. The other analogue signal was fed into an inverter, followed by a leading-edge discriminator (LeCroy 3412, 4413), a CFD and into a Time-to-Digital Converter (TDC) for the timing information and for gate/β-decay trigger generation of the data acquisition system (DAQ).

3.4.6 Implantation events

The F11 plastic scintillators of BigRIPS triggered implantation events. The trigger was sent to the three data acquisition systems (BigRIPS, WAS3ABi, EURICA), to be discussed in further detail in the next chapter. During an implantation event, when an ion is stopped, several GeV of energy is deposited into the DSSSD. This energy deposition can be distributed over several strips in x- and y- direction. The implanted ion is expected

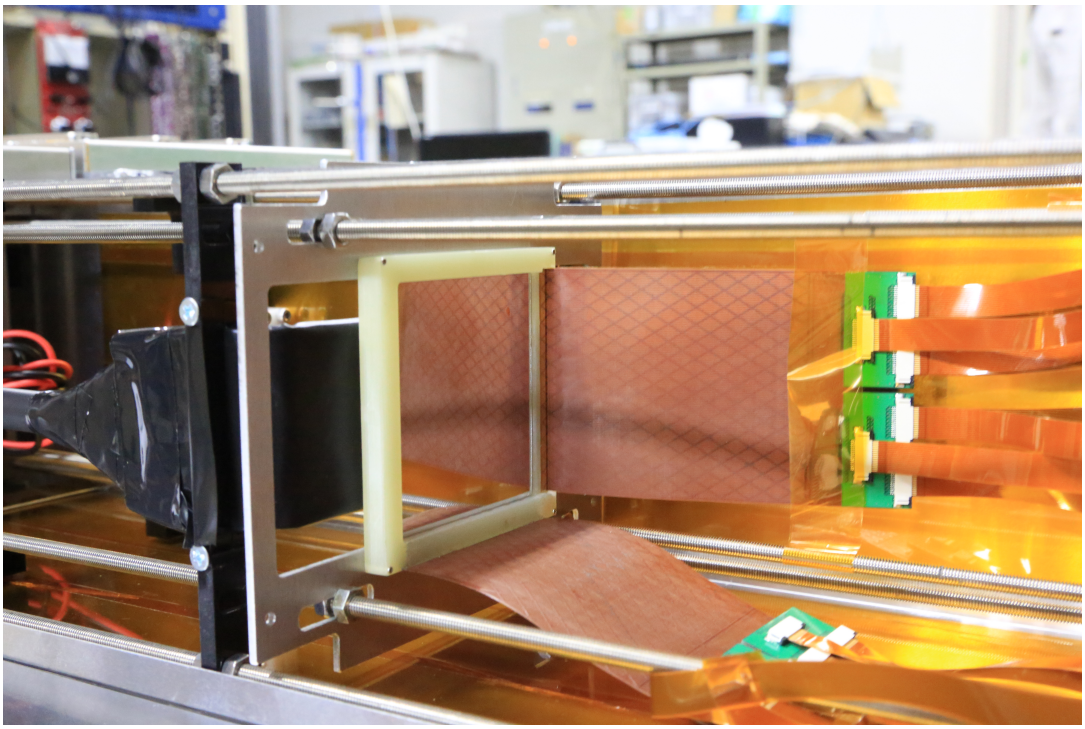

Figure 3.9: A photograph of the BB13 detector with the cabling. The cables from the detector were divided into two groups. The readout signals were connected to the feedthroughs located upstream and downstream of the chamber. Photo courtesy of J. Wu and S. Nishimura [103].

in the strip with the largest energy deposition, with the neighbouring strips having less energy deposited. Using the rise time of the signal, the largest energy deposition in a strip is expected to have the fastest timing signal, as the pulse will rise fastest past the discrimination level of the TDC. To find the implantation position in the offline analysis, the DSSSD is first checked for energy signals, i.e. energy deposition in the overflow of the ADC. The implantation is localised at the intersection of the x- and y- strips with the fastest timing.

3.4.7 Calibration of the DSSSD

Calibrations are necessary to accurately measure the energy deposited by the β^+-decays. In cases where the β^+ particle deposits energy in more than one pixel in the DSSSD, the energy is used to determine the position of interaction. This will be discussed in the next chapter. Absolute energy calibrations for WAS3ABi were performed using a ^{207}Bi source, which emits mono-energetic conversion electrons of 482- and 976- keV (K lines) as shown

in Fig. 3.10.

A ^{207}Bi source was placed inside the WAS3ABi chamber and the data acquisition triggered with WAS3ABi. Each peak of the 128 energy spectra of the DSSSD detector was individually fitted with a Gaussian function. The resulting centroids were used to perform a linear fit of the energy values. A resolution of 28±8 keV FWHM was achieved for WAS3ABi.

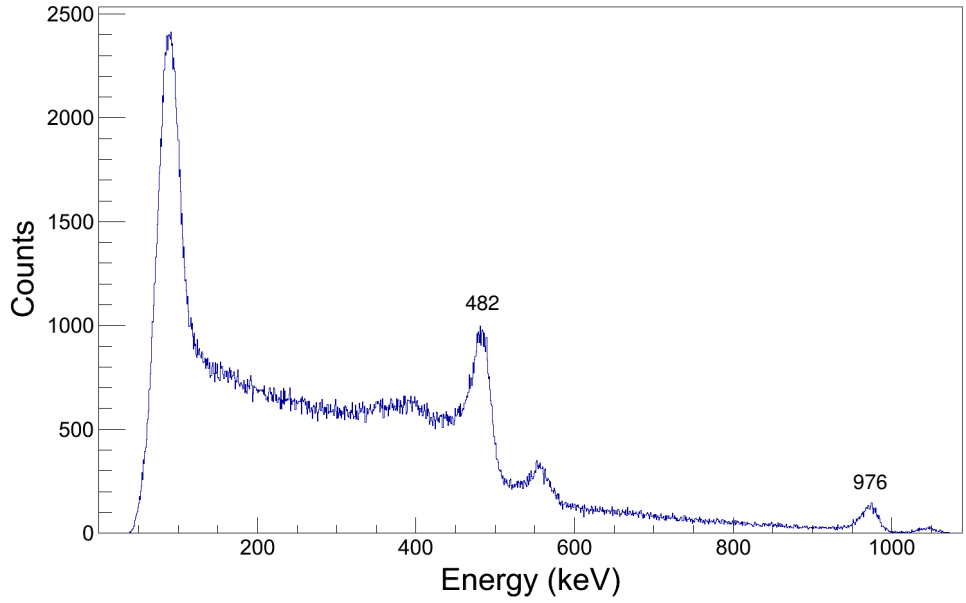

Figure 3.10: An absolute energy calibration spectrum for WAS3ABi. Calibrations were performed using a ^{207}Bi source which emits mono-energetic conversion electrons of 482- and 976- keV (K lines).

3.5 Settings

For RIBF97 two BigRIPS settings were used for the maximum transmission of ^{73}Sr and ^{74}Sr ions. The optimal configuration of BigRIPS for dipole magnets and slits at the focal planes were determined based on LISE^{++} simulations [105] to find the optimal beam transmission for the transmission of ^{73}Sr and ^{74}Sr. Table 3.1 displays the slit widths at focal planes F1, F2, F5, and F7 used for the ^{73}Sr, ^{74}Sr settings, and an additional sub setting, which was used by the BigRIPS team to search for new isotopes. Adjusting the widths of the slits at F1, F2, F5, F7, and the F5 wedge allowed for the optimisation for transmission of nuclei. The predicted counts of nuclei from LISE^{++} calculations for the

experiment are presented in Table. 3.2.

Table 3.1: The slit widths (left and right), at a foci, for each of the run settings used for RIBF97.

Setting	F1 [mm]	F2 [mm]	F5 [mm]	F7 [mm]
^{73}Sr	L 64.2 / R 0	L 3 / R 5	L 0 / R 120	L 2 / R 10
^{74}Sr	L 64.2 / R 5	L 25 / R 9	L0 / R 120	L 8 / R 10
Sub setting	L 64.2 / R 30	L 14 / R 8	L5 / R 120	L 6 / R 14

Table 3.2: The predicted count rates from the LISE++ calculations for the two-day run. Isotopes labelled with an asterisk have not been previously observed.

Setting	Nucleus	Total Counts
1	^{73}Sr	2500
1	^{74}Sr	100
2	^{74}Sr	8000
2	^{76}Y	4000
2	^{75}Y	200*
2	^{77}Zr	100*

The BigRIPS configuration for Bρ at the focal planes F1, F2, F3-5, and F5-7 are summarised and presented in Table. 3.3, displaying the Bρ settings for RIBF97. Table. 3.4 displays the settings for the material thickness of the degraders located at the focal planes F1 and F5. The run conditions of the two settings, ^{73}Sr and ^{74}Sr, are listed in Table. 3.5. The values in Table. 3.6, are the actual count rates from this experiment for the two settings, which differ from those in Table. 3.2. The number of events experimentally observed was considerably less than predicted by the LISE^{++} calculations. It is suggested that this was due to the experimental cross-sections being much lower than previous experimental results and theoretical model predictions.

Table 3.3: The settings for Bρ at focal planes, i.e. Bρ_{57} is F5 and F7, for RIBF97.

$B\rho$ (Tm)			
$B\rho_{01}$	$B\rho_{12}$	$B\rho_{35}$	$B\rho_{57}$
5.110	4.432	4.399	3.6055

Table 3.4: The settings for the target material thicknesses, and F1 and F5 degraders for RIBF97.

	Target	$F1_{deg}$	$F5_{deg}$
Material	Be 4 mm	Al 4 mm	Al 3.5 mm

Table 3.5: Summary of the run conditions during the two-day run for RIBF97. The two main settings for the implantation of ^{73}Sr and ^{74}Sr ions are shown.

Focused nuclide	^{73}Sr	^{74}Sr
Primary beam	^{124}Xe	^{124}Xe
Beam energy (MeV/u)	345	345
Time of data taking (Hours)	45	9
Number of total implantations	186	589

Table 3.6: The total number of observed events for various nuclei identified, for each setting, during the two-day run for RIBF97.

Setting	Nucleus	Total Counts
^{73}Sr	^{71}Kr	89156
^{73}Sr	^{72}Kr	87746
^{73}Sr	^{73}Sr	186
^{73}Sr	^{74}Sr	1
^{73}Sr	^{75}Sr	0
^{74}Sr	^{74}Sr	589
^{74}Sr	^{75}Sr	9694
^{74}Sr	^{76}Y	51
^{74}Sr	^{75}Y	0
^{74}Sr	^{77}Zr	1

Chapter 4

Data analysis and statistical methods

In general, data produced and recorded during an experiment must undergo further detailed and rigorous analysis. Electrical signals were generated by detectors, the signals were digitised and acquired through an electronic data acquisition (DAQ) system in the experimental set-up in this work. Raw data were collected during the experiment, encoded and written to a computer file for further processing in online or offline analysis. Raw data can be then transformed into manageable and physically meaningful data. The data analysed in this thesis were generated by three main detector systems: BigRIPS, WAS3ABi, and EURICA as described in the previous chapter. To properly process the basic signals into a form from which the physics of interest can be extracted the detectors must be calibrated, and their performance must be understood. The processing, calibrations, corrections, and analysis of data collected during the experiment as described in Chapter 3 are discussed in this chapter. Particle identification plots which are used for analysis are displayed in this chapter. The construction, analysis and statistical methods for experimental decay curves are also presented in the following chapter.

4.1 Data acquisition

Three independent DAQ systems were operated in parallel to independently record data(BigRIPS, WAS3ABi, and EURICA). This method was used to improve the efficiency of data collection, and to reduce the dead time during data acquisition. Some of the BigRIPS signals were also fed into the DAQs of the EURICA and WAS3ABi for online analysis. The data

acquired from the three DAQ systems, during the experiment, were stored in different formats. Events from the three DAQ systems are reconstructed via the absolute time information called a timestamp for online or offline analysis. Therefore, it was necessary to merge the data. To achieve this a timestamp was recorded for each detector signal. The timestamp was recorded on an event-by-event basis by a Logic Unit for Programmable Operation (LUPO) module, which was installed in the three DAQ systems for time synchronisation [106]. To obtain an absolute time, a high frequency clock signal (100 MHz) was simultaneously provided to the three systems as a timestamp. A physical event triggers the data recording for the three DAQs. The digital resolution of the timestamp is 10 ns per channel, which is much shorter than the time interval between events, i.e. β-decay half-lives of the nuclei of interest, which occur over an order of ms.

BigRIPS and WAS3ABi used the RIBF DAQ, which was developed at RIKEN, a detailed description of which can be found in Ref. [107]. EURICA used the Multi Branched System (MBS), a data acquisition system developed at GSI, and for further information on this the reader is referred to Refs. [108, 109].

The DAQ system for BigRIPS included PPACs, plastic scintillators, and MUSIC previously discussed in Chapter 3. The master trigger of the BigRIPS DAQ was obtained from the plastic scintillator located at the focal plane, F7.

For WAS3ABi, energy and timing signals were recorded by 23 CAEN V785 ADCs and 6 CAEN V1190 TDCs, which were arranged in two VME crates [110]. Data from the VME crates were read by a VMI/VME controller installed in a master VME crate. The expected dead time was less than one millisecond for an implantation event, and a dead time of less than 500 μs could be achieved for a β-decay event with threshold for the ADCs [110]. The master trigger of the EURICA DAQ system and WAS3ABi DAQ system was obtained from the logic OR between the plastic scintillator at F11 and a SUM of front-back coincidence over the DSSSD. The resultant hybrid trigger was to record γ-rays from isomeric states and β-delayed γ-rays.

4.2 Raw data

For all detectors in BigRIPS, WAS3ABi, and EURICA the individual electronic channels were assigned to the corresponding detector signals. The necessary calibrations for WAS3ABi were performed as discussed in the previous chapter. The BigRIPS data processing were performed by the BigRIPS team. The BigRIPS data underwent further

processing to calculate the mass-to-charge ratio and nuclear charge. The BigRIPS team provided a ROOT-File [111] with the calculated A/Q and Z data, and these data were then merged with the EURICA and WAS3ABi data. The EURICA and BigRIPS calibrations were performed by the EURICA and BigRIPS teams, respectively, as part of the framework of the EURICA campaign. The object-oriented system Go4 (GSI Object Oriented online offline system) [112] was an analysis code developed by the EURICA collaboration. This software was used for the EURICA data and to assign the individual electronic channels to the corresponding detectors. The ANAROOT tool kit is an offline merging software, developed at RIKEN, was used for the WAS3ABi data. This software was optimised for the analysis of RIDF (RIBF Data Format) raw data produced by RIBF DAQ system [113].

4.3 Merging of data between the DAQ systems

Merging and reconstructing data from the individual DAQ systems (WAS3ABi, EURICA, and BigRIPS) was required for use in ion-β, ion-γ or ion-β-γ correlations. The timestamp, mentioned previously, was used as part of the merging process for the three DAQ systems. This was achieved by evaluating the constant offset in the timestamp difference (ΔTS) between any two of the three DAQ systems. It should be noted that due to different cable lengths and delays that the timestamps of one system in comparison to another system may have an offset. An offset $\mathrm{TS_{offset}}$ had to be determined, and taken into account for the correlation of events in the merging process.

4.4 Particle identification plots

The secondary beam, purified by the first stage of BigRIPS, was a cocktail beam containing a large number of fragment products with different A and Z. This beam was implanted into WAS3ABi. Therefore, a particle identification (PID) plot was necessary to tag all the implanted fragments for the subsequent analysis. The PID provided the atomic number, Z, and mass-to-charge ratio, A/Q, of fragments, by measuring energy loss, magnetic rigidity and time-of-flight (ΔE-Bρ-TOF) as described in Section. 3.2.2. The particle identification of the implanted ion species was provided by the BigRIPS team. The average A/Q resolution was determined to be as 0.06%.

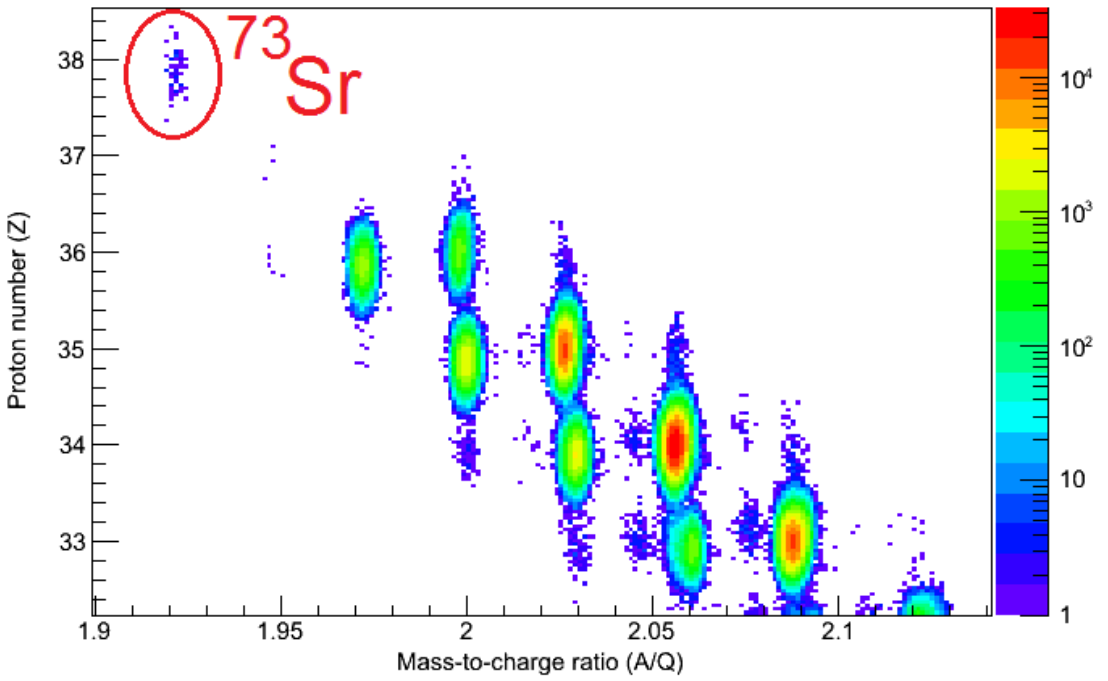

Figure 4.1: Particle identification plot of all implanted ions in the ^{73}Sr setting RIBF, at the RIKEN facility. The PID plot shows the measured mass-to-charge ratio, (A/Q), in BigRIPS using the F3-F5 ToF measurement versus the deduced nuclear charge, Z, from the F11 ionisation chamber. The colour scale represents the number of measurements.

Shown in Fig. 4.1, the setting of BigRIPS was set for the maximum transmission of ^{73}Sr. Two isotones are clearly established. A few events for ^{72}Rb can be seen. Shown in Fig. 4.2, is the setting for the maximum transmission of ^{74}Sr. Three isotones are clearly established. No events of ^{73}Rb are seen. Further cleaning of the PID plots was provided by Suzuki [114]. The results from the PID plots will be discussed in more detail in Section. 6.

The remaining events between each nuclei, in the PID plots, originate from proton-knockout at the F5 degrader [114]. These events could not be removed completely due to the limited resolution of the detector.

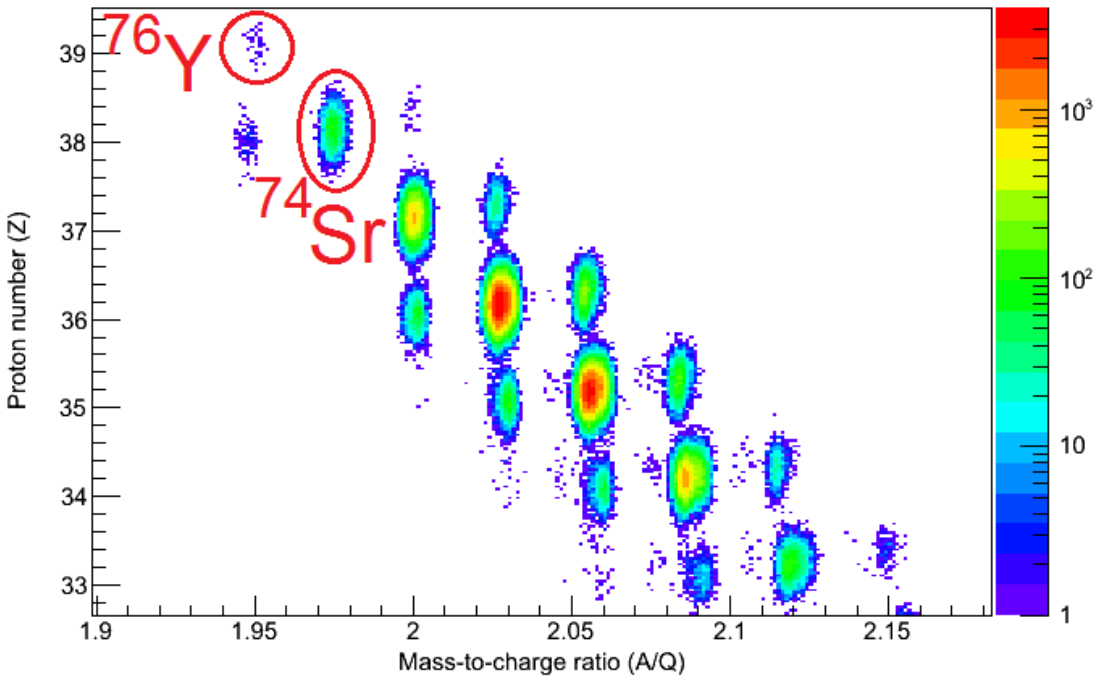

Figure 4.2: Particle identification plot of all implanted ions in the ^{74}Sr setting. The PID plot showing the measured mass-to-charge ratio (A/Q) in BigRIPS using the F3-F5 ToF measurement versus the deduced nuclear charge, Z, from the F11 ionisation chamber.

4.5 β-decay events

β and β-proton decay events were associated with preceding heavy-ion implantations based on position and time information from the active stopper, WAS3ABi. A prerequisite for the correlation analysis was the proper identification of the implanted ion species, which was provided by the BigRIPS team and are shown in Fig. 4.1 and Fig. 4.2. Contributions from other nuclear species implanted in the WAS3ABi detector were strongly suppressed by requiring a maximum total implantation rate of 70 pps in the array.

β-decays from ions implanted in WAS3ABi, created a trigger for data acquisition from their emitted positrons. To create the β-decay trigger, the sum outputs of the discriminators for each DSSSD were used. An energy deposition above threshold was required in at least one x- and one y-strip of the DSSSD measured in coincidence. β particles often deposit energy in several neighbouring strips due to the thin strips of the DSSSD. If energies are deposited in several strips, then the full energy of the β particle can be reconstructed.

To reduce the probability of summing energies of β particles emitted in random coincidence, only neighbouring strips of the implantation were considered. Non-neighbouring strips were treated as independent energy depositions from different β particles.

In general, for the data analysis, the position-correlation area was cross-shaped, i.e. the pixel where the decay event occurred, plus the four neighbouring pixels (two pixels in horizontal and two pixels in vertical directions), or a single-pixel window that only consisted of the pixel where the decay event occurred as shown in Fig. 4.3 unless otherwise stated.

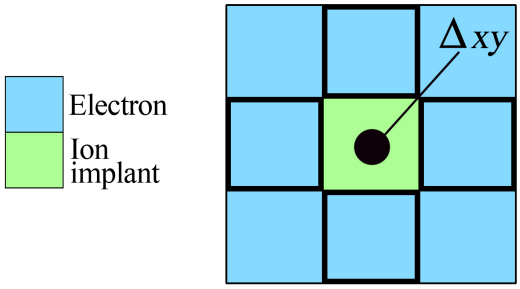

Figure 4.3: A schematic representation of the Δxy method used to determine the implantation position in WAS3ABi. If an ion is implanted in a pixel, a search for a subsequent β decay is conducted. The only pixels considered in the search were where the decay event occurred, plus the four neighbouring pixels (two pixels in the horizontal and two pixels in the vertical direction). Figure from [47].

The position-correlation, Δxy, was determined as:

$$\Delta xy = \sqrt{(ion_x - \beta_x)^2 + (ion_y - \beta_y)^2}, \tag{4.1}$$

where Δxy is the distance between implantation and β-decay and is measured in mm. ion$_x$ and β_x are an ion and β particle implanted in the x-strip of the DSSSD and ion$_y$ and β_y are an ion and β particle implanted in the y-strip of the DSSSD. This area was determined by comparing the position-correlations of single, cross-shaped and a square (all surrounding pixels of implantation) and the effect of the background radiation in relation to the positions.

Given the low maximum implantation rate per pixel of about 4.3×10^{-3}s and the predicted β-decay rate, the probability of multiple implantation events correlated with a decay was negligible.

Timing information is recorded on an event-by-event basis in WAS3ABi. The decay time is the difference between a β-decay correlated with an ion implanted ($t_{Decay,ts}$) and the time-stamp with the implantation of the correlated ion ($t_{Imp,ts}$) [115]:

$$t^i_{Decay} = t^i_{Decay,ts} - t_{Imp,ts}. \tag{4.2}$$

Where the superscript i denotes the index of the decay, $i = 1$ is the first decay correlated with the implanted ion after the implantation, $i = 2$ the second decay and so forth.

The time window for ion-β correlations is recorded for a time interval of 1 s. As this value exceeds the expected half-lives of the nuclei in this work, the subsequent generations of decays must also be taken into account in the fitting procedure. This will be discussed later in this chapter.

When constructing the decay curves, it can be argued whether to use a constant or an exponential background in the decay curve. Contaminations produced by secondary reactions degrader were expected to be implanted in the Si detector. An exponential would be suitable if the radioactivity from the contaminations are not negligible. A constant background is a good approximation for the simplification of the analysis to determine the half-life. This method was used in Refs. [116] and [117].

4.6 β-delayed protons

β-decay events can be accompanied by proton emission. The protons should deposit all of their energy in the DSSSD because of their higher stopping power. The energy of decay events in the DSSSD is the sum of the proton energy and part of the β energy deposited in a given pixel. This summing effect shifts the peak centroids to higher energies, and distorts the shape of the observed spectrum. It is possible to account for the summing through a suitable simulation. The energy-loss of β-particles, and electrons from internal conversion, contribute to the lower energy region of the spectrum the expected form. βp events contribute to the higher-energy region of the spectrum. The βp-energy spectra includes a contribution from summing with the simultaneously emitted β-particle and proton.

To determine the branching ratios for β-delayed proton emission this required the separation of β-decay events and βp decay events. The two distributions can overlap, and so the separation of the βp events was based on energy deposition. β-particles are expected

to deposit less than 1 MeV in a single pixel in the detector. In comparison, protons in this mass region typically have energies above 1 MeV, due to the Coulomb barrier, and therefore are expected to deposit more than 1 MeV in a single pixel. βp events were identified by requiring an energy deposition of more than 1 MeV in the implantation pixel or in the neighbouring pixels (i.e. the cross-shaped position-correlation).

The number of implants observed in BigRIPS were compared to the number of implants in WAS3ABi, then the efficiency of ion implantation was calculated. To determine the β-proton branching ratio of the nuclide, the total intensity of the proton spectrum was divided by the total production rate of the ions, and the efficiency of ion implantation was considered thus:

$$\beta p \ = \ \frac{N_{protons}}{N_{implantations}}. \tag{4.3}$$

4.7 γ decay

The three forms of γ-ray interactions with Ge detectors are the photoelectric effect, Compton scattering and, when E $> 2m_ec^2$, pair-production. In photoelectric absorption, the full energy of the γ-ray is deposited in one crystal of the array. In the case of Compton scattering, a γ-ray can Compton scatter from a crystal and the energy can be distributed over a number of crystals.

4.7.1 Add-back

If the energy of a γ-ray is distributed over a number of crystals following Compton scattering, it is possible to reconstruct the full energy of the γ-ray. The energies deposited from the γ-ray in multiple crystals can be summed to reconstruct the full energy. This procedure is known as add-back. The add-back procedure is implemented during offline analysis to increase the photopeak efficiency and decrease Compton background. Add-pack is used to identify which crystals an individual γ-ray has deposited energy.

The energies of different crystals can only summed together if they are a direct neighbour, and are within set time and energy conditions. The crystals have to be direct neighbours within one cluster. Otherwise, the measured energies were treated as independent energy depositions from different γ-rays. The travel time of the Compton scattered γ-rays to the adjacent crystals is small compared to the timing resolution of the DGF. Therefore, the energies were only summed if the energy deposition was in prompt coincidence to each

other. The three different ways of γ-ray interaction with matter have different contributions for different energies. The contribution for low energies is dominated by photoelectric absorption, whilst for higher energies the two other effects dominate. A lower energy limit is set within the add-back algorithm to avoid the summation of low energy γ-rays.

4.7.2 Energy-time matrix

To analyse the data recorded in coincidence with the implanted ions, a γ-ray energy versus time matrix was created for each of the nuclei of interest. An example of the energy-time matrix is shown in Fig. 4.4. The energy of the γ-ray is plotted versus the timing with respect to the implantation trigger. Gates were placed on the energy axis in order to project the time spectra. Timing information was extracted using TDCl (long range time-to-digital converter) and DGF (digital gamma finder) readout with resolutions of 0.73 ns/channel and 25 ns/channel, respectively. The DGF has a much higher absolute efficiency for low energy γ-rays.

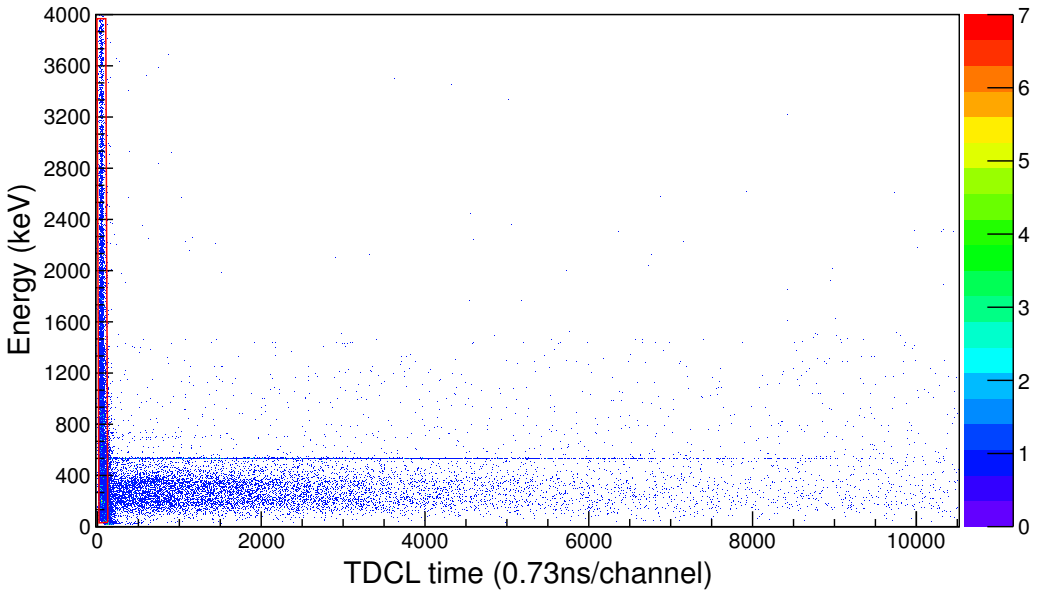

Figure 4.4: γ-ray energy versus TDCL time matrix for ^{69}Se. The gate shown in the red colour is set around the prompt flash. The transitions arising from isomeric states are first identified in the matrix as the horizontal lines starting in the prompt radiation peak and losing intensity over time.

An energy-time matrix for a ^{69}Se ion is shown in Fig. 4.4. A ^{69}Se ion is identified

in BigRIPS, that has triggered the data acquisition system, and then implanted into the active stopper WAS3ABi. The trigger opened a gate of 110 μs for the DGF and TDCl, allowing the observation of γ-rays in delayed coincidence with the implantation following the decay of the isomeric state. A gate, shown in red in Fig. 4.4, is set around the prompt flash, to be discussed further in Section. 4.7.3, is removed to obtain a cleaner spectra, and to be able to identify isomeric transitions.

Horizontal lines with a strong, losing intensity over time can be identified as isomeric states. A two-dimensional gate is placed on the prompt flash to achieve the optimal peak-to-background ratio and to reduce data loss. To obtain an energy/time spectrum, after removing the prompt flash, the gate is projected on the energy/time axis. The resulting plot(s) can be used to identify the transitions below the isomeric state.

4.7.3 Prompt flash

High-energy ions and material at the final focal plane (F11) interact, which leads to a large flux of electromagnetic radiation, observed by the Ge detectors (EURICA). This burst of energy observed at the time of implantation is known as the prompt flash and results in a huge amount of unwanted background radiation. The prompt background radiation has its origins in radiative electron capture and Bremsstrahlung [1].

The large background radiation created by the prompt flash, particularly that below 100 keV, can cause a poor time resolution at these energies due the spread of the flash over a large number of time bins. The prompt flash causes many photons to be emitted simultaneously, which blinds many detectors in EURICA from detecting the γ-rays of interest. A detector is deemed to be paralysed if a detector is hit by a photon from the flash, which reduces the effective efficiency of the array [118]. The prompt flash is highlighted in red in Fig. 4.4 and it can be seen to spread over multiple time bins at lower energies.

4.7.4 Time-walk correction

One effect limiting the time resolution of detectors is the 'walk of the time' signal. The time-walk is a shift depending on the amplitude of the signal. In this case, the γ-ray

[1] Heavy ions penetrate into the active stopper, and electrons are knocked out from the stopper material that de-accelerate under the electromagnetic field of nearby atomic nuclei via photon emission [118].

implants into a crystal and produces an electric signal (charge). A discriminator produces a logic output signal, when the charge input crosses the chosen threshold. The measured time is the time at the crossing point. Due to the slower rise-time of the low energy signals, it takes longer to reach the threshold. This time difference is called time-walk. This depends on the energy of the γ-ray and can be determined in a fitting process.

To determine the time-walk correction an energy time matrix was created. For each energy bin, a one-dimensional time projection was created, the bin with the largest peak was used to subtract from the timing information and an offset to zero was created. All subsequent references to γ-ray times have this correction implemented.

4.8 Decay-curve fitting

By measuring the time distribution between the implantation of an ion and its subsequent β-decay, the identifying β-decay of a specific nuclide can be deduced. Decay curves were constructed using the time distribution between an implantation and a correlated β-decay. Two methods were applied to the fitting analysis of the decay curve depending on the statistics of the data. For a higher number of statistics the preferred method involved the χ^2 minimisation fit technique by solving the Bateman equations, and this method will be referred in the text as the χ^2 method. The second method was used for nuclei produced in the present work with low yields, in this case the half-lives were determined by the logarithmic binning method as described by Schmidt in Refs. [119] and [120]. This will be referred in the text as the Schmidt method. The full development and formal description of the χ^2 methods has been described previously in Refs. [110, 115], thus only a brief summary will be provided here.

4.8.1 Bateman equations and χ^2 minimisation fit

To construct decay curves one must consider the probability that the time distribution of the β-decay has contributions from the parent nuclei, and also the daughter and the subsequent progeny that form the decay chain. The Bateman equation [121] is a mathematical model describing abundances and activities in a decay chain as a function of time, based on the decay rates and initial abundances. The fitting function has to consider the parameters for the initial abundance N_0 and the β-decay half-life of the mother nucleus, the half-lives of the nuclei produced along the decay chain (initiated by the parent nuclei),

and an appropriate background. This method is useful for cases where the parent and daughter nuclei have similar half-lives and a high number of statistics. A brief summary of the steps involved are given below. A more detailed description is given in Ref [122].

If a decay constant λ_1 can be assumed for the nuclide ${}^{A}_{Z}X_1$, the number of ${}^{A}_{Z}X_1$ decaying in a unit of time can be described as:

$$\frac{dN_1}{dt} = -\lambda_1 N_1(t), \tag{4.4}$$

with

$$X_i = \frac{dN_i}{dt}. \tag{4.5}$$

The number of nuclei decaying in a unit time as a function of time is obtained by summing the time differentials:

$$\frac{dN_i}{dt} = -\sum_i \lambda_i X_i(t) + C, \tag{4.6}$$

where the β-decay half-life of the parent, which is given by $t_{1/2} = ln(2)/\lambda_1$, can be obtained by fitting Eqn. 4.6 to the decay spectrum gated on the implantation of ${}^{A}_{Z}X_1$.

The general solution describes the number of nuclei of the n-th isotope, $N_n(t)$, with decay constant, λ_n, at a time, t, involved in a decay chain with the following formula [121]:

$$N_n(t) = \prod_{j=1}^{n-1} \lambda_j \sum_{i=1}^{n} \sum_{j=1}^{n} \left(\frac{N_i(o) e^{-\lambda_j t}}{\pi^{n}_{p=i,p\neq j}(\lambda_p - \lambda j)} \right), \tag{4.7}$$

where λ_j is the decay constant of the j-th precursor.

The total decay spectrum as a function of decay time, t, (Eqn. 4.6) is denoted as $f(t_i; a)$, where the n variable a represents the β-decay of the parent nuclide to be determined by the fitting analysis. The χ^2 is minimised to obtain a half-life [123]. χ^2-fitting tries to minimise:

$$\chi^2 = \sum_{i=1}^{N} \left[\frac{N(t_i) - f(t_i; a)}{\sigma_i} \right]^2, \tag{4.8}$$

in which the index, N, is the total bin number in the time histogram. t_i and $\mathrm{N(t}_i)$ are the central time and number of counts in the i-th bin, respectively, and σ_i is the statistical uncertainty in the i-th bin obtained from the number of counts as:

$$\sigma_i = \sqrt{N(t_i)}. \tag{4.9}$$

The three free fitting parameters are the decay constant of the parent nucleus λ_1, the initial abundance N_o, and a constant background c. This method of reconstructing the data are chosen as it can be assumed that the background originates from only time random

correlations, which can be accounted for by a constant component in the fit. The a best reproducing $N(t)$ with $f(t_i; a)$ is the estimate of the β-decay half-life of the parent nuclide. The χ^2 function is minimised using the ROOT [111] implementation of MINUIT [124].

The χ^2 minimisation generally has some limitations. When the counts per bin are low this can lead to a bias in the results [125]. The bin size has to be chosen appropriately, as re-binning can subsequently lead to loss of information. In the cases with sufficient statistics the binning can be chosen fine enough to maintain the shape of the decay curves to extract half-lives, but for low statistics cases, for example with fewer than 100 events, another method is needed to achieve reliable results.

4.8.2 Schmidt method and maximum likelihood fit

The maximum likelihood (MLH) fit is an estimation method [126]. This method is useful for cases where there are very few statistics in the time bins and the probability distribution is known. In this method, one assumes that the data follows an exponential decay, with no linear background or daughter decays, and that the length of time between events is longer than the implants in the same pixel. For a pre-determined function, the MLH method gives the parameters of a curve that is most likely to have produced that data. This method is useful for when the parent and daughter nuclei have different half-lives (i.e. a different order of magnitude) and is suitable for a low number of statistics.

The probability for a state with mean lifetime τ to decay after an observed time t is given by [127]:

$$P(t;\tau) = \frac{1}{\tau} e^{-t/\tau}. \tag{4.10}$$

The log likelihood for N measurements t_1 ... t_N is:

$$\ln L = -N\frac{\bar{t}}{\tau} - N\ln\tau. \tag{4.11}$$

Where $\bar{t} = \frac{1}{N}\sum t_i$ and L (the likelihood function), is the product of the individual probabilities. Differentiating with respect to τ gives:

$$\frac{d(\ln L)}{d\tau} = -\sum\left(\frac{t_i}{\tau^2} - \frac{1}{\tau}\right). \tag{4.12}$$

Setting this to zero gives the maximum likelihood estimator, $\hat{\tau}$:

$$\sum\left(\frac{t_i}{\hat{\tau}^2} - \frac{1}{\hat{\tau}}\right) = 0, \tag{4.13}$$

$$\hat{\tau} = \frac{1}{N}\sum t_i. \tag{4.14}$$

Assuming that the time acceptance is τ, i.e. the observing window is known to be much larger than τ, the likelihood function is then given for N counts [126] as:

$$L = \prod_{i=1}^{N} \frac{1}{\tau} e^{-t_i/\tau}, \tag{4.15}$$

where t_m is the time of the m^{th} count. Here, N refers to the number of total decay events rather than the number of bins. Taking the natural logarithm and differentiating with respect to time gives:

$$\hat{\tau} = \frac{1}{N} \sum_i t_i + \frac{\tau e^{\tau/\hat{\tau}}}{1 - e^{\tau/\hat{\tau}}}. \tag{4.16}$$

The best estimator for τ, $\overline{\tau}$, is the mean of t_i.

The binned ML method has the advantage over the χ^2 method that the fit does not critically depend on the number of counts per bin. However, appropriately accounting for any kind of background can be difficult.

For nuclei with insufficient statistics with which to attempt the previous method, the half-lives can be determined by the logarithmic binning method as described by Schmidt in Refs. [119] and [120]. The number of radioactive decay events is plotted against the natural logarithm of the time difference between ion implantation and β-particle detection. The β-decay half-life can then be extracted from the centroid of the bell-shaped time distribution as shown in Fig. 4.5.

Instead of plotting a linear ΔT, the natural logarithm as described above, ln(ΔT) can be considered. For a radioactive decay, the linear decay time frequency distribution is given by:

$$\frac{dn}{dT} = -N\lambda e^{-\lambda t}. \tag{4.17}$$

In the Schmidt method, the logarithmic decay time distribution is used:

$$\frac{dn}{d(\ln T)} = -n\lambda e^{\ln T} e^{-\lambda e^{\ln T}}. \tag{4.18}$$

This results in asymmetric uncertainties [127]:

$$\sigma^+ = \frac{\overline{\tau}}{\sqrt{M} - 1}, \tag{4.19}$$

$$\sigma^- = \frac{\overline{\tau}}{\sqrt{M} + 1}, \tag{4.20}$$

where M refers to the number of counts.

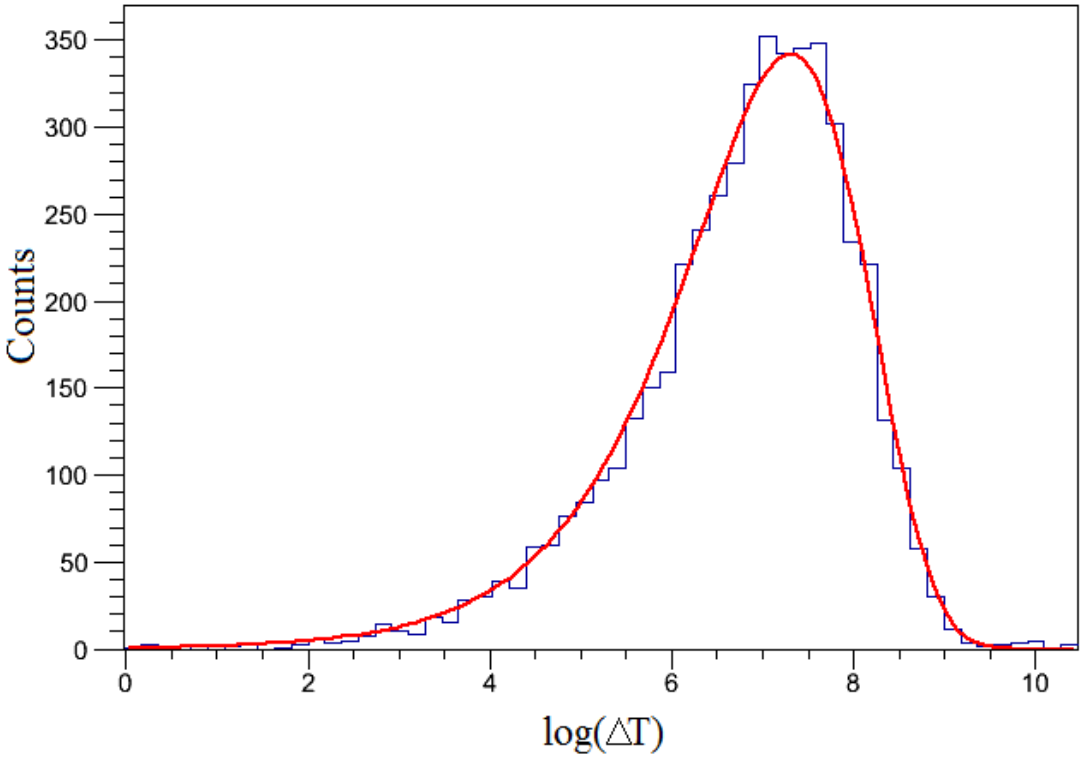

Figure 4.5: An example of the Schmidt method used in this work. The number of counts is plotted against the natural logarithm of the time distribution, ΔT. This gives rise to an asymmetric bell shaped curve. The peak in the distribution corresponds to the lifetime of the nuclide. The mean lifetime of the 534.8-keV γ-ray in ^{69}Se using the Schmidt method was found to be 1400(20) ns, and is in good agreement with the previously measured value of 1385(33) ns [128].

Chapter 5

β- and γ-decay spectroscopy

Proton-rich nuclei produced in the projectile fragmentation experiment, RIBF97, were investigated using β- and γ-decay spectroscopy. The statistical methods employed in this work are discussed in detail in Chapter 4. Additional details of the procedures of the analysis to obtain β-decay half-lives and β-delayed proton spectra are discussed this chapter. These neutron-deficient nuclei with masses A = 69–76, are on the path of the astrophysical *rp*-process. β-decay half-lives are essential for *rp*-process calculations, in order to help determine the reaction pathways. The effect of the new half-lives, and the proton-separation energy, S_p, of ^{73}Rb extracted from the β-delayed proton spectrum of ^{73}Sr, measured in this work, were used in a one-zone X-ray burst model and the results are reported in Chapter 7.

5.1 β-decay half-lives in the mass 70 region

One of the goals of the RIBF97 experiment was to measure the half-life of ^{74}Sr to gain a complete picture of the two-proton-capture branch for the ^{72}Kr waiting point. Following the identification an isotope, the time distribution of β-decay events were fitted with a decay curve to determine the half-life. As described in Section. 4, the β-ion position correlation area was cross shaped. Two methods, depending on statistics, were used to determine the β-decay half-lives of ground state nuclei as previously discussed in Section. 4.8. In cases where the lifetimes of the daughter or grand-daughter are known, these values were taken from the published literature. This has the effect of reducing the number of fitting parameters required and consequently, reducing the error on the measurement of half-lives in this work.

5.2 Half-lives fitted using the χ^2 method

To test the validity of the analysis technique to remeasure the half-life of ^{74}Sr with higher precision, known half-lives of ^{70}Br, ^{71}Kr, ^{74}Rb and ^{75}Sr were remeasured and compared to the literature. It should be noted that for daughter nuclei with half-lives with an order of magnitude difference (i.e. ms for the parent and s for the daughter) could be neglected for the fit, as they are not expected to contribute to the half-life of the parent within the time range chosen.

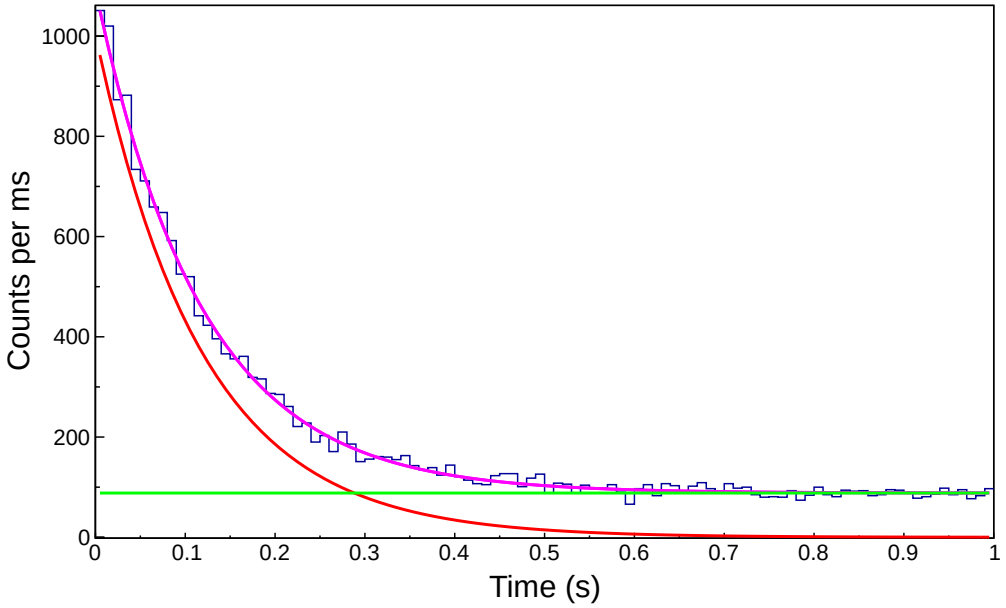

Figure 5.1: The time distribution of the β-decay events following the identification of ^{70}Br nuclei. A decay time fitted with an exponential decay (red) and a constant background (green) resulting in the combined fit (magenta). The half-life extracted for ^{70}Br = 79.7(24) ms is in good agreement with the literature half-life of 79.1(8) ms [129].

The time distribution of β-decay events correlated with the identification of ^{70}Br nuclei is shown in Fig. 5.1. For ^{70}Br, 27696 events were identified in BigRIPS. The decay of the daughter nuclide, ^{70}Se, whose β-decay is known to be 41.1(3) min [130], could be neglected as it is not expected to contribute to the half-life of the parent. A constant background (green) was fitted (as previously discussed) and this yielded a combined fit (magenta). A half-life, $T_{1/2}$, of 79.7(24) ms was extracted for ^{70}Br. This agrees very well with the literature half-life value of 79.1(8) ms [129].

The results for ^{71}Kr, ^{74}Rb and ^{75}Sr are presented in Table. 5.1. The values extracted in this work are consistent with the literature half-life values. For ^{75}Sr, a half-life of 81.7(34) ms is consistent with the currently accepted literature half-life value of 88(3) ms from the decay curves of $\beta\gamma$ and pγ spectra [82]. Other half-life values for ^{75}Sr include 87(3) ms [131], 89(5) ms [132], 80^{+400}_{-40} ms [133].

Table 5.1: β-decay half-lives obtained in the present work $T^{exp}_{1/2}$ are compared with the literature values $T^{lit}_{1/2}$. Other information includes the daughter nuclide half-life, $T^{lit}_{1/2daughter}$, and the number of events observed in BigRIPS.

Nucleus	$T^{lit}_{1/2parent}$	$T^{lit}_{1/2daughter}$	Number of events	$T^{exp}_{1/2}$
^{71}Kr	100(3) ms [134]	21.4(6) s [135]	17622	98.8(3) ms
^{74}Rb	64.761(31) ms [136]	11.50(11) minutes [137]	17229	65.5(8) ms
^{75}Sr	88(3) ms [82]	19.0(12) s [138–141]	4125	81.7(34) ms

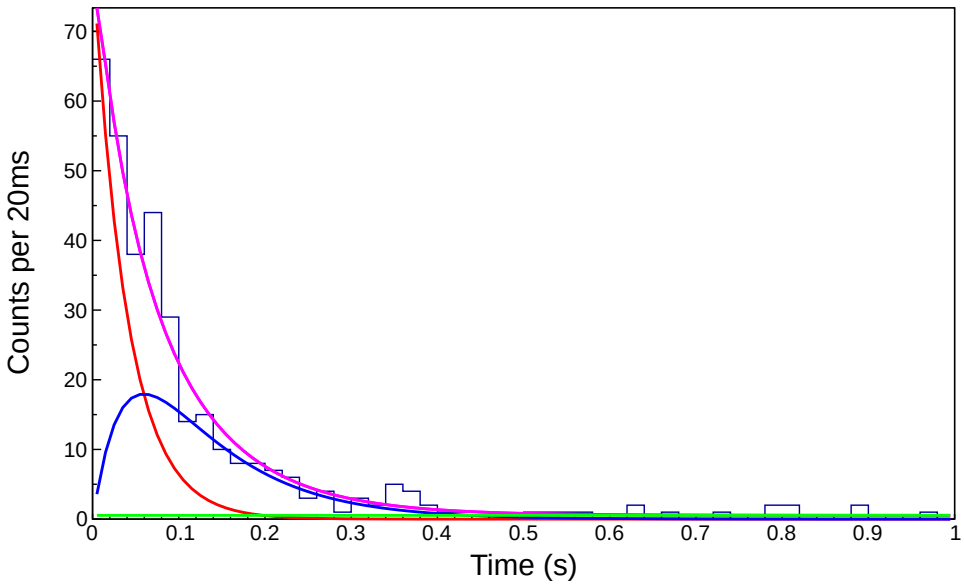

Figure 5.2: The time distribution of the β-decay events following the identification of ^{74}Sr nuclei. The red line represents the parent nuclei, ^{74}Sr. The blue line is the daughter nucleus, ^{74}Rb with a known β-decay of 64.761(31) ms [136], and the green line is a constant background. The combined fit, represented by the magenta line, yields a half-life, $T_{1/2}$ = 27.7(28) ms for ^{74}Sr.

The time distribution of the β-decay events as a function of time following the im-

plantation of ^{74}Sr nuclide is shown in Fig. 5.2. The β-decay fit of ^{74}Sr includes the activity of the daughter nuclide ^{74}Rb (the blue line), whose β-decay half-life is known to be 64.761(31) ms [136]. For ^{74}Sr a half-life of 27.7(28) ms was extracted from 361 events observed in WAS3ABi, and a total of 562 events in BigRIPS.

In 1995, ^{74}Sr was produced and identified at GANIL using Ni(^{78}Kr,X) reaction at E= 73 MeV/u. The work used the ToF method for the transit time but this work did not determine the half-life [142]. In 2013, an in-beam study of ^{74}Sr was performed at Jyväskylä using the recoil-beta-tagging technique [1]. The analysis involved γ-rays correlated with fast decays at the focal plane and were tentatively identified as transition in ^{74}Sr. From that work an estimate of the lifetime of 27(8) ms [143] was made. The half-life was extracted using the Schmidt method, with low statistics. This value agrees with the more precise value obtained from the present work.

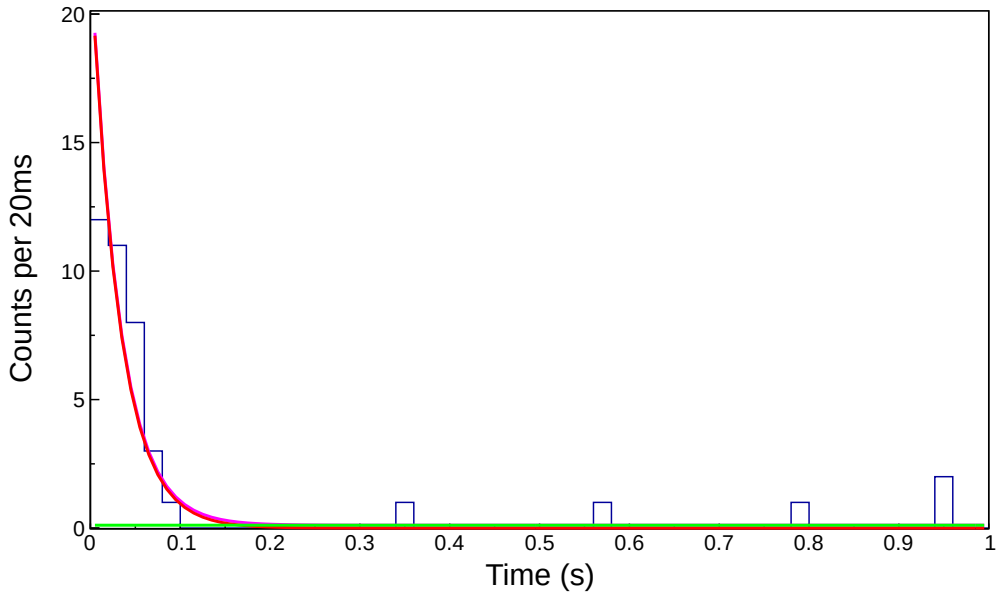

Figure 5.3: The time distribution of the β-decay events following the identification of ^{73}Sr nuclei. ^{73}Sr is represented by the red line. The green line is a constant background. The magenta line is a combined fit, which yields $T_{1/2}$= 24.3(53) ms for ^{73}Sr.

The distribution of the β-decay events as a function of time following the implantation

[1] For ^{74}Sr, this work was done at the same time as the first measurement of the half-life by Henderson *et al.* [143].

of ^{73}Sr nuclei is shown in Fig. 5.3. The β-decay half-life fit of ^{73}Sr did not include the contributions from the daughter nuclide ^{73}Rb, which is proton unbound. A half-life, $T_{1/2} = 24.3(53)$ ms for ^{73}Sr was extracted from a total of 49 events observed in WAS3ABi, and a total of 192 events in BigRIPS. No previous measurements existed for the β-decay half-life of ^{73}Sr. ^{73}Sr has been observed previously, and the half-life calculated and will be discussed further in the next section.

5.3 Half-lives determined using the Schmidt method

Due to limited statistics the half-lives of ^{73}Sr and ^{76}Y were determined using the Schmidt method [119, 120]. For ^{74}Sr, the Schmidt method was not appropriate due to the similar half-lives (∼ms) of parent and daughter nuclides. In order to confirm the validity of this method, the half-life of ^{74}Rb was determined, prior to extracting the half-lives of nuclei with unknown half-lives with the Schmidt method.

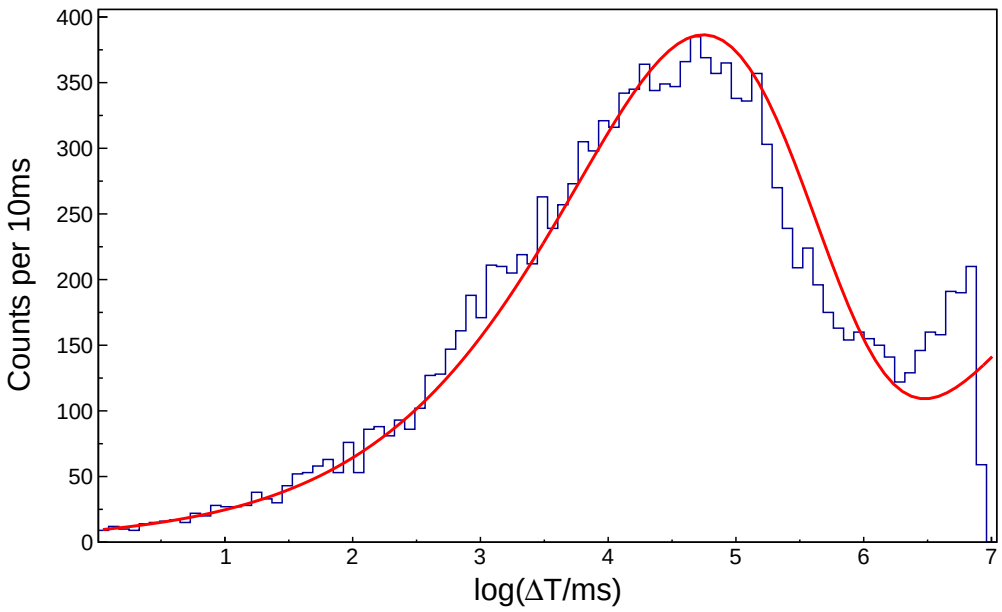

Figure 5.4: The number of radioactive decay events is plotted against the natural logarithm of the time difference between ^{74}Rb implantation and the subsequent β-decay event, using the Schmidt method to extract a $T_{1/2} = 65.0(5)$ ms, with a daughter component for ^{74}Kr of $T_{1/2}$= 11.50(11) min.

The distribution of the β-decay events as a function of time, obtained following the

identification of ^{74}Rb nuclei is shown in Fig. 5.4. The number of radioactive decay events is plotted against the natural logarithm of the time difference between ^{74}Rb implantation and a subsequent β-decay event. The half-life of ^{74}Rb was extracted from a total of 17229 events, yielding a half-life, $T_{1/2}$ = 65.0(5) ms with a daughter component for ^{74}Kr of $T_{1/2}$= 11.50(11) min. This agrees very well with the literature value 64.761(31) ms [136].

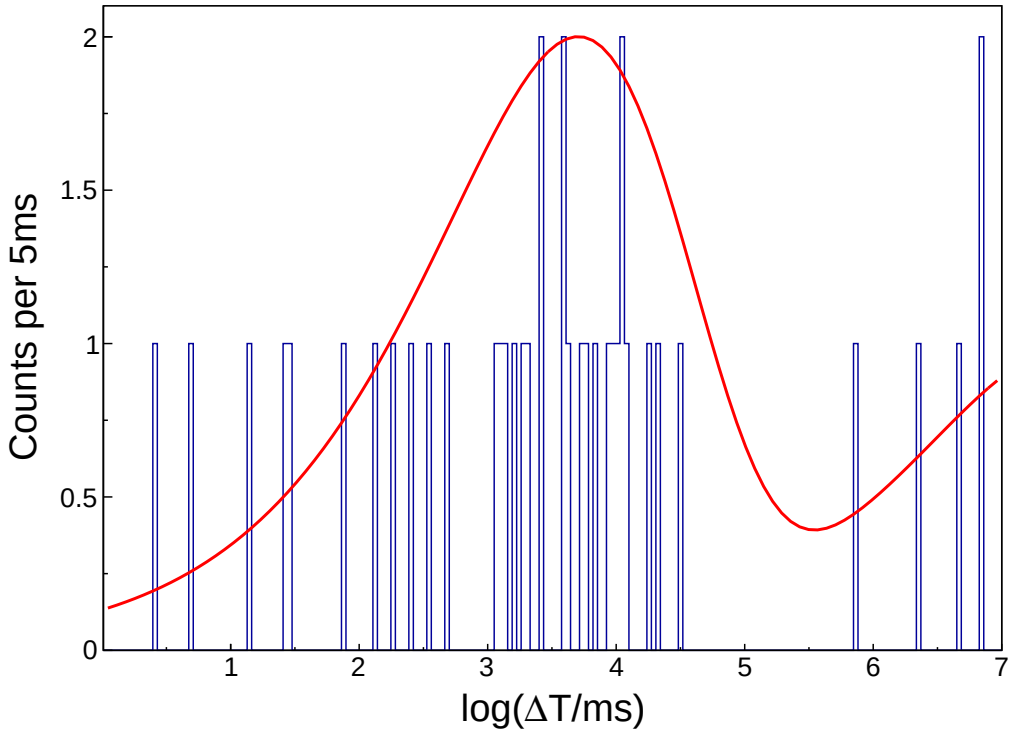

Figure 5.5: The number of counts against the logarithm time distribution of the β-decay events, obtained following the identification of ^{73}Sr nuclei. Using the Schmidt method to extract the β-decay half-life of ^{73}Sr yielded a half-life, $T_{1/2} = 28^{+5}_{-4}$ ms, assuming a daughter component for ^{72}Kr with a $T_{1/2}$= 17.1(2) s [53].

The distribution of the β-decay events as a function of time following the implantation of ^{73}Sr nuclei is shown in Fig. 5.5. It is assumed that the daughter component for ^{73}Sr is ^{72}Kr with a $T_{1/2}$= 17.1(2) s [53], as ^{73}Rb is proton unbound. For ^{73}Sr, a half-life of 28^{+5}_{-4} ms was extracted using the Schmidt method from a total of 49 correlated decay events.

In 1993, ^{73}Sr was first produced and identified by Batchelder *et al.* [81] in ^{40}Ca(^{36}Ar,3n) reaction at E=245 MeV, He-jet particle telescope. Work by Winger *et al.* [144] used a

^{58}Ni(^{78}Kr,X) reaction at E=65 MeV/u, followed by fragment, mass and charge analysis, to estimate a half-life of 25 ms from the total transit time. A β-decay half-life of 44 ms was calculated by Moller and Nix [145].

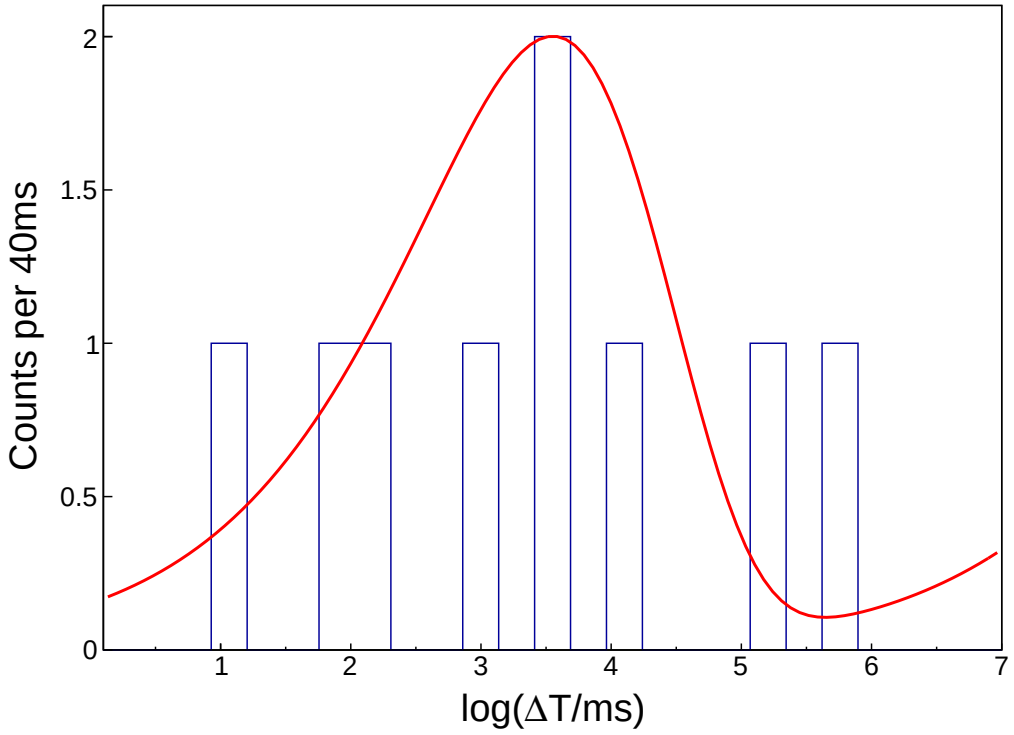

Figure 5.6: The number of counts plotted against the natural logarithm of the time distribution of the β-decay events as a function of time, obtained following the identification of ^{76}Y nuclei. Using the Schmidt method yields a $T_{1/2}$=24^{+12}_{-6} ms for ^{76}Y.

The distribution of the β-decay events as a function of time, obtained following the identification of ^{76}Y nuclei is shown in Fig. 5.6. For ^{76}Y, a $T_{1/2}$= 24^{+12}_{-6} ms was extracted from a total of 35 events observed in BigRIPS.

In 2001, ^{76}Y was produced and identified in fragmentation of a ^{122}Sn beam at 1 GeV/u on a ^{9}Be target at GSI. A total of two events were observed and assigned to ^{76}Y [131]. This work established the stability of ^{76}Y against proton emission. In 2003, Moller and Nix [145] predicted $T_{1/2}$=37.8 ms for the β-decay of ^{76}Y and calculated the proton-separation energy S_p=-0.57 MeV, which is proton unbound. Kaneko *et al.* [87] calculated single-proton separation energies of ^{76}Y to be -0.61 MeV from shell-model calculations using the JUN45 shell-model effective interactions.

5.4 Summary of half-lives from present work

The β-decay half-lives of nuclei ^{73}Sr and ^{76}Y have been measured for the first time in this work, and a half-life of ^{74}Sr has been measured with higher precision than previous work. Ground-state decay half-lives of known nuclei were also observed and measured to provide a validation of the experimental and analysis methods. The half-lives, $T_{1/2}$, obtained in the present work for various isotopes are listed in Table 5.2, and the half-lives are compared with literature values, $T^{lit}_{1/2}$ for the various isotopes.

Table 5.2: Comparison of β-decay half-lives obtained in the present work $T^{exp}_{1/2}$ with the literature values $T^{lit}_{1/2}$. Nuclei denoted by * are either calculated half-lives or limits placed on nuclei from previous experiments.

Nucleus	β-decay		
+	$T^{lit}_{1/2}$	$T^{exp}_{1/2}$	Method
^{70}Br	79.1(8) ms [129]	79.7(24) ms	χ^2
^{71}Kr	100(3) ms [134]	98.8(3) ms	χ^2
^{73}Sr	25 ms* [81]	24.3(53) ms	χ^2
^{73}Sr	25 ms* [81]	28^{+5}_{-4} ms	Schmidt
^{74}Sr	27(8) ms [143]	27.7(28) ms	χ^2
^{75}Sr	88(3) ms [82]	81.7(34) ms	χ^2
^{74}Rb	64.761(31) ms [136]	65.5(8) ms	χ^2
^{74}Rb	64.761(31) ms [136]	65.0(5) ms	Schmidt
^{76}Y	$>$ 200 ns* [131]	24^{+12}_{-6} ms	Schmidt

5.5 β-delayed protons

The prime goal of the RIBF97 experiment was to look for evidence of β-delayed protons from ^{73}Sr, in order to establish the proton-separation energy of ^{73}Rb. β-delayed proton emission provides a unique method of probing the proton-separation energy. The Fermi β-decay of the parent nucleus decays into the IAS of the daughter nucleus, if this state is above the proton-separation energy. As the proton-separation energy of ^{73}Rb corresponds to the proton capture Q-value (S_p =-Q_p) for the reaction ^{72}Kr(p,γ)^{73}Rb, the proton-separation energy for ^{73}Rb is essential for the estimation of the effective lifetime of ^{72}Kr. ^{72}Kr is a *rp*-process waiting point and this represents a path around that waiting point.

In principle, this is a test of the robustness of the waiting point.

To verify the validity of the β-delayed proton spectra of ^{73}Sr, the method of analysis was applied to known β-delayed proton emitters ^{71}Kr and ^{75}Sr. The β-delayed proton spectra of ^{71}Kr and ^{75}Sr will be discussed prior to discussing the data for the nucleus ^{73}Sr.

The total number of ^{71}Kr ions identified in BigRIPS was 92110, and of these 17796 were implanted into WAS3ABi, yielding an ion detection efficiency of 19.3%. A total of 669 of these decays were correlated with a ^{71}Kr implantation as shown in Fig. 5.7. The spectrum shown corresponds to the y-side energy values of the DSSSD. The position-correlation was cross-shaped. Events were considered if they occurred within 300 ms of implantation.

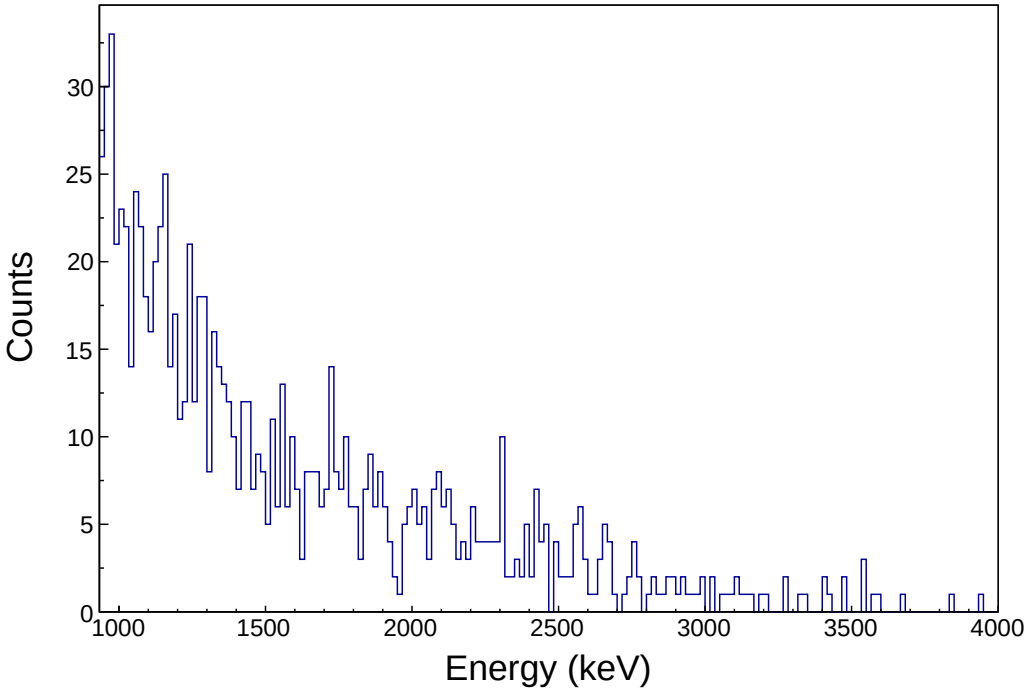

Figure 5.7: β-delayed proton spectrum for ^{71}Kr. From the β-decay of ^{71}Kr and the subsequent proton decay of ^{71}Br. The spectrum shown corresponds to the y-side energy values of the DSSSD. The position-correlation was a cross-shape. Events were considered if they occurred within 300 ms of implantation.

As a confirmation of the validity of the β-proton spectrum, the half-life of ^{71}Kr was measured by gating on the proton events, which should yield the same half-life as the β-decay half-life in principle, but with fewer background events. The half-life data are extracted by gating on the β-protons from β-delayed proton spectrum, the time distribu-

tion of the proton decay events is shown in Fig. 5.8. A half-life of 100(3) ms was deduced from the time distribution of correlated decay events using the Schmidt method, as the daughter nucleus, ^{70}Se, has β-decay is known to be 41.1(3) min [130]. This is consistent with the literature value, of $T_{1/2}$=100(3) ms [134]. A βp branching ratio of 3.8(1)% was obtained. Previous work by Oinonen *et al.* [134] at ISOLDE, obtained a value of 2.1(7)% for the β-proton branch ratio, whilst Blank *et al.* [142] at GANIL obtained a value of 5.2(6)%. There are difficulties in extracting the branching ratio, and the discrepancies come from low count rates, which can lead to large errors, β-ion-proton correlations, and where the proton implants in the silicon detector.

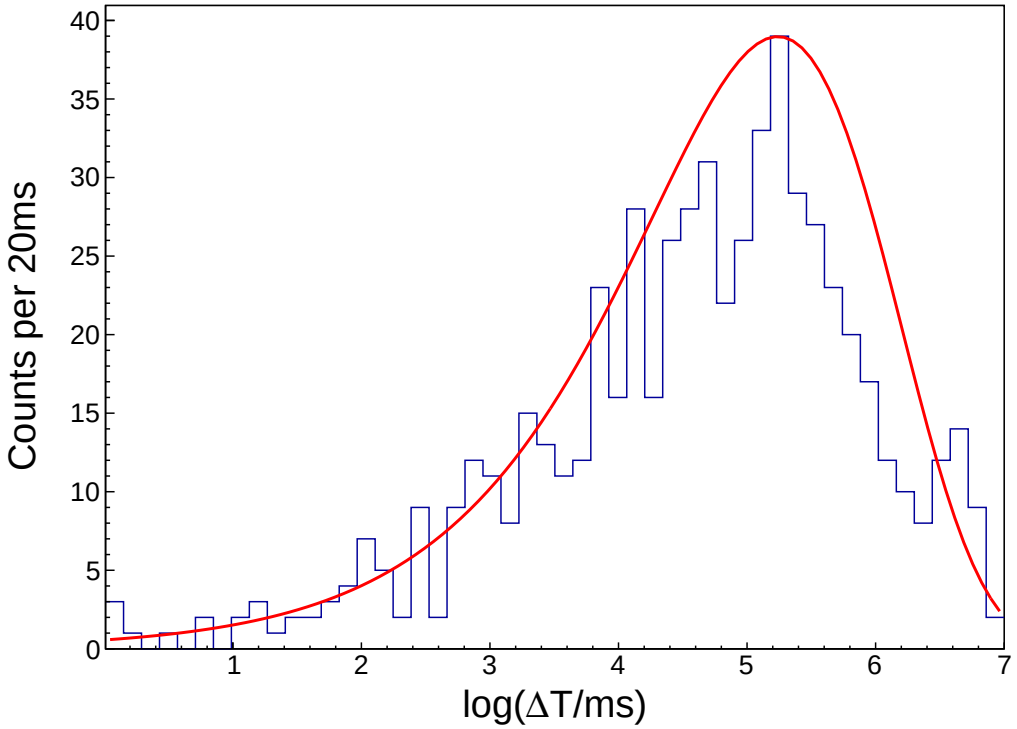

Figure 5.8: Time distribution of βp events correlated with ^{71}Br ions. The daughter nucleus, ^{70}Se, the β-decay half-life is known to be 41.1(3) min [130]. Using the Schmidt method to extract the half-life for ^{71}Kr. The (red) fit yields a $T_{1/2}$=100(3) ms.

The total number of ^{75}Sr ions identified in BigRIPS was 4124, and of these 1885 were implanted into WAS3ABi, yielding an ion detection efficiency of 45.6%. A total of 120 βp decays were correlated with a ^{75}Sr implantation as shown in Fig. 5.9. The spectrum shown corresponds to the y-side energy values of the DSSSD. Events were considered if

they occurred within 300 ms of implantation.

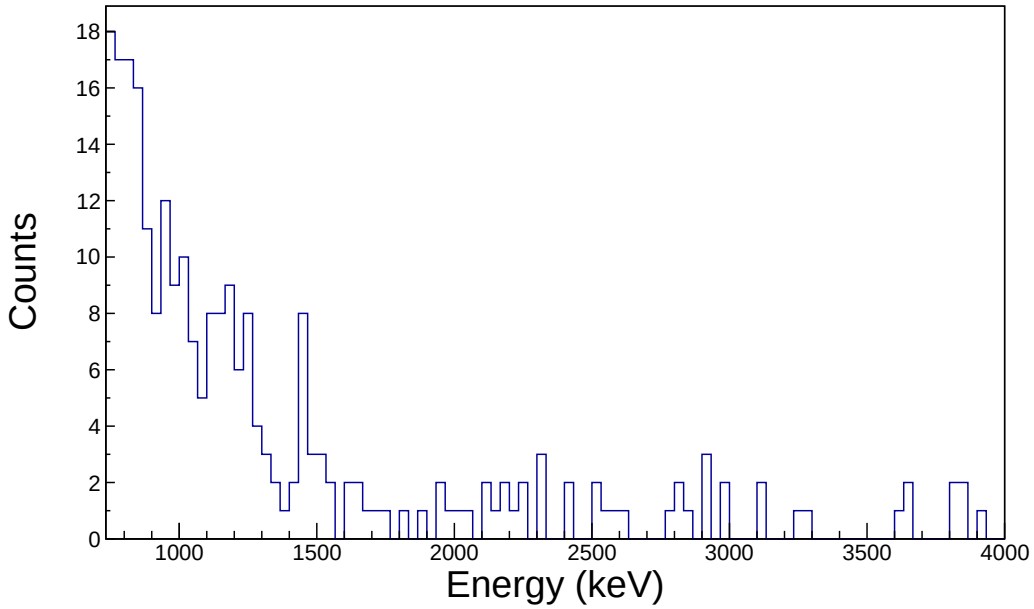

Figure 5.9: β-delayed proton spectrum for ^{75}Sr. From the β-decay of ^{75}Sr and the subsequent proton decay of ^{75}Rb. The spectrum shown corresponds to the y-side energy values of the DSSSD. The position-correlation was a cross-shape. Events were considered if they occurred within 300 ms of implantation.

A half-life of 88(13) ms was extracted from 46 events using the Schmidt method. This value is consistent with the literature value of $T_{1/2}$= 88(3) ms [82]. From the present work, a proton branching ratio of 6.3(6)% was obtained. Previous work by Blank *et al.* [142] at GANIL obtained a branching ratio value of 6.5(33)% from four counts, whilst J. Huikari *et al.* [82] at ISOLDE obtained a value of 5.2(9)% from an average of 5.4 ion/s over 21 hours.

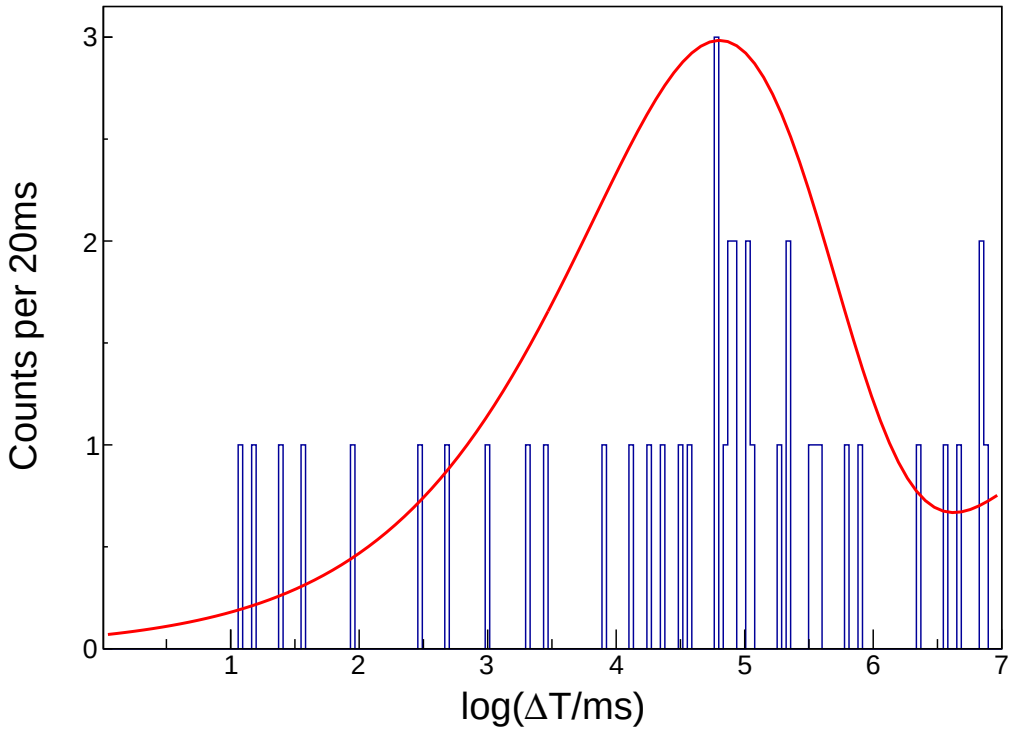

Figure 5.10: Time distribution of βp events correlated with ^{75}Sr ions. The daughter nucleus, ^{74}Rb is 64.761(31) ms [136]. Using the Schmidt method to extract the half-life for ^{75}Sr, the fit yields a $T_{1/2}$=88(13) ms.

The total number of ^{73}Sr ions identified in BigRIPS was 186, and of these a total of 49 events were observed in WAS3ABi, yielding an ion detection efficiency of 26.4%. Fig. 5.11 shows the β-delayed proton spectrum extracted for ^{73}Sr. As a cross-check, the half-life of ^{73}Sr was measured by gating on the proton events, the time distribution is shown in Fig. 5.13. As ^{73}Rb is expected to be proton unbound, a branching ratio is not expected. Candidate transitions for β-delayed protons are observed at 765 keV, 1056 keV, 1440 keV, 2560 keV and 2730 keV.

In Table. 5.3 are the half-lives of the decay times associated with the candidate transitions. The lowest energy-transition at 765 keV had a different time distribution to the other transitions. Therefore, this was disregarded as being the possible ground state candidate. The energy-transition at 1055 keV, 1440 keV, 2560 keV and 2730 keV have consistent half-lives within error and distributions to the half-life of ^{73}Sr obtained in this work. From the data in Fig. 5.11 a half-life, $T_{1/2}=32^{+6}_{-5}$ ms was extracted, using the Schmidt method,

and is consistent with the value of 28^{+5}_{-4} ms obtained from the β-decay half-life measured in this work.

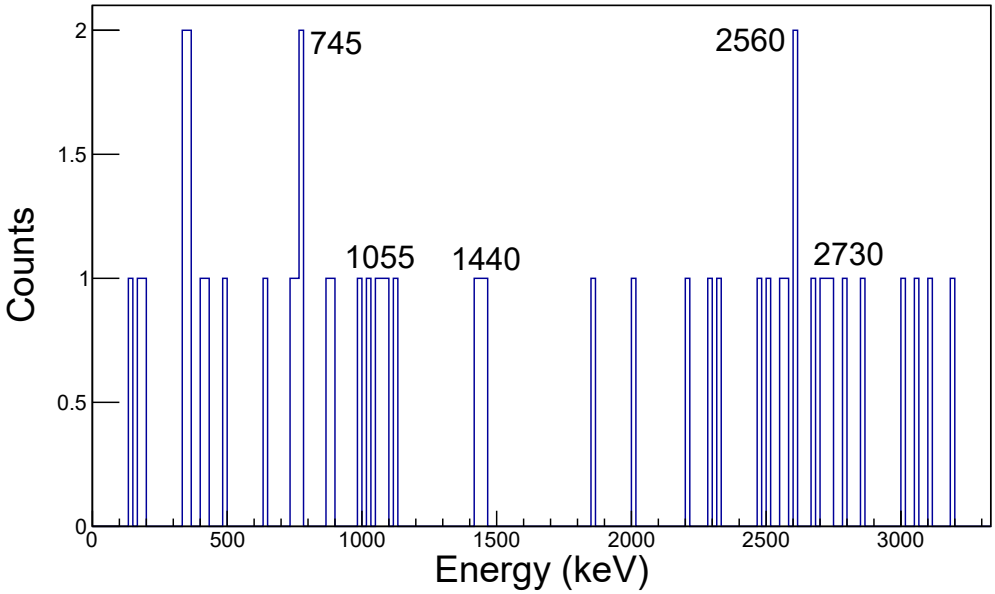

Figure 5.11: β-delayed proton spectrum for ^{73}Sr. From the β-decay of ^{73}Sr and the subsequent proton decay of ^{73}Rb. The spectrum shown corresponds to the y-side energy values of the DSSSD. The position-correlation was a cross-shape. Events were considered if they occurred within 100 ms of implantation.

Shown in Fig. 5.12 is the β-delayed proton spectrum for ^{73}Sr. From the β-decay of ^{73}Sr and the subsequent proton decay of ^{73}Rb. The spectrum shown corresponds to the y-side energy values of the DSSSD. Events were considered if they occurred within 100 ms of implantation. The position correlation considered was a single pixel, i.e. the β-particle and the proton are observed in a single pixel. Candidate transitions for β-delayed protons are observed at 765 keV, 1055 keV, 2560 keV and 2730 keV. The 765 keV transition has a time distribution not consistent with previous results. Therefore, the 1065 keV transition is the most probable candidate. Gating on the spectrum, yields a half-life of 32^{+23}_{-16} ms and is consistent with the β-decay half-life measured in this work.

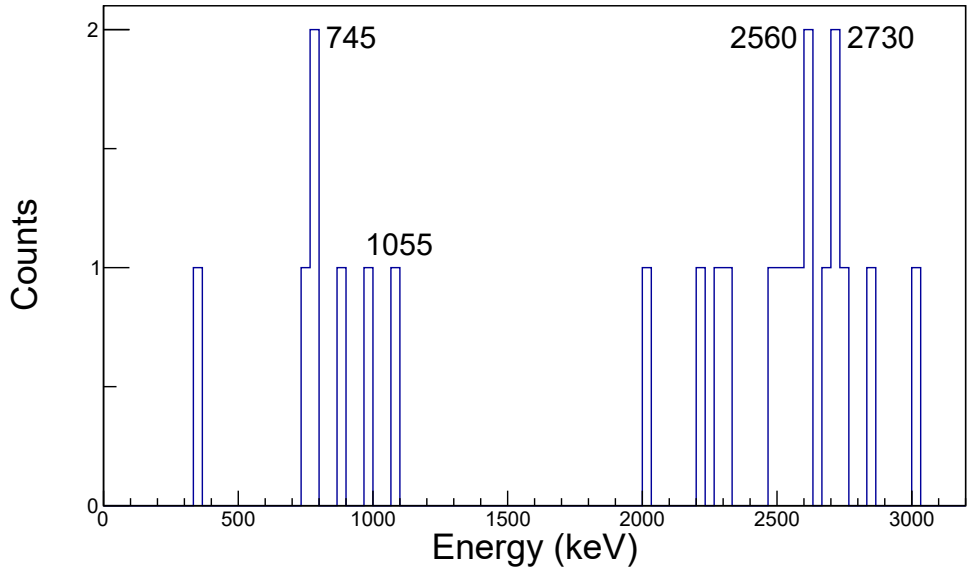

Figure 5.12: β-delayed proton spectrum for ^{73}Sr. From the β-decay of ^{73}Sr and the subsequent proton decay of ^{73}Rb. The spectrum shown corresponds to the y-side energy values of the DSSSD. Events were considered if they occurred within 100 ms of implantation.

Table 5.3: βp-decay half-lives for ^{73}Sr extracted using the Schmidt method.

Transition energy	$T_{1/2}$
765 keV	18^{+17}_{-13} ms
1055 keV	21^{+8}_{-6} ms
1440 keV	19^{+9}_{-7} ms
2560 keV	33^{+11}_{-9} ms
2730 keV	31^{+9}_{-7} ms

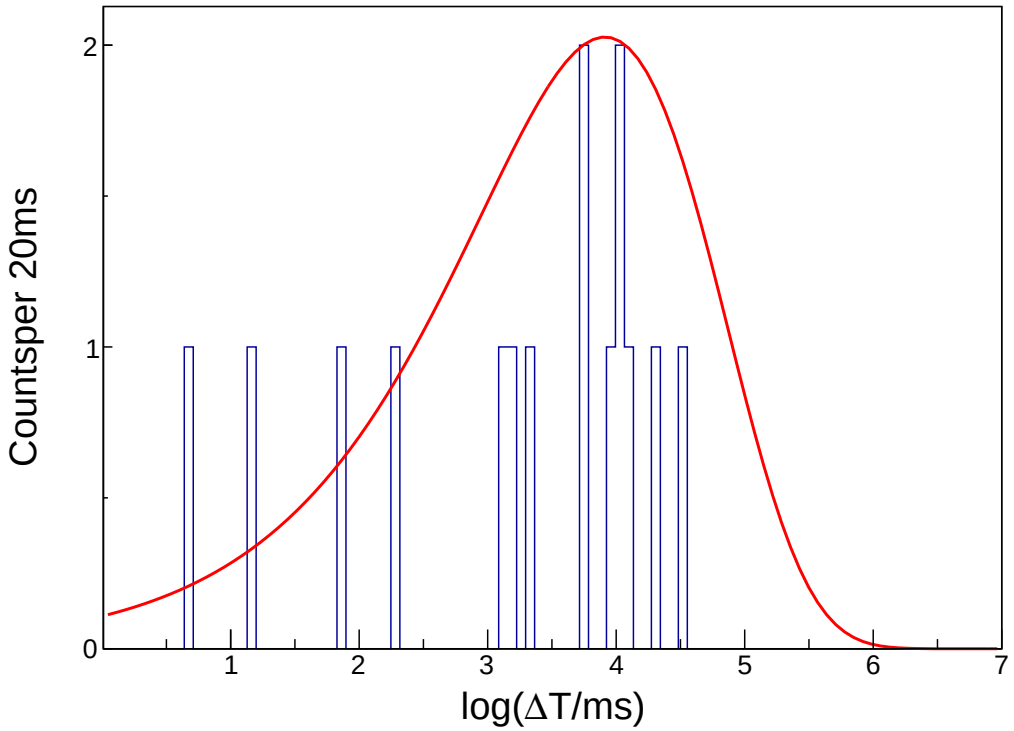

Figure 5.13: Time distribution of βp events correlated with ^{73}Sr ions. The daughter nucleus ^{72}Kr has a $T_{1/2}$= 17.1(2) s [53]. Using the Schmidt method to extract the half-life for ^{73}Sr, the fit yields a $T_{1/2}$=32^{+6}_{-5} ms and is consistent with the β-decay half-life measured in this work.

In 1993, Batchelder *et al.* [81] measured the first β-delayed proton spectrum of ^{73}Sr. However, due to experimental constraints in their work only proton decays above a threshold energy of about 2.5 MeV were observed. A Fermi decay to the IAS in ^{73}Rb at 3750(40) keV was reported. However, this transition was not observed in this work. Henderson [146] at Jyväskylä (JYFL) observed candidates for three new β-delayed proton-decays from ^{73}Rb at 1035 keV, 1187 keV and 1532 keV. The resolution of the DSSSD at Jyväskylä is 4 keV, which is superior to the resolution of WAS3ABi DSSSD. At Japan Atomic Energy Agency (JAEA) [147] a candidate was observed at ∼1 MeV.

From the β-delayed proton spectrum obtained in this work, and comparing to the previous work at JYFL [146] and JAEA [147], the most likely candidate for the proton decaying from ^{73}Sr to the ground state of ^{73}Rb is the energy-transition at 1055 keV. Therefore a S_p of 1055±90 keV for ^{73}Rb was extracted. However, due to βp summing

effects, discussed in the previous section, to extract the final proton-separation energy a GEANT4 simulation [148] was performed. For the S_p=1055±90 keV, the error is based on statistical errors only, the systematic error arising from the simulations and calibration errors, for example, is not included in the above error.

No evidence was found for β-delayed proton decays for ^{74}Sr or ^{76}Y.

5.5.1 β-proton summing effects

To account for β-proton summing effects, GEANT4 [148] simulations were used to extract a tentative proton-separation energy for ^{73}Rb. The GEANT4 simulation was based on the code of N. Warr *et.al* [149]. The detector geometry for the WA3ASBi DSSSD, as described in Section. 3.4.4, was simulated. For the WAS3ABi DSSSD, the detector resolution was σ=28(8) keV. Protons and β-particles were simulated in the experimental conditions. The code provides an initial β spectrum, the β^+ particle had a fixed energy distribution and used Eqn. 2.6 for the expected energy spectrum for β-decay. The code provided spatial distribution of the implantation area [149]. For each event, GEANT4 randomly emits β-particles following and tracks them as are implanted in the DSSSD [149]. The energy of the proton is fixed and run with the β distribution.

The energy for a β-particle and a proton were run simultaneously, which sum together to recreate the experimental β-proton summing effect in the DSSSD [2].

Fig. 5.14 shows the results from the GEANT4 simulation of the β-proton delayed spectrum. The figure shows the β-decay of ^{73}Sr, and the subsequent proton decay of ^{73}Rb [3]. For the β-decay, the expected energy spectrum is shown on the left hand side, the proton in the middle, and the β-proton summing effect on the far right. A proton-separation energy for ^{73}Rb, S_p, of 1055±90 keV was obtained from the β-delayed proton spectrum of ^{73}Sr, is shown in Fig. 5.11. The energy of the proton was determined to be 800 keV, which led to a tentative proton-separation energy of -800±70 keV for ^{73}Rb.

[2] The GEANT4 simulation was performed in a single pixel, while the β-delayed proton spectrum in Fig. 5.11 was constructed using a cross-shaped position correlation. The single pixel βp spectrum is shown in Fig.5.12

[3] The simulation was run with a higher number of events than actually measured.

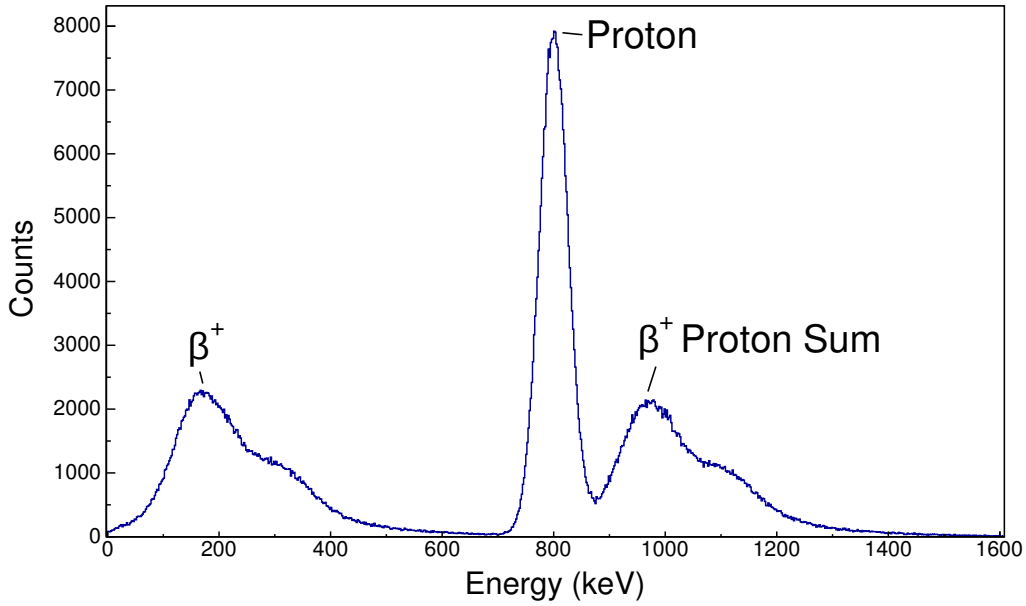

Figure 5.14: A GEANT4 simulation of the energy spectrum from the β-decay of ^{73}Sr and the subsequent proton decay of ^{73}Rb in a silicon detector. The simulation was used to account for summing effects of the β-particle and proton to extract the final proton separation energy. The expected energy spectrum for β-decay is on the left hand side. The energy of the proton (centre) is a parameter input into the simulation. The β-proton summing effect is seen on the far right.

5.6 Isomers and excited states of mass ∼70 nuclei

In this work, a search for evidence of new γ decaying isomers in the nuclei implanted in WAS3ABi was conducted. With the statistics collected, it was not possible to identify any new isomers. However existing isomers could be seen. Isomers in ^{69}Se and ^{73}Kr were analysed and their lifetimes were compared to the results presented in literature.

5.6.1 ^{73}Kr

An energy-time matrix was created for ^{73}Kr is shown in Fig. 5.15. The trigger of the ^{73}Kr opened a gate of 110 μs for the DGF and TDCl modules, allowing the observation of γ-rays in delayed coincidence with the ion following the decay of an isomeric state. A gate is set around the prompt flash (see Section. 4.7.3 for explanation) to remove background radiation and to provide clean spectrum. Isomeric transitions can be identified

as horizontal lines starting in the prompt flash and losing intensity over time. The time walk at low energies was corrected for, as discussed in Section. 4.

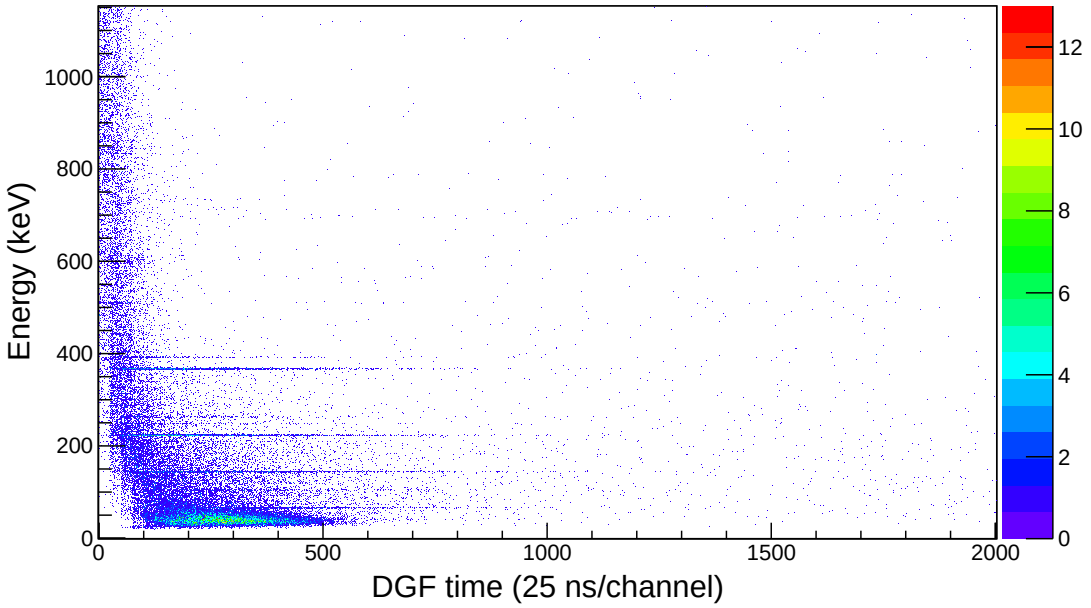

Figure 5.15: Germanium energy time matrix for implanted ^{73}Kr ions. A gate shown is set around the prompt flash to remove background radiation. The transitions arising from isomeric states can be identified in the matrix as the horizontal lines losing intensity over time. Time-walk corrections were applied.

Energy gates were placed on the 40.8- and 65.8-keV γ-rays in ^{73}Kr (see Fig. 5.15) resulting from the decay of the known 433.6-keV $9/2^+$ isomer [150]. This resulted in the Germanium energy spectrum shown in Fig. 5.16. The isomeric state at 433.6 keV decays initially via a 65.8 keV transition. Other previously identified transitions at 144-, 224-, 265- and 368- and 393 keV can also be seen in Fig. 5.16. The inset in Fig. 5.16 shows the mean-lifetime of the isomeric state in ^{73}Kr. This was calculated from a weighted average of the fit to the two transitions and was determined to be 156(31) ns, and is in good agreement with the previously determined value of 155(15) ns [151]. A new transition at 102.7-keV is observed.

Prior work on ^{73}Kr by Satteson *et al.* [152], Freund *et al.* [150] and Chandler *et al.* [151] can be combined to describe the level scheme. In 1990, Satteson *et al.* [152], identified γ-ray transitions in ^{73}Kr for the first time, by tagging the γ-rays of the reaction products of mass 73. Chandler *et al.* [151] found previously unreported transitions at 265- and

393 keV and proposed the level scheme illustrated in Fig. 5.17. The energy transitions at 265- and 393 keV were observed in this work.

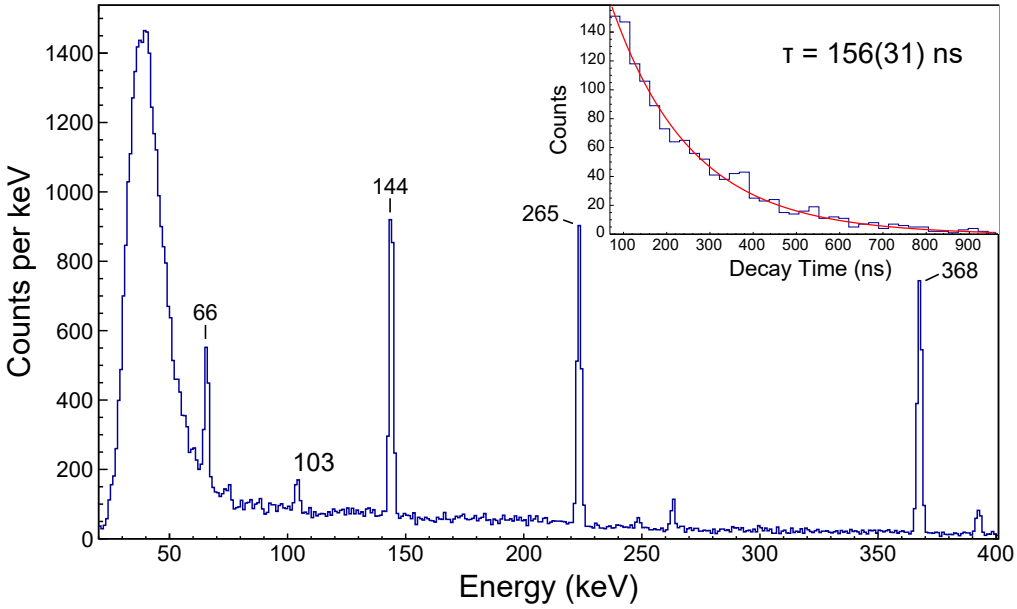

Figure 5.16: The Germanium energy spectrum projected from the energy-time for ^{73}Kr ion. The decay from a $g_{9/2}$ isomer in ^{73}Kr at 433.6-keV. Note a new transition at 102.7-keV is observed. The inset shows the mean-lifetime of the isomeric state in ^{73}Kr was obtained from a weighted average of the fit to the two transitions and was determined to be 156(31) ns.

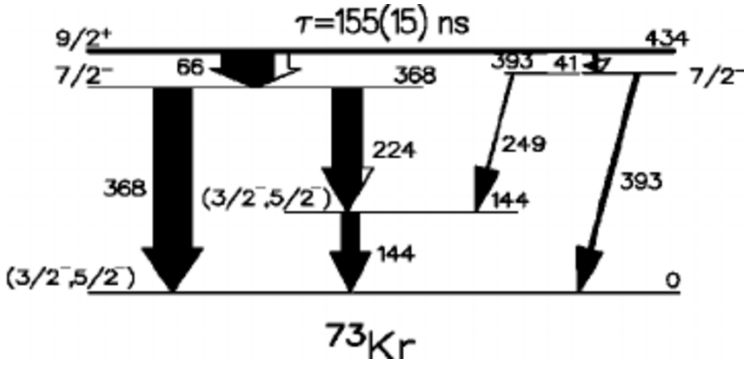

Figure 5.17: The low-lying decay scheme depopulating the $9/2^+$ isomer in ^{73}Kr [150]. Figure reproduced from [151].

5.6.2 ^{69}Se

An energy-time matrix was created for ^{69}Se (shown in Fig. 4.4). Energy gates were placed on the known 39.4- and 534.8-keV γ-rays in ^{69}Se [128], which are observed following the decay of the $5/2^-$ and $9/2^+$ states at 38.85- and 574-keV, respectively.

The mean-lifetime of the 534.8-keV γ-ray in ^{69}Se was obtained by fitting a standard exponential decay curve to the time distribution data. This yields a value of 1389(20) ns as shown in Fig. 5.18. Using the Schmidt method, the lifetime was found to be 1400(20) ns (see Fig. 5.19). Both values are clearly consistent with each other and are also in good agreement with the previously measured value of 1385(33) ns [128].

The mean-lifetime of the state decaying via the 39.4-keV γ-ray in ^{69}Se was measured to be 2.9(1) μs, which is in excellent agreement with the previously published value of 2.89(29) μs [128]. The time walk at low energies was corrected for, as discussed in Section. 4.

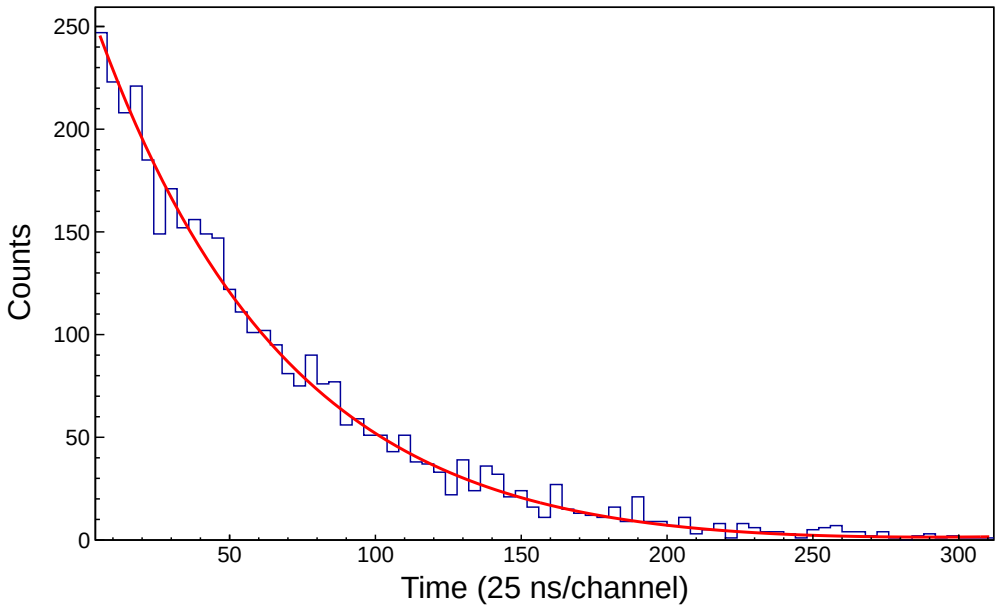

Figure 5.18: Time distribution of the 574-keV transition, gated on the 534.8-keV γ-ray in ^{69}Se. To extract the lifetime the data were fitted using a single exponential decay function (in red), which yields a lifetime, τ=1389(20) ns and is good agreement with literature.

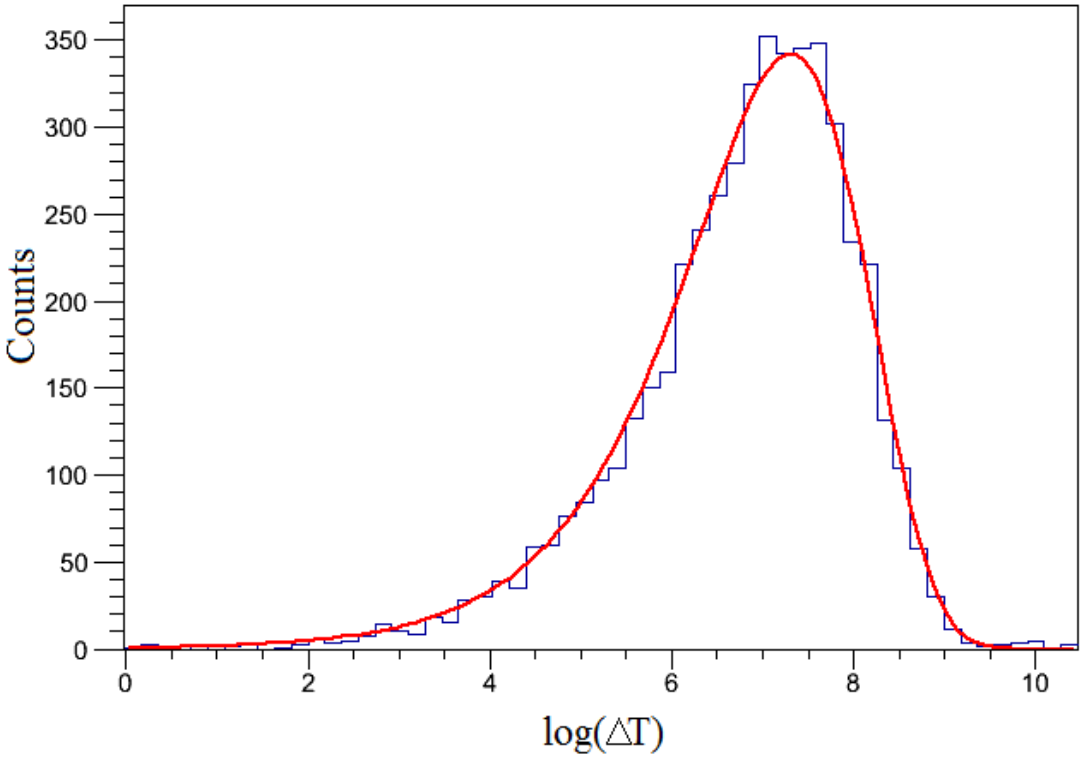

Figure 5.19: Time distribution of the 574-keV transition, gated on the 534.8-keV γ-ray in ^{69}Se. To extract the lifetime the data were fitted using the Schmidt method (the red fit), which yields a lifetime, τ =1400(20) ns and is good agreement with literature, see text for details.

5.6.3 γ-γ-coincidences

To build level schemes, the observation and interpretation of γ-rays in prompt (delayed) coincidence with other γ-rays can be investigated. If γ-rays are emitted in a cascade and none of the involved states has a measurable lifetime, then those transitions can be observed in mutual prompt coincidence. A prompt-matrix was generated for ^{73}Kr to investigate all of the possible combinations of γ-rays (energy E_1 and E_2), which are observed within a time difference window Δt of $\pm$ 300 ns:

$$\Delta t = |t_{(\gamma 1)} - t_{(\gamma 2)}| < 300\ ns \tag{5.1}$$

where t(γ_1) and t(γ_2) are the measured times for the emission of the two γ-rays γ_1 and γ_2, respectively. A gate can then be set on an observed transition in E_1 and the gated prompt γ-γ-matrix is projected on the E_2-axis.

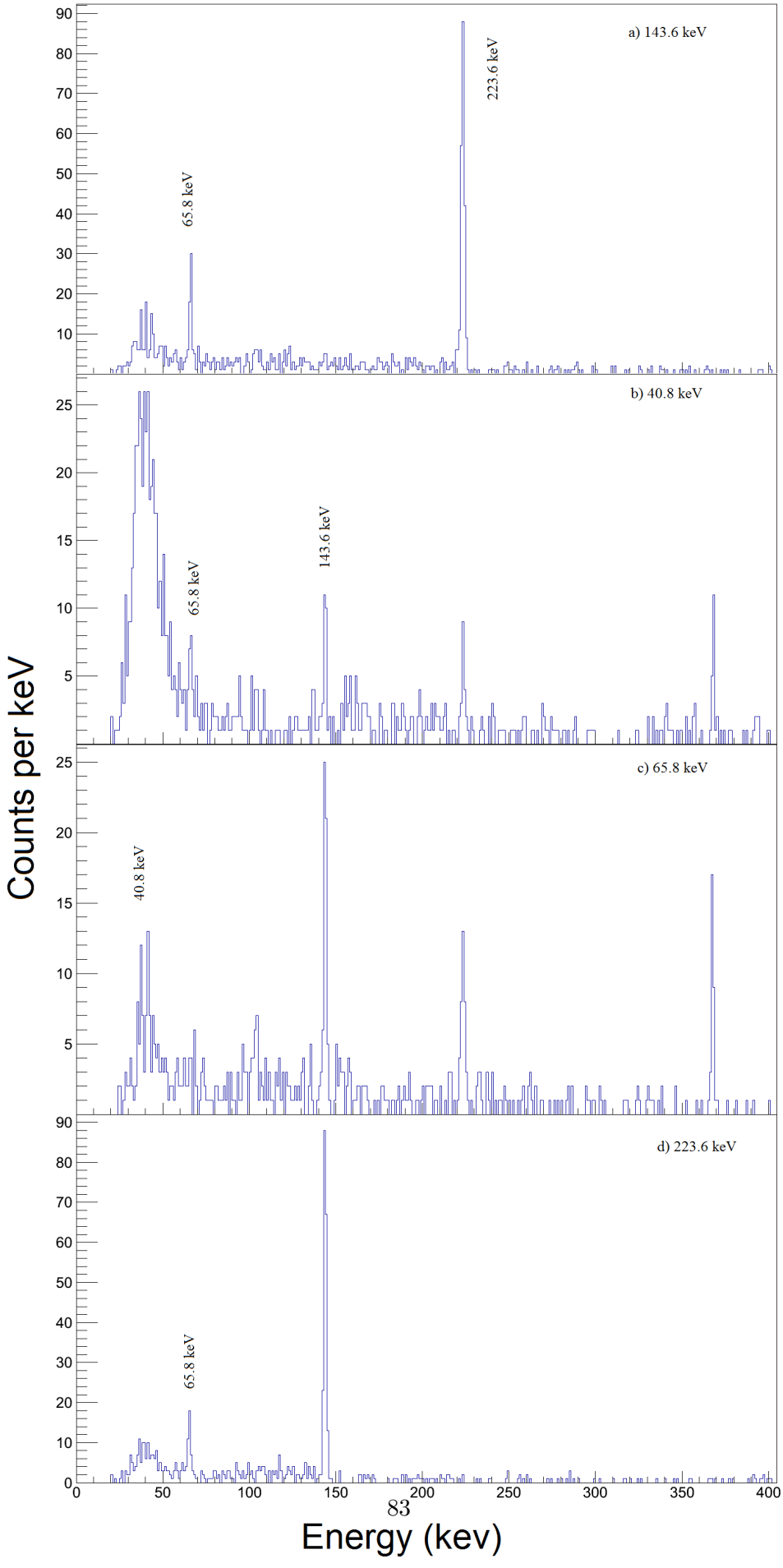

Figure 5.20: Germanium (DGF) spectrum for ^{73}Kr observed in prompt coincidence.

Relevant γ-γ-coincidence spectra are shown in Fig. 5.20 where gates are set on the a) 143.6-keV, b) 40.8-keV, c) 65.8-keV, d) 223.6-keV transitions observed in coincidence with β-decay of ^{73}Kr. Spectra a)-d) show the prompt γ-spectra with the requirement mentioned in formula 5.1.

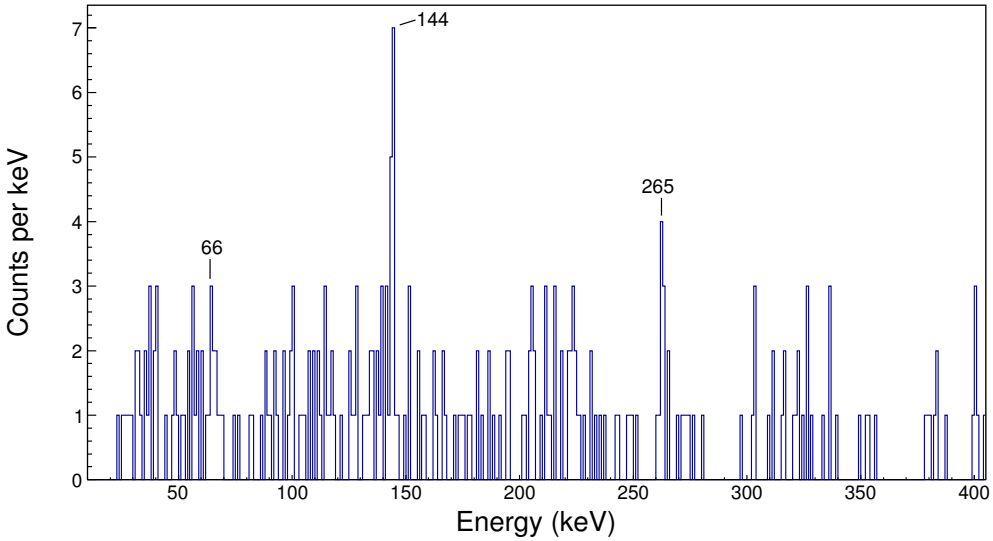

Figure 5.21: Germanium (DGF) spectrum for ^{73}Kr observed in prompt coincidence with the 102.7-keV transition.

In Fig. 5.21 the 102.7-keV transition is shown in coincidence with the 65.8-, 143.6-, and 265- keV transitions.

5.7 β-gated γ-ray spectrum

β-Ge-energy-time matrices were created for analysis to search for γ decays following the β-decay of the nuclei produced in this work. The γ-ray energy on the y axis, and the DGF timing information on the x axis. The DGF timing is taken relative to the decay trigger signal. After each decay trigger, a 110 μs gate is opened for the Ge detectors to measure prompt- and delayed γ-rays following the β-decay, revealing information about the level structure of the daughter nucleus. The energy-time matrix which identifies prompt and delayed- coincidence γ-rays with the β-decays of the implanted ^{71}Kr ions is shown in Fig. 5.22.

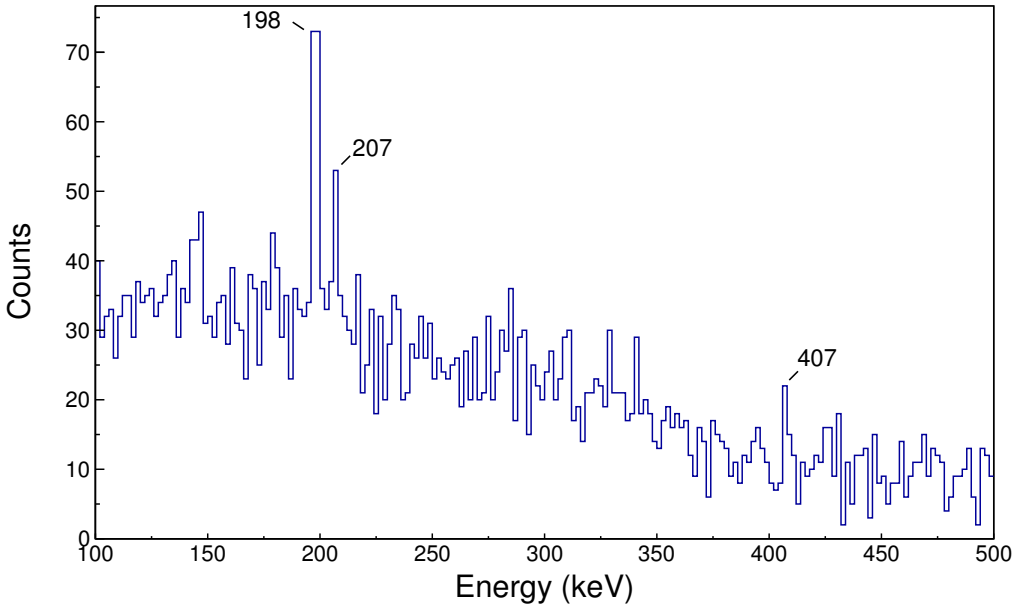

Figure 5.22: A projection of delayed γ-rays in ^{71}Br following the implantation and the decay of a ^{71}Kr ion. Transitions are seen at 198, 207 and 407 keV.

The three lines of interest for ^{71}Kr are seen at 198, 207 and 407 keV in Fig. 5.22. Their relative intensity is in agreement with those observed in an in-beam study on ^{71}Br by Arrison *et al.* [134] and Fischer *et al.* [153]. They are associated with the β-decay of ^{71}Kr, and de-excite the 207 keV level in ^{71}Br.

A goal of the experiment was to try to observe new γ decays following the β-decay of the most exotic nuclei produced, however a lack of statistics prevented the observation of such transitions.

5.8 Discussion and conclusions

The β-decay half-lives of known nuclei were also observed and measured to provide a validation of the experimental and analysis methods. The half-lives of nuclei ^{73}Sr and ^{76}Y have been measured for the first time in this work, and a half-life of ^{74}Sr has been measured with higher precision than previous work. The half-life of ^{74}Sr is needed to gain a complete picture of the two-proton-capture branch for the ^{72}Kr waiting point.

The mirror nucleus of ^{73}Sr, ^{73}Kr, has transitions at 779.2 keV, 1154.2 keV and 1528 keV [152] which are similar in energy to 765 keV, 1055 keV, 1440 keV transitions measured in

^{73}Sr in this work. This may indicate that states measured in the β-delayed proton spectrum are being populated. The measurement obtained in this work of S_p= -0.80±0.70 MeV is a direct measurement, if the proton decay originates from the ground state of ^{73}Rb. Jenkins [154] argued that there may be isomeric "shadowing" of the ground-state, where the $9/2^+$ state is populated, rather than the ground state. The isomeric state then promptly proton decays, and this could account for the nature of ^{73}Rb. Henderson [146] obtained a tentative direct measurement of S_p ∼-1.04 MeV, however this work did not account for β-proton summing effects. An upper limit of 30 ns for the half-life of ^{73}Rb was obtained by Pfaff *et al.* [52], which indicated that ^{73}Rb is proton-unbound by at least 680 keV, the work assumed that the emitted proton comes from the $f_{5/2}$ state as the mirror nucleus is ^{73}Kr. However, work by Kelsall *et al.* [155] revised the decay scheme of ^{73}Kr, assigned the ground state to be the $3/2^-$ state based on γ-ray spectroscopy. Proton-separation energies, S_p of -0.59(55) MeV (Audi-Wapstra extrapolation (AWE) model) and -0.55(32) MeV (Skyrme-Hartree-Fock model) were calculated by Brown *et al.* [85]. A proton-separation energy, S_p of -0.71(10) MeV was calculated by Rodríguez *et al.* [59], this work used Coulomb shifts along with precise mass measurements of the ^{73}Rb mirror nucleus, ^{73}Kr. Kaneko *et al.* [87] calculated single-proton-separation energies of -0.9 MeV and -1.1 MeV from shell-model calculations with the GXPF1A and JUN45 shell-model effective interactions, respectively. The value obtained in this work, is within the range of the calculated and previously measured value. Proton emission calculations for ^{73}Rb will be discussed in Chapter 6.

The measurements of the half-life of ^{74}Sr and the proton-separation energy of ^{73}Rb will be used in reaction network calculations for the astrophysical *rp*-process in Chapter. 7.

Chapter 6

Beyond the drip-line

Many of the nuclei of interest produced in this work are exotic, lying at, or very close to the proton drip-line, and beyond. In this chapter, the experimental and theoretical results from RIBF97 are presented. A particle identification plot yielding new information about the proton drip-line is discussed. The data analysis technique for obtaining the estimate and upper limit of the half-lives of unbound nuclei ^{72}Rb and ^{73}Rb, respectively,q is discussed. The results and discussion for the proton emission calculations for ^{72,73}Rb will be presented. This discussion will be presented in the context of the theory and motivation as outlined in Chapters 1 and 2.

6.1 Mapping the drip-line

As one moves away from the valley of stability towards increasingly neutron-deficient nuclei, the borders between bound and unbound systems for the proton drip-line are determined by the change in sign of the proton-separation energies, S_p. Fig. 6.1 shows the particle identification plot for RIBF97 with both settings (^{73,74}Sr). One goal of the experiment was to probe the proton drip-line for the elements of Y and Zr by searching for ^{75}Y and ^{77}Zr and studying the decay mode of ^{76}Y.

Previous work by Kienle *et al.* [131] measured the half-life of the T_z =- 1/2, odd-Z nucleus, ^{77}Y. The half-life was measured to be 57^{+22}_{-12} ms. From the detection of β^+ and γ events in a fragmentation experiment, Faestermann [132] concluded that β^+-decay is dominant, while the proton emission branch is expected to be small. Kienle also measured a total of two events and assigned these to ^{76}Y. The work of Kienle *et al.* [131] established the stability of ^{76}Y against proton emission. In 2003, Moller and Nix [145] predicted

$T_{1/2}$=37.8 ms for the β-decay of ^{76}Y and calculated the separation energy S_p= -0.57 MeV, suggesting that this is a proton unbound nucleus. Kaneko *et al.* [87] calculated separation energies for ^{76}Y of S_p= -0.61 MeV and S_{2p}= 0.64 MeV. From the present work a half-life of $T_{1/2}= 24^{+12}_{-6}$ ms has been measured, indicating that β^+-decay is the dominant mode of decay.

One count of ^{77}Zr was found in the present work and following rigorous checks of the event, confirmed [114]. No counts of ^{75}Y were observed, however. The isotope ^{72}Rb was unexpectedly observed in BigRIPS with 14 counts, the gap in the PID spectrum in Fig. 6.1 between ^{74}Sr and ^{72}Kr indicates the absence of the proton unbound ^{73}Rb in the secondary beam. Previous work had already suggested that the isotope ^{73}Rb is proton unbound [52]. Jenkins [154] discussed the proton unbound nature of ^{73}Rb, and suggesting it may have important implications in the way ^{72}Kr acts as a waiting point in the *rp*-process.

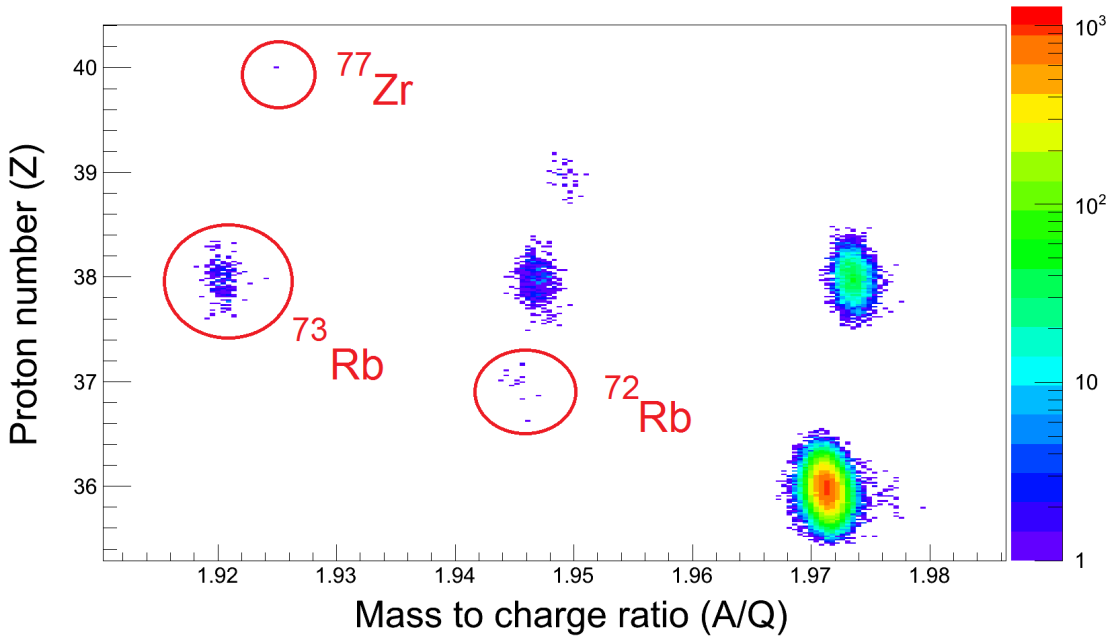

Figure 6.1: A particle identification plot from the RIBF97 experiment, showing the sum of data from both of the settings used for ^{73,74}Sr. The PID plot shows the deduced nuclear charge of the F11 ionisation chamber versus the mass-to-charge ratio (A/Q) measured in BigRIPS using the F3-F5 ToF measurement. One can note the absence of ^{73}Rb, while there are 14 counts for ^{72}Rb, however.

The region of the nuclear landscape involved in this experiment is shown in Fig. 6.2 and shows the potential new evidence for the drip-line location, based on the experimental

results obtained in this work.

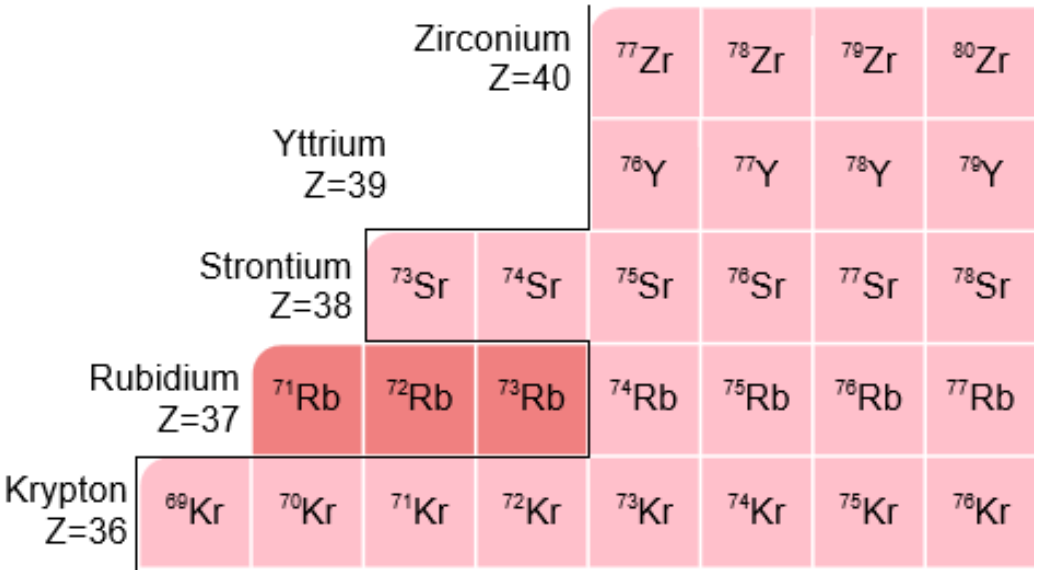

Figure 6.2: Mapping the proton drip-line from the results obtained in this work. The black line indicates the proton drip-line. Colours indicate the decay modes of the nuclei; light pink represents nuclei that predominantly undergo β-decay, dark-pink are nuclei that proton decay. Figure adapted from [60].

6.2 Upper limits and estimates of half-lives of unbound nuclei

Following the procedure outlined by Suzuki *et al.* [156] the estimated half-life and the upper limit of the half-life have been calculated for ^{72}Rb and ^{73}Rb, respectively. To determine the half-lives of ^{72}Rb and ^{73}Rb, the observed yields of the neighbouring isotopes were compared with the expected yields, which were extracted from interpolation of the yields of neighbouring isotopes. The observed and expected yields were then used to determine the activity of the isotope, and when the activity is combined with the ToF values in BigRIPS, between F0 and F7, the half-life for each isotope can be extracted.

Fig. 6.3 shows a plot used to determine the expected yield for ^{72}Rb following the procedure outlined above. The ToF from the production target located at F1, to implantation at F11 (ToF1-11) was found to be 769 ns from LISE^{++} calculations [105], the error is negligible [114]. By considering the yields expected relative to the neighbouring isotones, ^{73}Sr and ^{71}Kr, the expected yield of ^{72}Rb is 13753$\pm$47, however, only 14 events were observed

at F11. The errors of the expected yield are from the observed yields of the neighbouring isotones, ^{73}Sr and ^{71}Kr. From the expected yield compared to the observed yield, the activity and ToF were compared and the estimated half-life of the new isotope ^{72}Rb was determined to be $T_{1/2} = 77(21)$ ns.

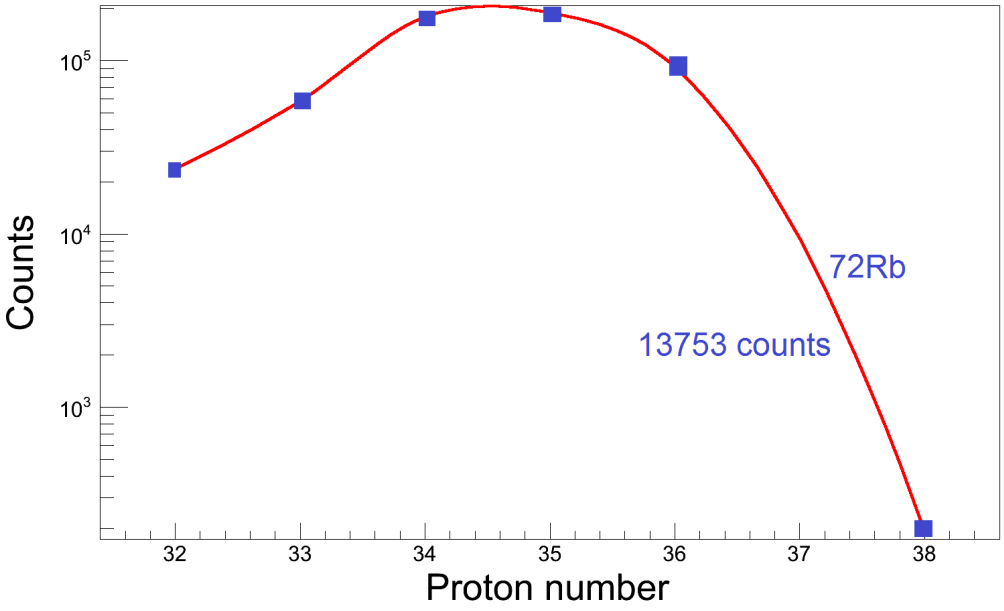

Figure 6.3: A graph of the number of events of the N=35 isotone identified in BigRIPS versus the proton number, Z. To determine the estimated half-life of ^{72}Rb the expected number of counts are compared to the actual counts of the neighbouring isotones ^{73}Sr and ^{71}Kr. The estimated $T_{1/2} = 77(21)$ ns.

From the experimental non-observation of ^{73}Rb the upper limit of the half-life can be determined by assuming that a single count has been observed. Fig. 6.4 shows a graph used to determine the expected yield for ^{73}Rb. The ToF1-11 from the production target to implantation was found to be 793.8 ns from LISE^{++} calculations. By considering the yields expected relative to the neighbouring isotones, ^{74}Sr and ^{72}Kr, the expected yield of ^{73}Rb is 832±26 nuclei, however, no events are observed at F11, therefore an observation limit of 1 is assumed. This places an upper limit for the $T_{1/2}$ at 70 ns.

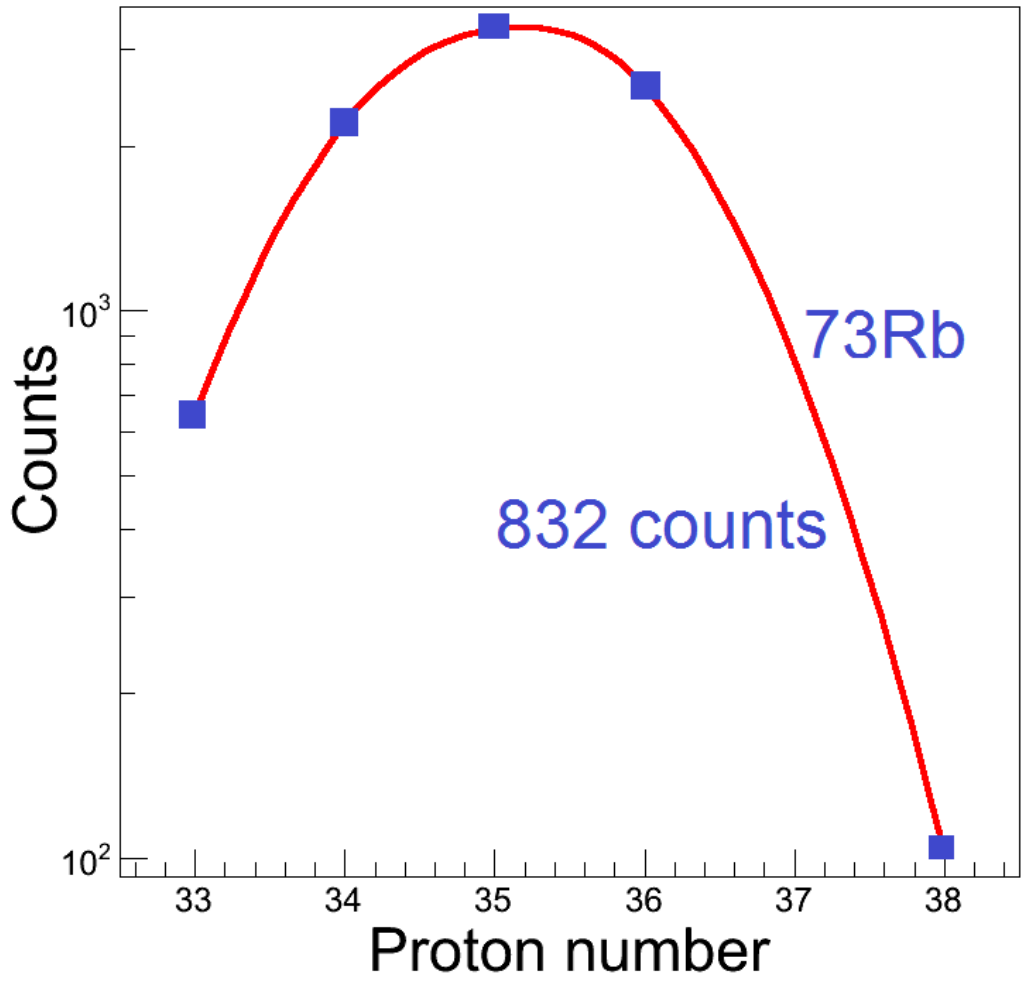

Figure 6.4: A graph of the number of events of the N=36 isotone identified in BigRIPS versus the proton number, Z. To determine an upper limit of the half-life of ^{73}Rb the expected number of counts are compared to the actual counts of the neighbouring isotones ^{74}Sr and ^{72}Kr. The upper limit of the $T_{1/2}$ = 70 ns.

6.3 Proton emission calculations

At the proton drip-line the valence proton is not bound by the nuclear potential. The Coulomb potential barrier confines the protons and inhibits particle emission. However, when the penetration probability is high enough, proton emission can compete with β-decay. Studies of the angular momentum, decay energy and half-life of proton emitters have been shown to provide information on the wave-functions of the parent state through

the WKB approximation for spherical nuclei. For deformed nuclei to determine the wave-function, one has to instead solve the full coupled channel problem for resonances, since the proton is a resonance. In Chapter. 2.5 the proton emission calculations performed by L.S. Ferreria and E. Maglione to characterise the decay of ^{72,73}Rb were outlined.

6.4 Proton emission calculations for ^{73}Rb

The odd-even nucleus ^{73}Rb was estimated to have a half-life upper limit of 70 ns in this work. The proton emission calculations for ^{73}Rb, used a non-adiabatic quasi-particle model [74], which considered a Nilsson proton quasi-particle coupled to the experimentally known excited states of the even-even core ^{72}Kr. The calculations performed for a specific proton energy provided the half-life of the proton emitting states as a function of nuclear deformation.

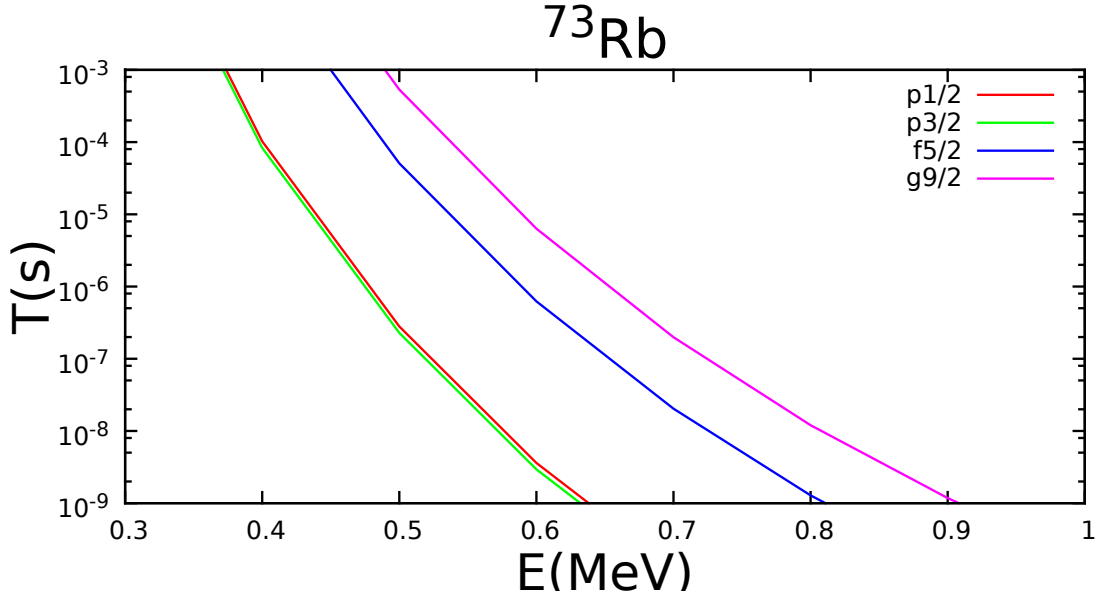

Figure 6.5: Theoretical proton emission half-lives for different orbitals around the Fermi surface as a function of proton decay energy for ^{73}Rb. The calculation is for a spherical nucleus, to obtain an estimate of possible half-lives for the different decaying states. The experimental upper limit of the half-life from this work was determined to be 70 ns, which corresponds to a minimum energy of 550 keV.

The mirror nucleus of ^{73}Rb is ^{73}Kr [155], the ground state of which is $3/2^-$, this may

give an insight into the ground state spin. The spectrum shown in Fig. 6.5 is the theoretical proton emission half-lives from ^{73}Rb, corresponding to the different angular momenta of the emitted proton as a function of energy. The calculation is for a spherical nucleus, to obtain an estimate of possible energies for the different decaying states. From the upper limit of the half-life obtained in this work, ∼70 ns, this corresponds to a minimum energy of 550 keV. This could be satisfied for a proton in a $1/2^-$ or $3/2^-$ state with a proton energy higher than 550 keV. This is assuming there is no change in the sign of the deformation between parent and daughter states involved in the decay. This is in good agreement with the AME2012 prediction of -570(100) keV [157].

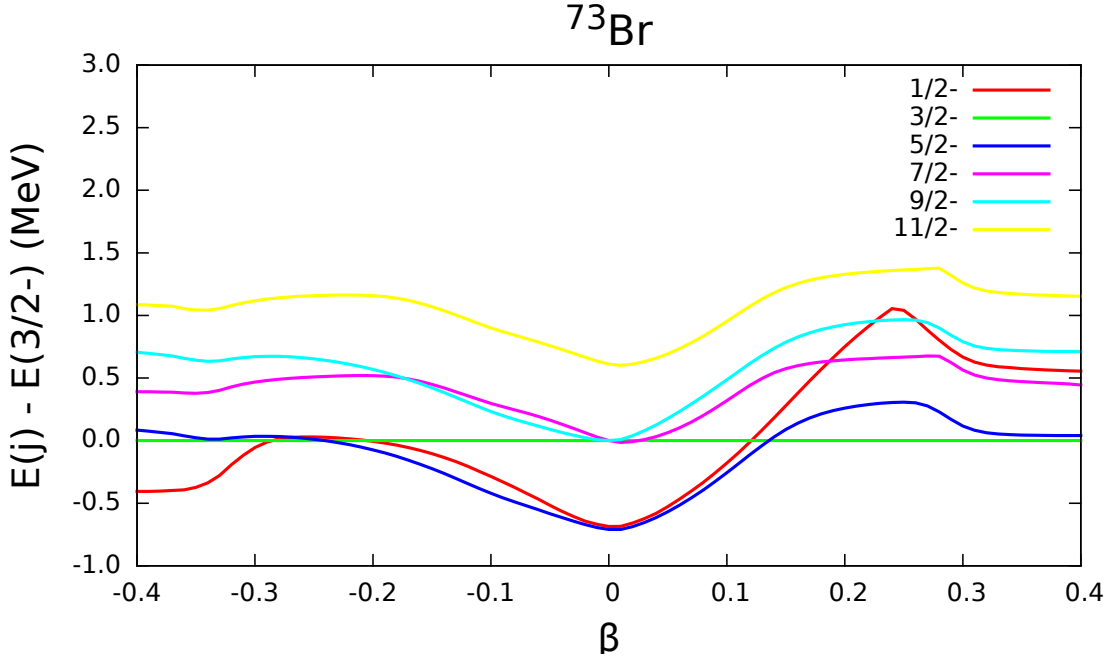

Figure 6.6: Theoretical energies (MeV) of the negative parity states with respect to the energy of the $3/2^-$ state (experimental ground state of the mirror nucleus ^{73}Kr) as a function of deformation, using the non-adiabatic quasi-particle wave-functions for ^{73}Rb.

The calculated energies of the negative parity states with respect to the energy of the $3/2^-$ state in ^{73}Rb, (*cf:* this is the experimental ground state of the mirror nucleus ^{73}Kr) are shown in Fig. 6.6. For large (ß=0.3 - 0.4) positive deformation, the spectrum seems to be in reasonable agreement with the latest experimental level scheme for ^{73}Kr [155].

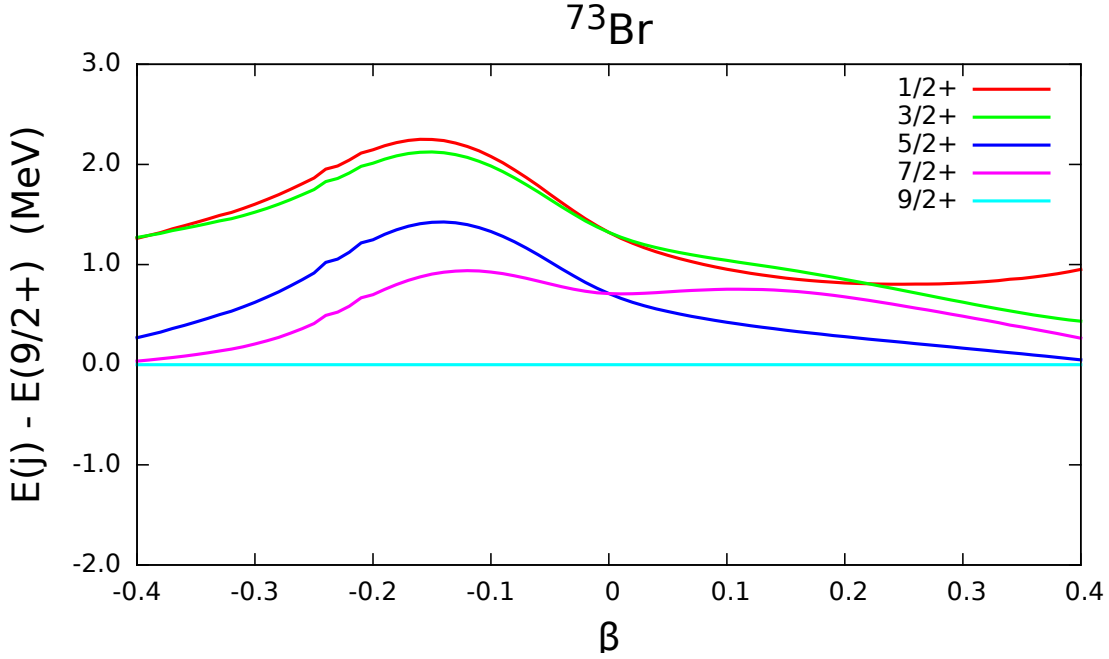

Figure 6.7: Theoretical energies (MeV) of the positive parity states with respect to the energy of the $9/2^+$ state, as a function of deformation, using the non-adiabatic quasi-particle wave-functions for ^{73}Rb.

The energies of the positive parity states with respect to the energy of the $9/2^+$ state are shown in Fig. 6.7. The $9/2^+$ state seems to be consistently the lowest positive parity state (for deformation, ß up to 0.4), while in ^{73}Kr (mirror nucleus) the lowest positive parity state is the $5/2^+$. One possible explanation of this discrepancy is that at zero deformation, the energy of the $5/2^+$ state is equal to that of the 2^+ state in the core nucleus, ^{72}Kr, (since within the model calculations results from the coupling of the $g_{9/2}$ orbital with the first 2^+ state in the core). Increasing the deformation reduces the energy of the $5/2^+$ state, which almost crosses the $9/2^+$ state at ß = 0.4. If the energy of the 2^+ state was lower, then the $5/2^+$ state could cross the $9/2^+$ state at a lower deformation (similar to the crossing that reproduces the negative parity states). The 0^+ state is lowered in energy with respect to the 2^+ state, because of configuration mixing. If the odd proton reduces the configuration mixing of the core, then the energy of the 2^+ state would decrease, and the $5/2^+$ state could become the lowest positive parity state for a lower deformation.

Fig. 6.8 shows the theoretical proton emission half-lives, within the non-adiabatic quasi-particle approach, for the fixed positive deformation ß=0.37, suggested by Moller and Nix [145], as a function of the energy of the escaping proton, and for different decaying

states. This corresponds to a minimum energy of 600 keV for the escaping proton.

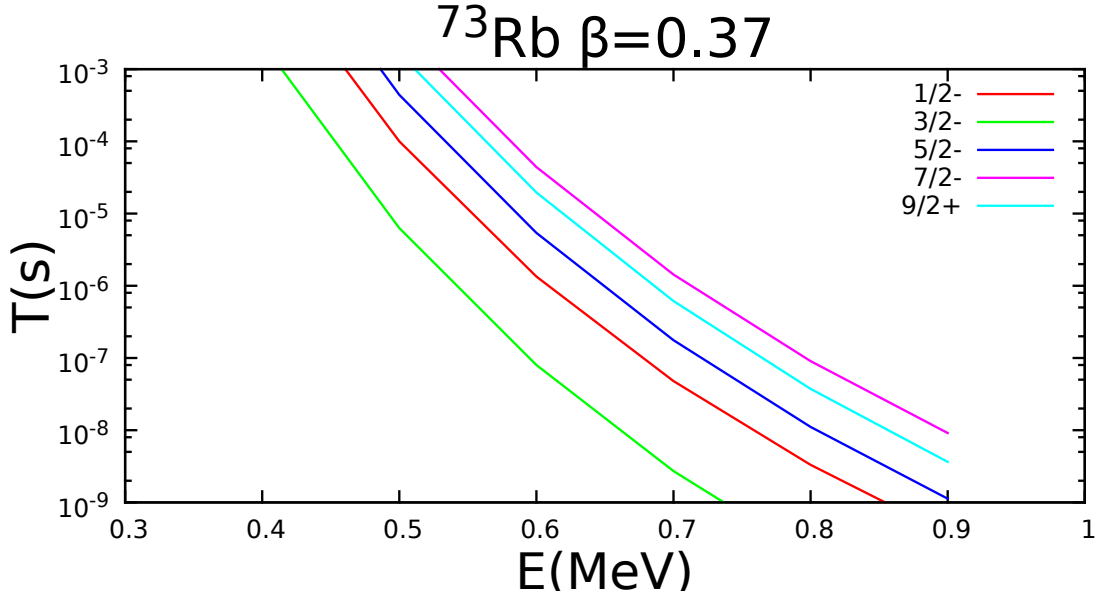

Figure 6.8: Theoretical proton emission half-lives for a fixed positive deformation of ß=0.37, as a function of the energy of the escaping proton and for different decaying states, using the non-adiabatic quasi-particle wave-functions for ^{73}Rb. The experimental upper-limit of the half-life from this work was determined to be 70 ns, which corresponds to a minimum energy of 600 keV.

Fig. 6.9 shows the theoretical proton emission half-lives for a fixed negative deformation of ß= -0.37, as a function of the energy of the escaping proton, and for different decaying states based on the results shown in Fig. 6.6. This corresponds to a minimum energy of 600 keV for the escaping proton.

From these calculations, it is clear that the experimental upper limit for the half-life of ^{73}Rb yields a lower limit of ∼600 keV for the $1/2^-$ state, or $3/2^-$ state, at negative deformation. At positive deformation, it seems that the $3/2^-$ state is the most likely. The calculations were also performed with another parametrisation of the interactions, but there was no change in the results. The energy should be at least 600 keV, experimentally.

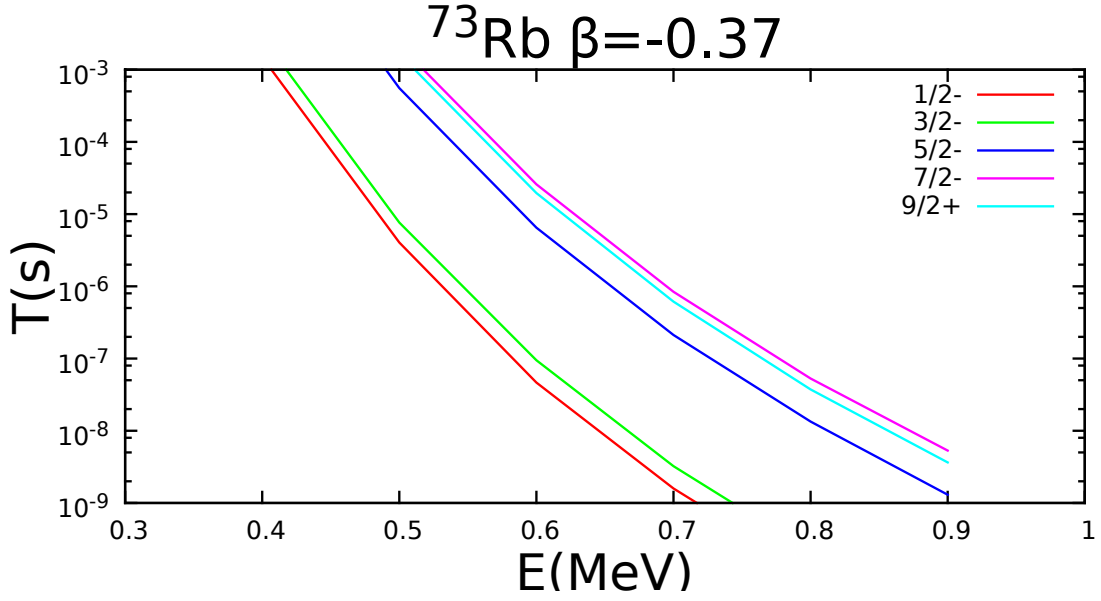

Figure 6.9: Theoretical proton emission half-lives for a fixed negative deformation of ß=-0.37 as a function of the energy of the escaping proton and for different decaying states, using the non-adiabatic quasi-particle wave-functions for ^{73}Rb. The experimental upper-limit of the half-life from this work was determined to be 70 ns, which corresponds to a minimum energy of 600 keV.

6.5 Proton emission calculations for ^{72}Rb

The estimated half-life for the odd-odd nucleus ^{72}Rb was found to be 77(21) ns in this work. ^{72}Rb was expected to be beyond the proton drip-line in recent calculations. Previously, Moller and Nix [145] calculated for ^{72}Rb that S_p = -0.800- keV and Kaneko *et al.* [87] calculated ^{72}Rb S_p = -0.81 keV and S_p = -1.73 keV for the GXPF1A and Jun45 interactions, respectively.

As ^{72}Rb is an odd-odd nucleus, the neutron is not a spectator and contributes actively to the decay [73]. Therefore to understand the proton emission for ^{72}Rb, the neutron levels in the daughter nucleus ^{71}Kr were investigated. The aim was to understand which state may give rise to the proton emission in ^{72}Rb.

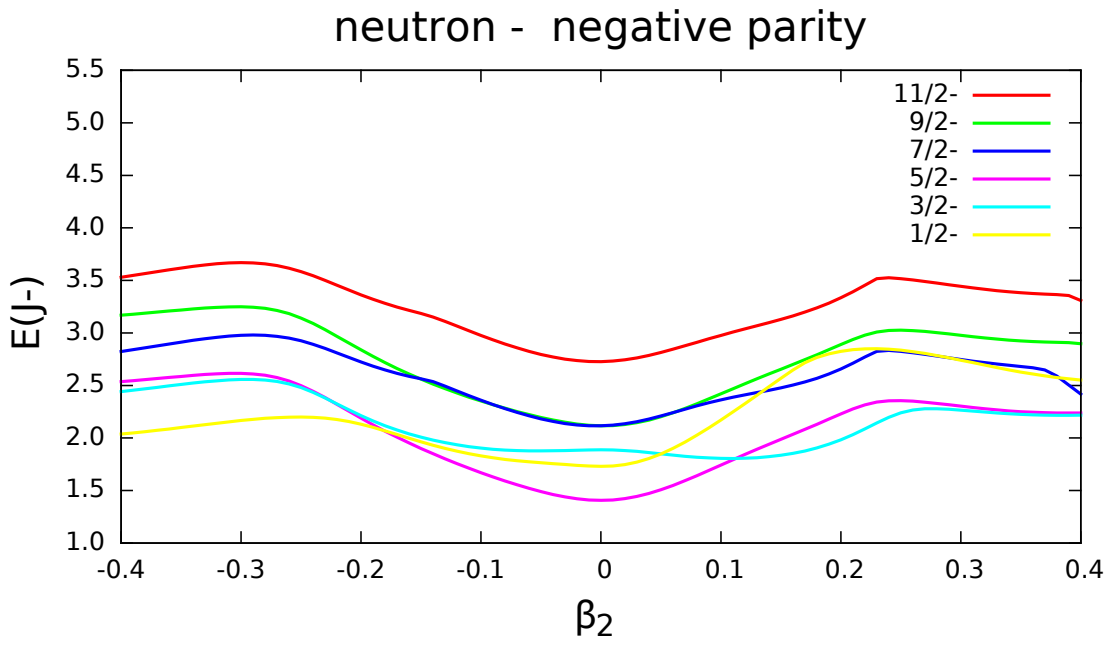

Figure 6.10: The neutron levels with negative parity states in the daughter nucleus ^{71}Kr as a function of deformation from -0.4 (oblate) to +0.4 (prolate). For large negative deformations, the lowest energy is state predicted to be $1/2^-$. For large positive deformations, the lowest state is predicted be $5/2^-$ or $3/2^-$.

Fig. 6.10 shows the negative parity states in the daughter nucleus, ^{71}Kr, determined from non-adiadatic quasi-particle calculations. For large negative deformations, the lowest state is predicted to be $1/2^-$. For large positive deformations, the lowest state predicted to be $5/2^-$ state or $3/2^-$ state. For no deformation (i.e. ß = 0) the lowest state is predicted to be $5/2^-$ state.

Similar calculations for the positive parity states in the daughter nucleus ^{71}Kr, are shown in Fig. 6.11. The lowest state is predicted to have a spin of $9/2^+$. For large positive deformation the ground state is predicted be the $9/2^+$ state, but this depends on the strength of the spin-orbit interaction. For the absolute energies of the negative and positive parity states, the change in spin-orbit interaction could modify the results. A lower strength would push up the $9/2^+$ state, and the ground state would become the $5/2^-$ state. For negative deformation, the lowest state is predicted to be the $9/2^+$ state or the $1/2^-$ state, that are almost at the same energy. Presently, the situation regarding the spin and parity of the experimental ground state of ^{71}Kr is unclear. Fischer *et al.* [153] have investigated the ^{71}Br decay scheme in detail. The experimental evidence is consistent

with ^{71}Kr having a $J^{\pi}=5/2^{-}$ for the ground state, and is consistent with the expectation for the mirror partner of ^{71}Br. If there exists a $5/2^{-}$ state close in energy to the $1/2^{-}$ state, then the proton would decay to the $5/2^{-}$ state. Fischer *et al.* [153] suggest evidence for two β-decaying states in ^{71}Kr. The unusually strong β-decay to excited states between this mirror pair seems to arise from the strong mixing of shapes and implies that the wave-functions of the ^{71}Kr and ^{71}Br ground states must be different from each other. It seems that the ground state should be the $5/2^{-}$ state, but there remains a possibility that it is the $1/2^{-}$ state.

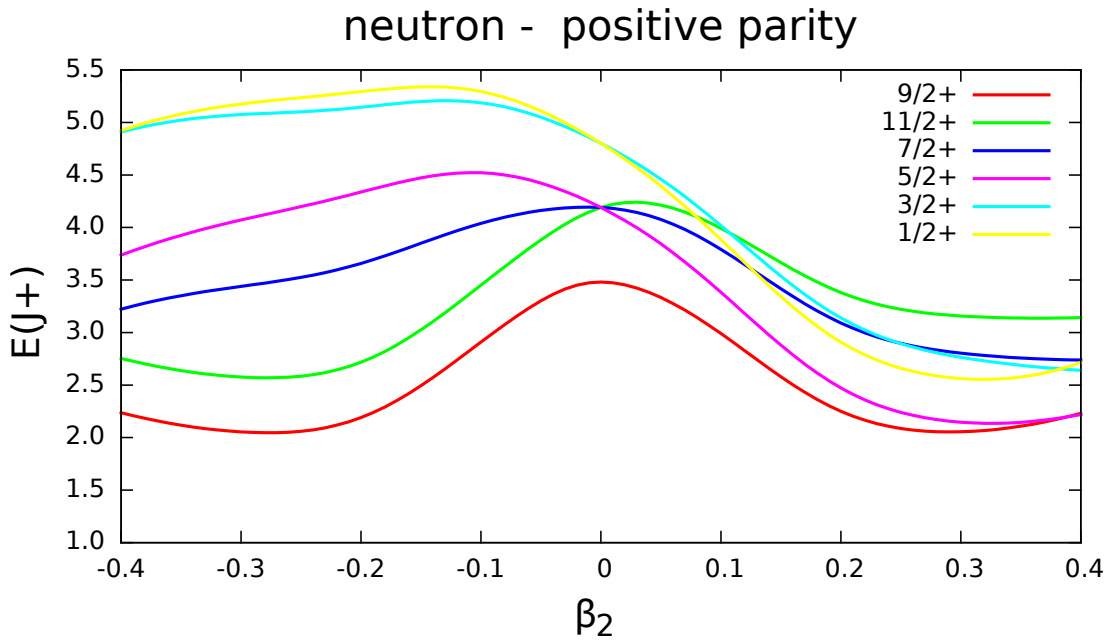

Figure 6.11: The neutron levels with positive parity states in the daughter nucleus ^{71}Kr as a function of deformation from -0.4 (oblate) to +0.4 (prolate). The lowest state is predicted to be $9/2^{+}$.

6.5.1 Energy levels in ^{72}Rb

In the calculations performed to date, the proton-neutron residual interaction is missing. Therefore, the ordering of the levels is not likely to be entirely correct. However, the wave-functions and the half-lives should not differ much. Also, the absolute energies are not important, since only the energies relative to the ground state of the daughter nucleus have physical meaning.

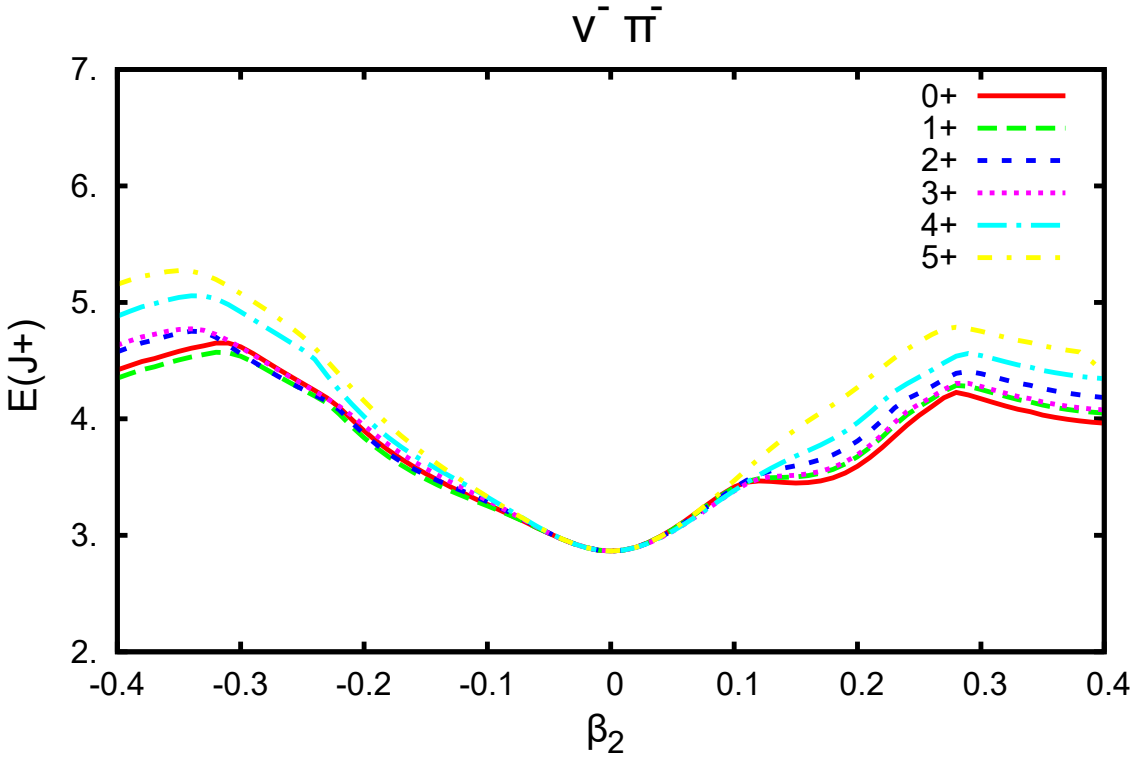

Figure 6.12: Energy of positive parity states as a function of deformation from -0.4 (oblate) to +0.4 (prolate). The lowest yrast levels with positive total parity and neutron and proton in negative parity for ^{72}Rb.

Shown in Fig. 6.12 are the lowest yrast levels with positive total parity, with the odd neutron and proton occupying negative parity levels/ orbits. In each case, the levels are the result of $\pi f_{5/2} \times \nu f_{5/2}$ components at zero deformation. In accordance of the Gallagher-Moszkowski rule [158], the lowest state would be expected to be the 5^+ state.

Fig. 6.13 shows the lowest yrast levels with negative total parity and a neutron in negative parity level and a proton in a positive parity level. These levels arise mainly from $\nu f_{5/2} \times \pi g9/2$ at zero deformation. In this case, according to the Gallagher-Moszkowski rule, the lowest state would be expected to be the 2^- state.

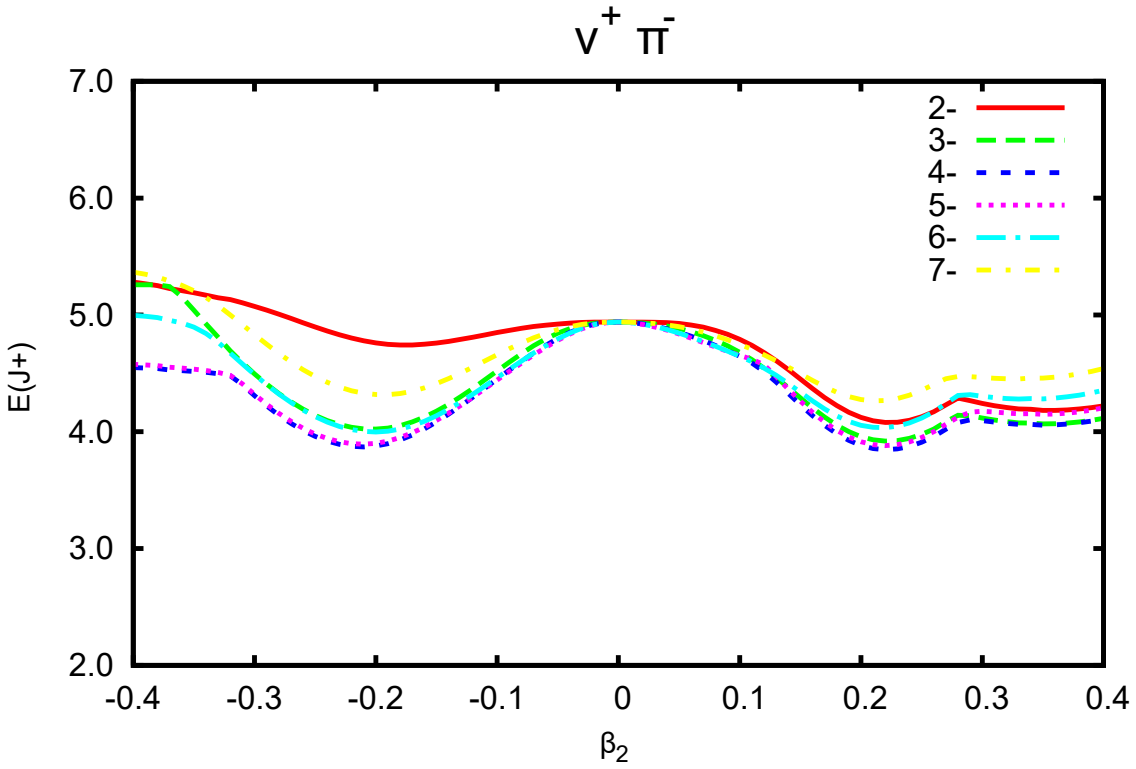

Figure 6.13: Energy of negative parity states as a function of deformation from -0.4 (oblate) to +0.4 (prolate). The lowest yrast levels with negative total parity and neutron in negative parity level and proton in positive parity for ^{72}Rb.

The lowest yrast levels with negative total parity and a neutron in positive parity level and a proton with a negative parity level are shown Fig. 6.14. These levels arise mainly from $\nu g_{9/2} \times \pi f_{5/2}$ at zero deformation. In this case, according to the Gallagher-Moszkowski rule, the lowest state would be expected to be the 2^- state.

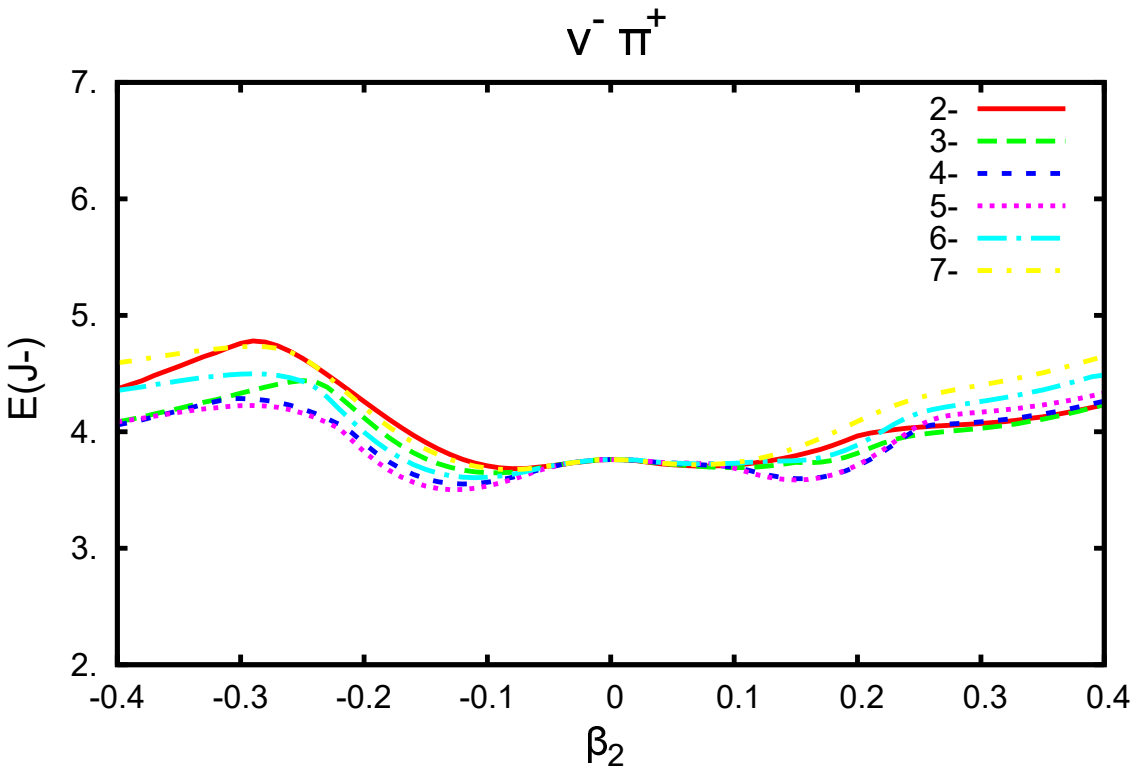

Figure 6.14: Energy of negative parity states as a function of deformation from -0.4 (oblate) to +0.4 (prolate). Lowest yrast levels with negative total parity and neutron in positive parity level and proton in negative parity for ^{72}Rb.

The lowest yrast levels with positive total parity and a neutron and a proton in positive parity level, are shown in Figs. 6.15 and Fig. 6.16, respectively. These levels arise mainly from $\pi g_{9/2} \times \nu g_{9/2}$ at zero deformation. Following the Gallagher-Moszkowski rule, the lowest state would be expected to have a spin of 9^+. In this case the levels rapidly decrease in energy, with increasing prolate/oblate deformation, because of the down-sloping of the K=$1/2^+$ and $3/2^+$ states for positive deformation, and K=$9/2^+$, $7/2^+$ states for negative deformation. This brings them down crossing the Fermi surface, and decreasing the quasi-particle energy, which leads to an increase in the deformation.

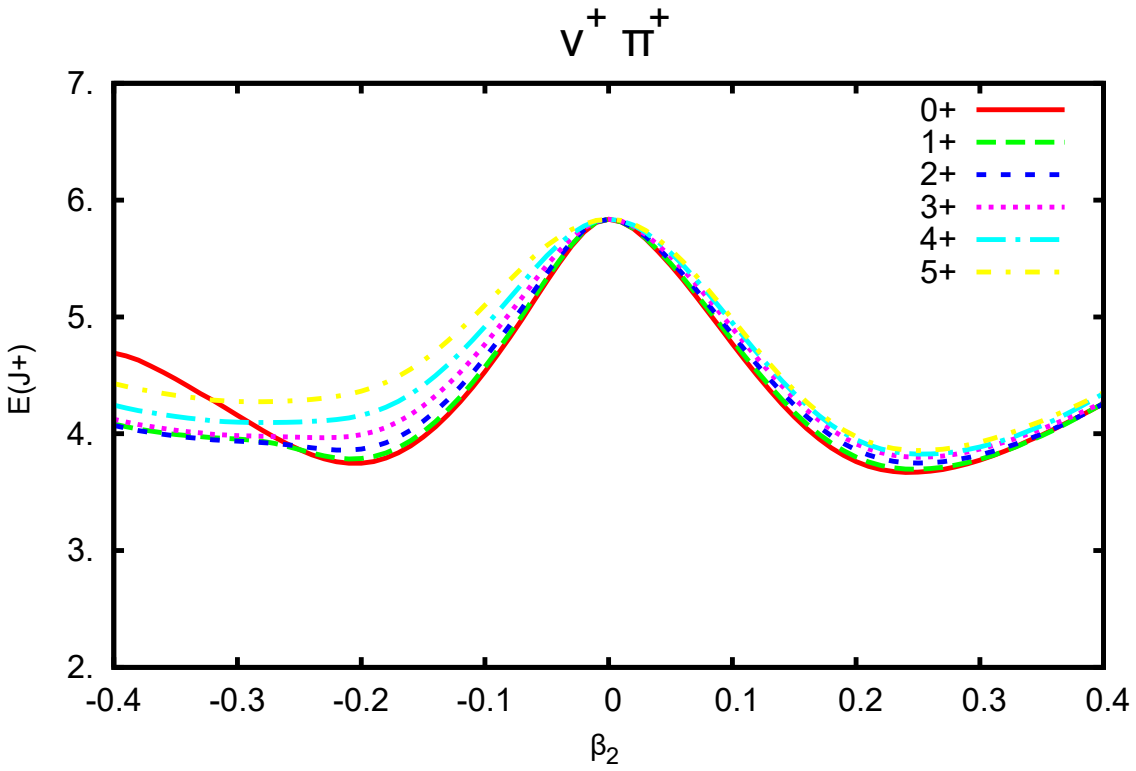

Figure 6.15: Energy of positive total parity as a function of deformation from -0.4 (oblate) to +0.4 (prolate). Lowest yrast levels with positive total parity and neutron and proton in positive parity level for ^{72}Rb.

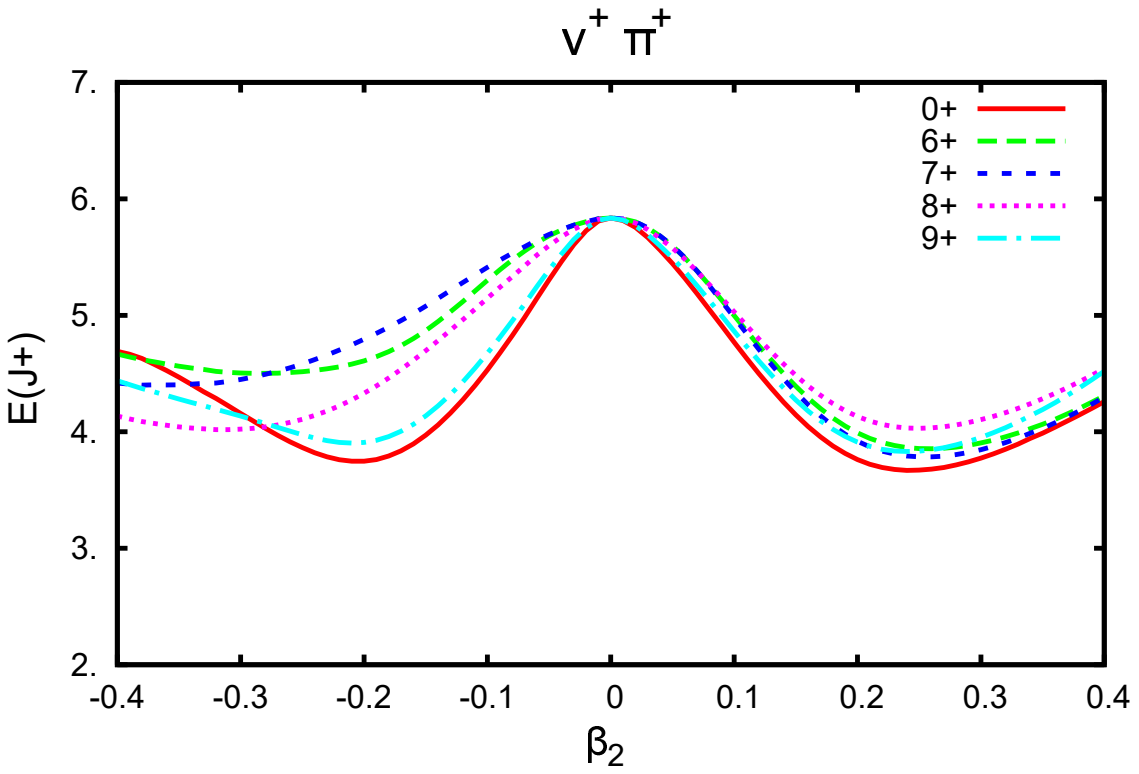

Figure 6.16: Energy of positive total parity as a function of deformation from -0.4 (oblate) to 0.4 (prolate). Lowest yrast levels with positive total parity and neutron and proton in positive parity level for ^{72}Rb.

The data indicates that for small deformation, the lowest levels result from neutron and proton in negative parity levels (i.e. $f_{5/2}$). For large deformation, the lowest levels result from neutron and proton in positive parity levels (ie. $g_{9/2}$).

6.5.2 Half-lives of ^{72}Rb

The half-lives for proton emission from the parent nucleus yrast states to the daughter nucleus yrast states were calculated. The calculations discussed each assume proton decay to the lowest states to the $9/2^+$, $5/2^-$ and $1/2^-$ levels of the daughter nucleus, ^{71}Kr.

Fig. 6.17 shows the theoretical proton emission half-lives as a function of deformation for a proton energy of 600 keV. Shown are the decays from levels in ^{72}Rb to levels in ^{71}Kr, specifically the 5^+ state, coming from the $5/2^-\times5/2^-$ at zero deformation, to the $1/2^-$ state, 5^+ to the $5/2^-$ and 9+ state coming from the $g_{9/2}\times g_{9/2}$ at zero deformation, to the $9/2^+$ state. The experimental half-life from this work was determined to be 77(21) ns.

Fig. 6.18 shows the theoretical proton emission half-lives as a function of proton energy

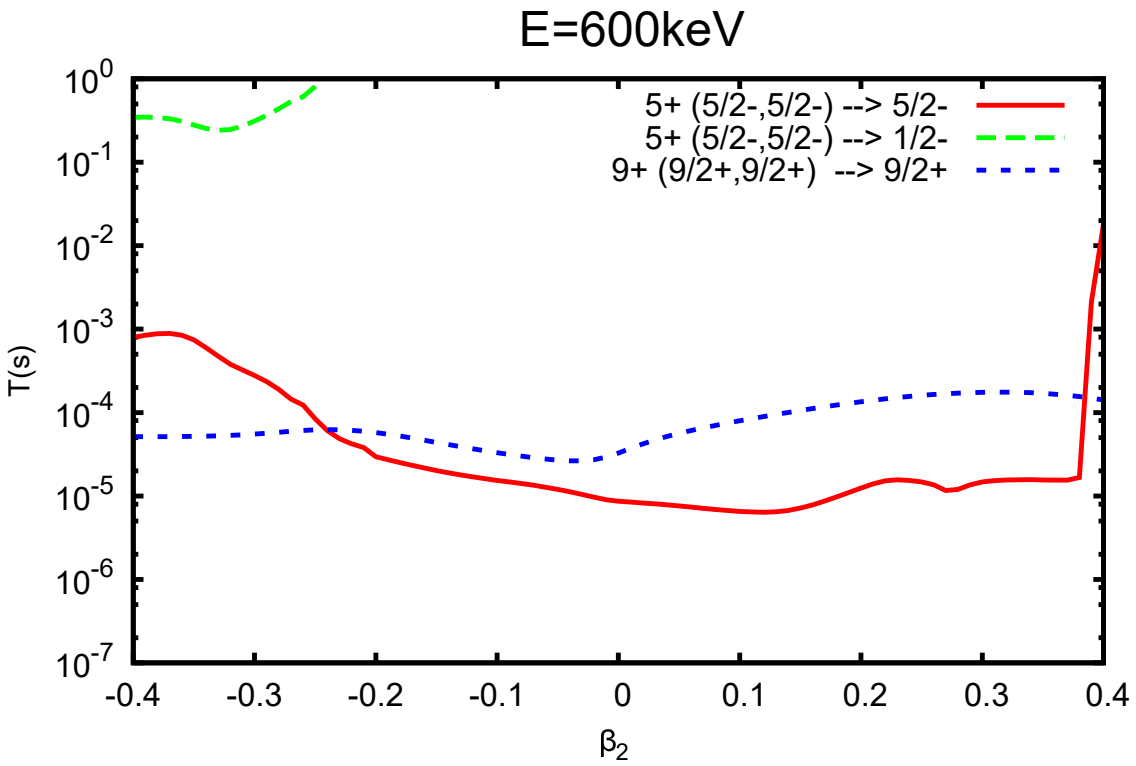

Figure 6.17: Theoretical proton emission half-lives as a function of deformation for a proton energy of 600 keV. Shown are the decays $5^+(5/2^-\times5/2^-)$ to the $1/2^-$, $5+(5/2^-\times5/2^-)$ to the $5/2^-$ and $9+(9/2^+\times9/2^+)$ to the $9/2^+$ for ^{72}Rb.

for the decay $5^+(5/2^-\times5/2^-)$ to the $1/2^-$. The experimentally determined half-life of 77(21) ns suggests a very high proton decay energy for the 5^+ state decaying to the $1/2^-$ state at large negative deformation, which could be the ground state.

Fig. 6.19 shows half-lives as a function of proton energy for the decay $5+(5/2^-\times5/2^-)$ to the $5/2^-$. The experimentally determined half-life of 77(21) ns suggests a proton decay energy of around 720 keV for the 5^+ state decaying to the $5/2^-$ state at large positive deformation or between 800 and 900 keV at large negative deformation.

Fig. 6.20 shows the theoretical proton emission half-lives as a function of proton energy for the decay $9^+(9/2^+\times9/2^+)$ to the $9/2^+$. The experimentally determined half-life of 77(21) ns suggests for the 9^+ state an energy of 810 keV at large negative deformation and an energy of 850 keV at large positive deformation.

The realibility of the lifetimes of the states in Figs. 6.18, 6.19 and 6.20 are dependent on the parametrisation of the Wood-Saxon potential used. It is mainly influenced by the radius, and strength of the spin-orbit interaction, which effect the relative position of the

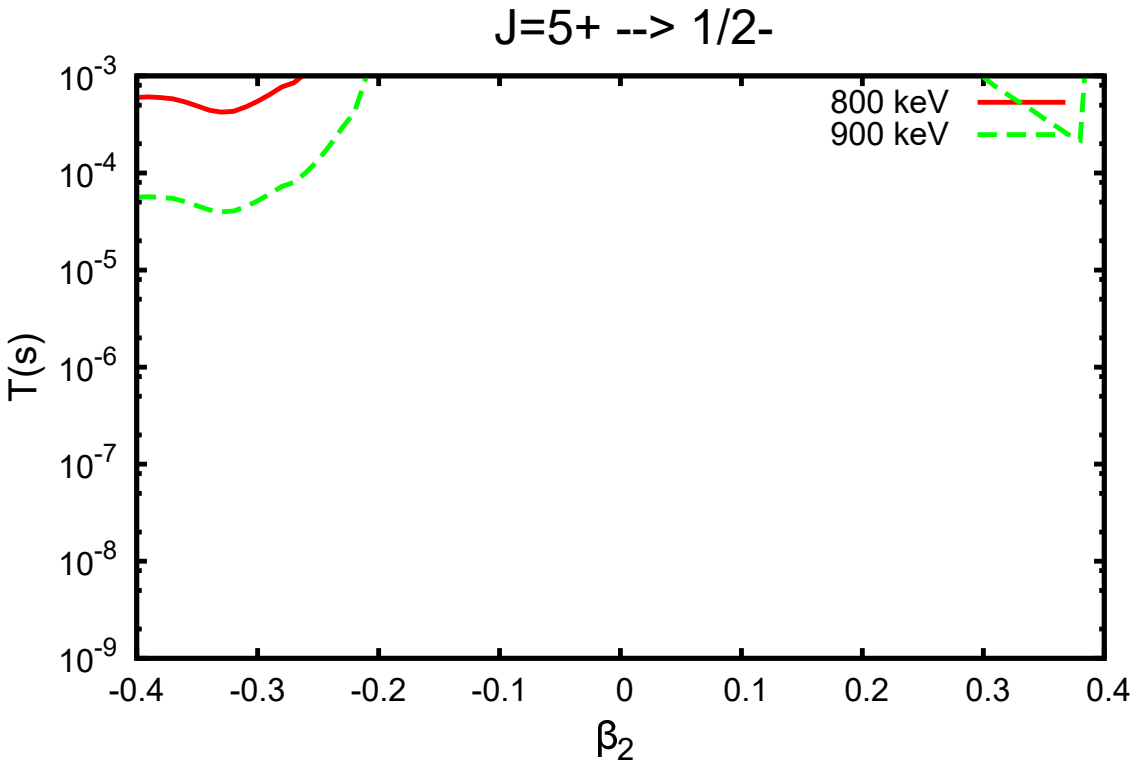

Figure 6.18: Theoretical proton emission half-lives as a function of proton energy for the decay $5^+(5/2^-\times5/2^-)$ to the $1/2^-$ for ^{72}Rb.

single particle levels. Using reasonable potentials, the change of the half-life will be less than a factor of 2, see Ref. [159].

In the case of the $9^+ \rightarrow 9/2^+$, the lowest angular momentum of the escaping proton is $9/2^+$. Higher angular momenta are not very important, since they mix very little in the Nilsson wave-functions. Therefore, the only components that could change the wave-function, and thus decrease the $g_{9/2}$ component, increasing the lifetime are:
1) The $d_{5/2}$. The probability of this component depends on the distance in energy between the $g_{9/2}$ and the $d_{5/2}$, and is dependent on the strength of the spin-orbit interaction. However, the effect of this should not be very large, and should not significantly decrease the probability of having the $g_{9/2}$ state. If the $d_{5/2}$ state couples to the 2^+ of the even-even core, and in the ground state of ^{71}Kr there is also a component with this 2^+ state.
2) Components with the $g_{9/2}$ coupled to the 2^+ of the core.

The state mixing is dependent on the spectrum of the core. For these calculations ^{72}Kr was used, since the appropriate details for ^{70}Kr are unknown.

In the case of the 5^+ state, the situation is more complicated, because the spherical

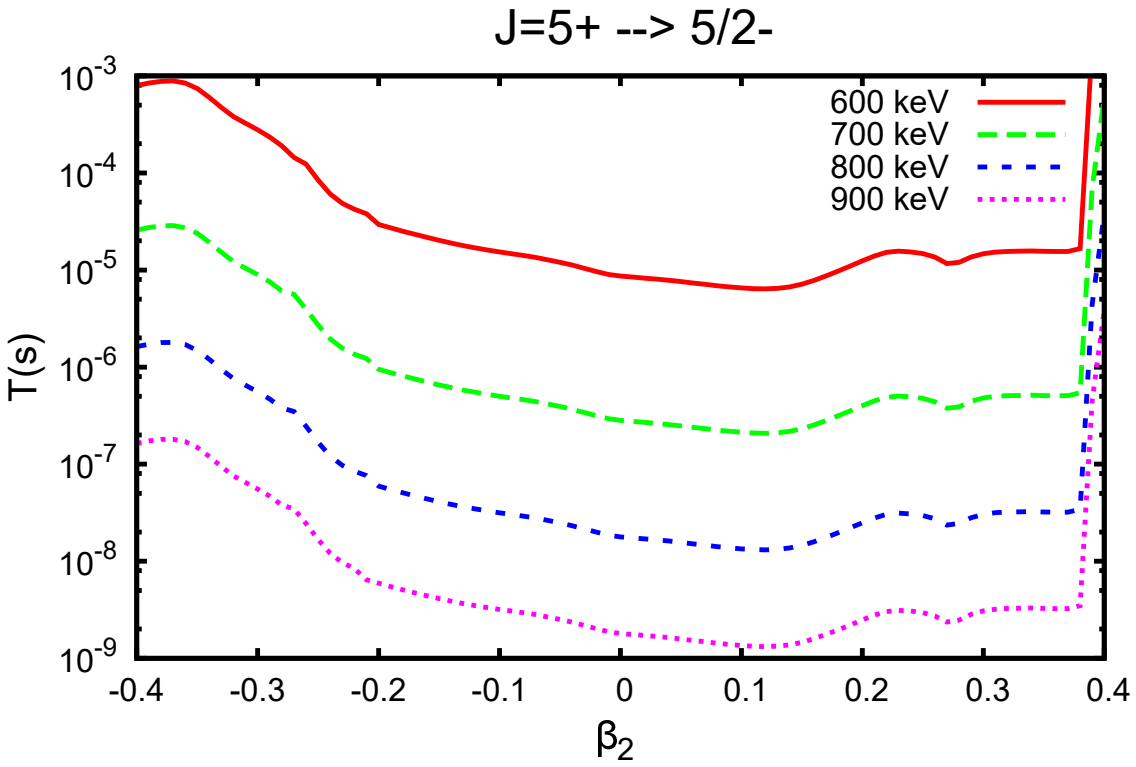

Figure 6.19: Theoretical proton emission half-lives as a function of proton energy for the decay $5^+(5/2^-\times5/2^-)$ to the $5/2^-$ state.

$f_{5/2}$, $p_{3/2}$ and $p_{1/2}$ states are close by. The results depend strongly on the relative positions of these levels. For large deformations the Nilsson model can distinguish between these states, and the spherical single particle features are diminished and the wave-functions are almost independent of the parameters of the Wood-Saxon.

6.6 Discussion and conclusions

In the case of ^{72}Rb, the AME2012 [157] model predicts a larger value of -920(520) keV, the error is very large. However, assuming that the energy is 920 keV then without the change of sign in deformation, the only possibility seems to be the $g_{9/2}$ state. This implies an improbable, very small spectroscopic factor. If the decay is from the ground state to an excited state, this decreases the energy. However, if the decay is from an excited state, than the energy of the proton emitted would increase. Since the error in the AME2012 [157] prediction is very large, for smaller energies, one could reproduce the half-life of 77(21) ns with $p_{1/2}$, $p_{3/2}$ and $f_{5/2}$ states for ^{72}Rb.

For the *np* spin-aligned 9^+ state in ^{72}Rb, in the mirror nucleus, ^{72}Br, the lowest 9^+ state

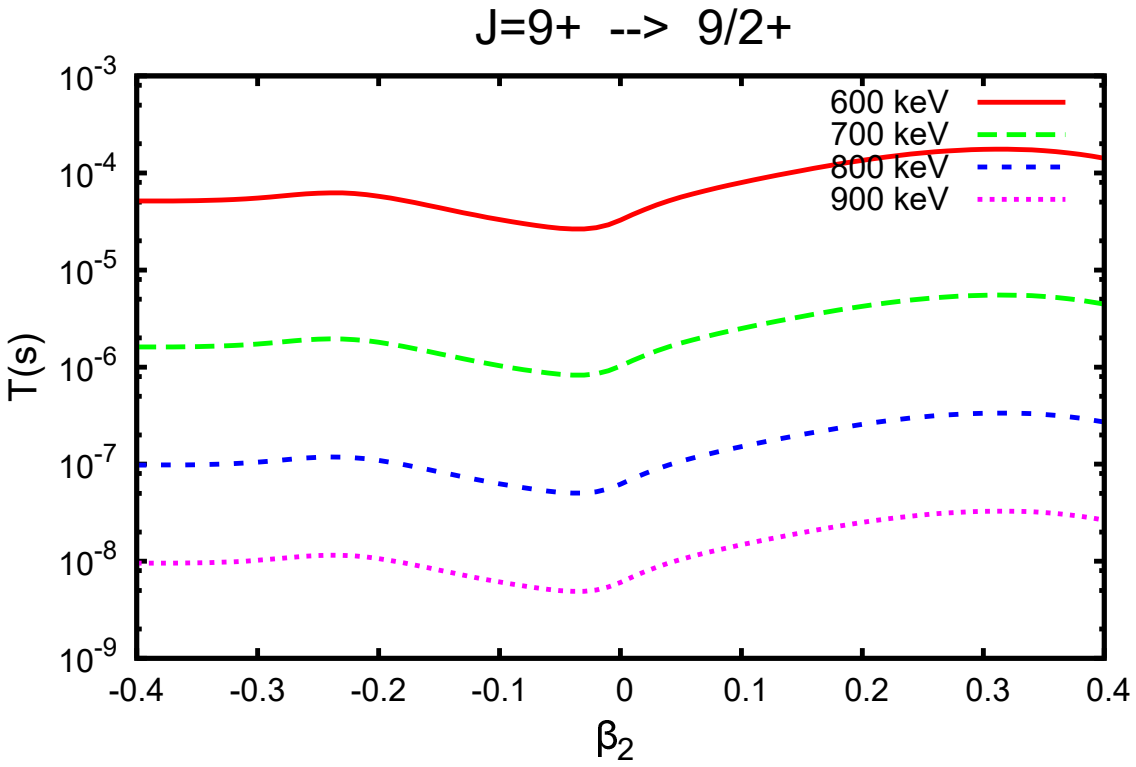

Figure 6.20: Theoretical proton emission half-lives as a function of proton energy for the decay $9^+(9/2^+ \times 9/2^+)$ to the $9/2^+$ for ^{72}Rb.

is located at 1448 keV. This state could decay to the $9/2^+$ state in the daughter nucleus, ^{71}Kr. The mirror nucleus for ^{71}Kr is ^{71}Br, for which the $9/2^+$ is located at 759 keV. This would indicate that the energy of the proton emitted would be 689 keV, which is larger than the energy available for decay from the parent ground-state to the ground-state of the daughter nucleus. Therefore, assuming the lowest value of the AME2012 prediction (-400 keV) [157], this would imply an energy of 1089 keV and an extremely small spectroscopic factor.

An remaining unknown factor is whether the mirror symmetry argument can be applied in a case where the binding is weak. In this case, the states in ^{72}Rb could reside at somewhat different energies relative to ^{72}Br. In Jenkins [154] it is stated that "mirror symmetry is a very reliable guide to the location of excited states" and that "mirror symmetry seems well supported in the mass 60-80 region." In fact, due to the Coulomb barrier, the wave-functions are quite localised inside the nucleus. Only unbound single particle states with low angular momentum (i.e. smaller centrifugal barrier) would be less localised. This would decrease the interaction of these levels, and so would increase the

energy of this level (i.e. the states with $g_{9/2}$ nucleons would not move, while those with $p_{1/2}{}^{-}$ $p_{3/2}$ would be shifted up, such that the $g_{9/2}$ states would have a smaller excitation energy with respect to the $p_{1/2}{}^{-}$ $p_{3/2}$ ground state). For instance, de Angelis *et al.* [160] found that in ^{72}Kr, the daughter nucleus of ^{73}Rb, the first excited state is a 0^+, and the second 0^+ are a mixture of prolate and oblate shapes as investigated by Bouchez *et al.* [29] and Clement *et al.* [4].

In the case of ^{76}Y, it is an α-decay from ^{72}Rb. In effect, the proton in ^{76}Y is 0.230 MeV more bound, from calculations by Moller and Nix [145], and 1.12 MeV more bound, from calculations by Kaneko *et.al* [87]. Due to the increasing importance of the $g_{9/2}$ orbit, ^{76}Y is more bound than ^{72}Rb. ^{72}Rb has a very short half-life for proton emission, while the half-life of ^{76}Y indicates that it decays mainly by β^+-decay.

It would be expected that the energy of the proton in ^{72}Rb is higher than that of ^{73}Rb. Moller and Nix [145] predicted an increase of 500 keV. In this work for ^{73}Rb, the calculations indicate an energy of at least 600 keV, therefore one would expect a higher energy for ^{72}Rb. The maximum energy occurs for the $5^+ \rightarrow 5/2^-$ decay at large oblate deformation. Since all the half-life curves are quite flat, the calculations cannot be more precise at present. Another possibility, would be the decay of the 9^+ state to an isomeric $9/2^+$ state in ^{71}Kr. In this case the separation energy would be larger than the energy of the escaping proton. However, if the reactions populate the negative proton parity, then they would decay before being detected.

In conclusion, assuming the lifetimes measured are reliable, then the observation of a few decays for ^{72}Rb can possibly be interpreted as either the proton decay of the 5^+ state (based largely on $f_{5/2}\times f_{5/2}$ configuration) to the $5/2^-$ ground state in ^{71}Kr or the decay of the 9^+ state (based on the $9/2^+\times 9/2^+$ configuration), most probably to the still unknown isomeric $9/2^-$ state in ^{71}Kr.

Chapter 7

rp-process calculations

The proton-rich, A∼70 nuclei studied in this work are on the path of the astrophysical *rp*-process, as described in Section. 1.4.2. The effect of the new measurements on the isotopic abundances produced in an *rp*-process that reaches the Sn-Sb-Te endpoint have been investigated by conducting a one-zone one-dimensional reaction-network calculation study. Full reaction-network calculations were used to explore the effects of the new half-lives of ^{73}Sr and ^{76}Y, and the higher precision half-life of ^{74}Sr, and the proton-separation energy of ^{73}Rb extracted from the β-delayed proton spectrum of ^{73}Sr measured in this work. The results of this investigation are reported in this chapter. Network calculations were discussed in detail in Section. 2.6. A brief introduction to the reaction network used is presented, and is followed by the results of the calculations performed.

7.1 Reaction-network calculation

Computer models are used to investigate the role of the *rp*-process during a Type I X-ray burst. The models vary in the level of sophistication, such as the number of zones used, or if the ashes of previous bursts compositions are included. In general, (with the input of the reaction rates, nuclear masses and half-lives) models are able to reproduce light curves, energy generation, and isotopic abundances as a function of temperature and density over the duration of the burst. Previous work by Schatz *et al.* [44] found that nucleosynthesis, in the *rp*-process, is mainly determined by nuclear masses and β-decay rates of nuclei along the proton drip-line.

Previous work by Parikh *et al.* [161, 162] has discussed the limitations of nucleosynthesis in X-ray burst models, particularly with regard to key uncertainties in the nuclear

physics input. Parikh *et al.* performed a comprehensive series of one-zone calculations in conjunction with various representative X-ray burst thermodynamic histories using ten different models. That work highlighted key nuclear reactions whose uncertainties have the largest impact on X-ray burst nucleosynthesis studies. One-zone, one-dimensional models look for changes due to different reaction rates. Therefore, a one-zone model was suitable for this work.

The nuclear reaction network for the *rp*-process was based on the code by Meyer [163] and includes 690 proton-rich nuclei, from Hydrogen to Xenon. Nuclear and reaction-rate data used in the network calculations are taken from REACLIBV2, provided through the JINA Reaclib database [79]. The parameters of the one-zone model by Schatz *et al.* [49] were chosen to investigate the effects of the new half-lives determined in this work and the first estimate of the S_p value deduced for ^{73}Rb. The one-dimensional, one-zone X-ray burst model calculates temperature and density in the burning zone assuming constant pressure. The requirements of the model were that the burst is capable of reaching and processing material up to, and beyond, the ^{72}Kr waiting point. The initial conditions of the burst assume a solar abundance of H, He and a metallicity of Z=10^{-3}. In all simulations in this work, processing occurs on burst timescales of $\sim$ 200 s to correspond to a rise time of $\approx$ 4 s, and a cooling phase of $\approx$ 200 s [49].

Mass models may also be used to determine critical proton-separation energies around waiting points. The effects of using different mass models has previously been explored by Schatz *et al.* [44]. Schatz *et al.* compared the FRDM (1992) and Hilf *et al.* mass models, and found that the mass predictions are sufficient for an approximate determination of the reaction path. However, the reliability, and therefore the quality of the reaction network calculations, depends critically on the accuracy of the nuclear masses used to determine the position of the proton drip-line. As the reaction path for given temperature, density, and composition is almost entirely determined by proton capture Q-values, the macroscopic-microscopic finite range droplet mass model (FRDM 2012) [164] was employed for this network calculation.

The ignition temperature for thermonuclear run-away is T_9=0.3. The density is initially around 1.1×10^6 g/cm^{-3} and drops to 2.0×10^5 g/cm^{-3} when the peak temperature of T_9=2 is reached. For a dynamic hydrogen burning calculation the profiles of ρ and T_9 were determined by [163]:

$$\rho(t) \;=\; \rho_o e^{-t/\tau}, \tag{7.1}$$

and

$$T_9(t) \;=\; T_{9,o}e^{-t/3\tau}. \tag{7.2}$$

When τ is a finite value, the density will decline exponentially with time. When $\tau \to \infty$ the temperature and the density remains fixed at the intial values, i.e. in a steady state.

7.2 Verifying the calculation

To test the consistency of the results obtained in this work, the results from the model were compared to the previous results obtained by Schatz *et al.* [49], the steady-state and explosive models described by Schatz *et al.* were replicated, using the separation energies from Ref. [165] shown in Table. 7.1.

Table 7.1: The proton-separation energies for some of the key isotopes in the *rp*-process. S_p and uncertainties in MeV from Ref. [165].

Nucleus	Separation energy, S_p (MeV)
^{65}As	-0.36 ± 0.15
^{69}Br	-0.81 ± 0.10
^{73}Rb	-0.70 ± 0.10
^{66}Se	2.43 ± 0.18
^{70}Kr	2.58 ± 0.16
^{74}Sr	2.20 ± 0.14

The X-ray burst conditions and proton-separation energies used by Schatz *et al.* [49] were replicated and these values were used throughout this work, unless otherwise stated.

7.3 Investigating the effects of different separation energies

One of the key goals of the RIBF97 experiment was to measure the β-delayed proton spectrum of ^{73}Sr in order to extract a value for the S_p of ^{73}Rb. To understand the impact of the effect of the proton-separation energy of ^{73}Rb, the tentative estimate S_p of ^{73}Rb was investigated as well as exploring the effects of the proton-separation energy at extreme limits. The effect of the proton-separation energies of nuclei observed in this work, ^{72}Rb, ^{76}Y and ^{77}Zr, near the waiting point nuclide ^{72}Kr of the *rp*-process, were also investigated.

7.3.1 ^{73}Rb

Jenkins [154] discussed the nature of the proton binding energy of ^{73}Rb, based on the non-observation of ^{73}Rb in projectile fragmentation experiments. Jenkins suggested that the likely range of S_p values was -500-900 keV. The proton emission calculations discussed in the previous chapter indicated that the minimum S_p for ^{73}Rb is > -600 keV. In this work the S_p of ^{73}Rb is estimated to be -800±70 keV from the β-delayed proton spectrum of ^{73}Sr and subsequent GEANT4 simulations. In order to investigate the effects of this proton-separation energy for ^{73}Rb, different limits and extremes of proton-separation energies were explored.

7.3.2 No two-proton capture (S_p = -1500 keV)

The ^{73}Rb S_p value was set to -1500 keV, effectively disabling the ^{72}Kr(2p,γ)^{74}Sr reaction in the *rp*-process network.

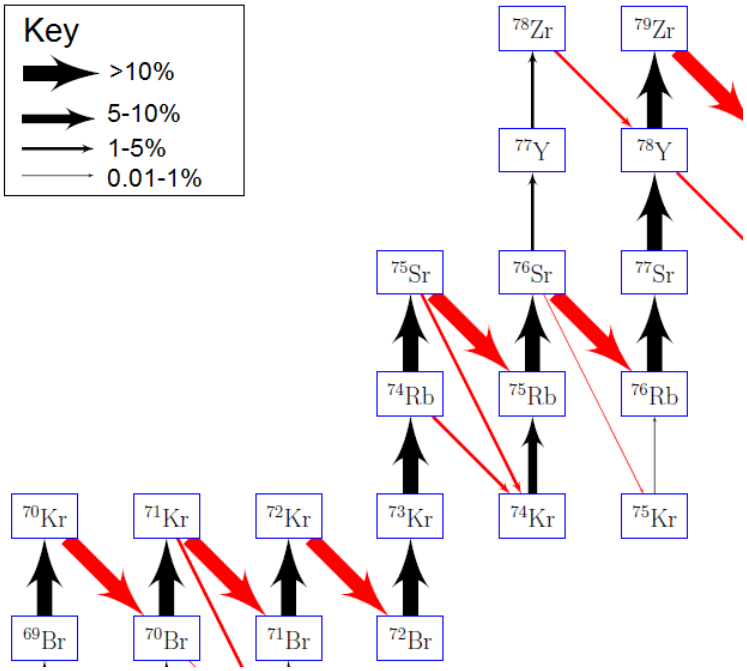

Figure 7.1: The pathway of the *rp*-process in the region of interest during a XRB at T_9=1.5, $\rho = 1.6\times10^6$ g/cm^{-3} for nuclei in the A∼70 region. Shown are the reactions; the black lines represent proton capture, and the red lines represent the various decay modes (i.e. β-decay, and β-delayed proton decay). The thickest line represents a flow of over 10%, the second 5-10%, the third 1-5% and the thinnest line represents 0.1-1% for ^{73}Rb, modelled at S_p = -1500 keV.

Furthermore, as ^{73}Rb is found from the present work to be highly unbound, there are virtually no ^{73}Rb nuclei present to undergo proton capture. As a result, the abundance of ^{74}Sr is near zero. Fig 7.1 shows the results for the time integrated reaction flow during an X-ray burst (XRB).

7.3.3 Non-observation limit (S_p = -500 keV)

For the purposes of comparison, the simulation was also run with the ^{73}Rb value fixed at S_p = -500 keV. This corresponds to the non-observation limit. However, in comparison with Fig. 7.1, a larger abundance of ^{73}Rb is produced, which is observed to increase the amount of ^{74}Sr, reflecting the stronger reaction flow, bypassing the waiting point via the sequential two-proton capture through ^{73}Rb as shown in Fig. 7.2.

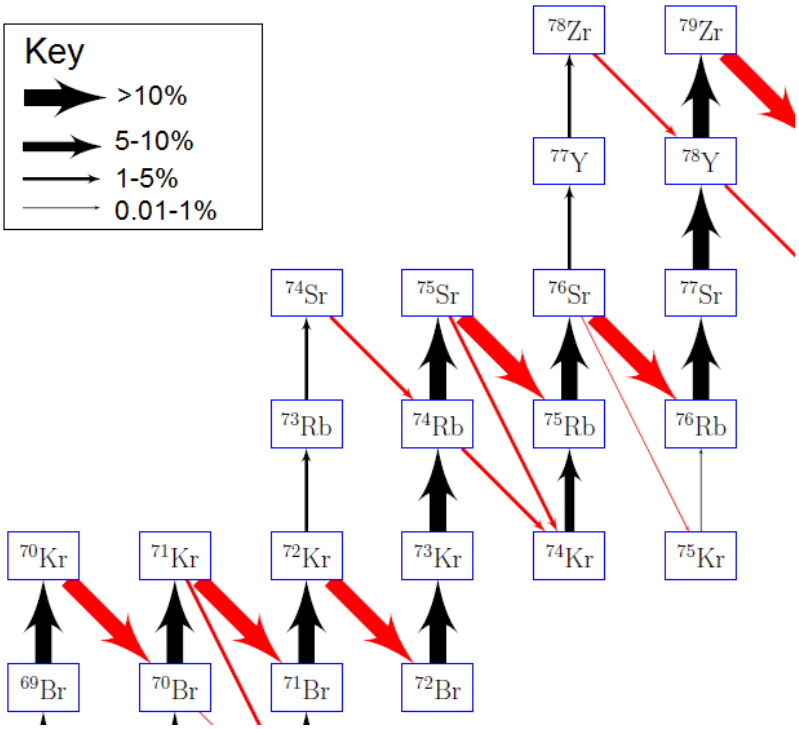

Figure 7.2: The pathway of the *rp*-process in the region of interest during a XRB at T_9=1.5, $\rho = 1.6\times10^6$ g/cm^{-3}. The line styles notation is the same as Fig. 7.1. Simulation modelled with $S_p(^{73}\text{Rb})$ = -500 keV. It can be seen that there is a flow into ^{73}Rb.

7.3.4 Limits of stability (S_p = 0 keV)

To exaggerate the influence of ^{73}Rb, a further simulation was run for S_p = 0 keV. However, now a larger abundance of ^{73}Rb is produced which is observed to increase the amount of

^{74}Sr, reflecting the larger amount of the reaction flow that bypasses the waiting point via the sequential two-proton capture through ^{73}Rb as shown in Fig. 7.3.

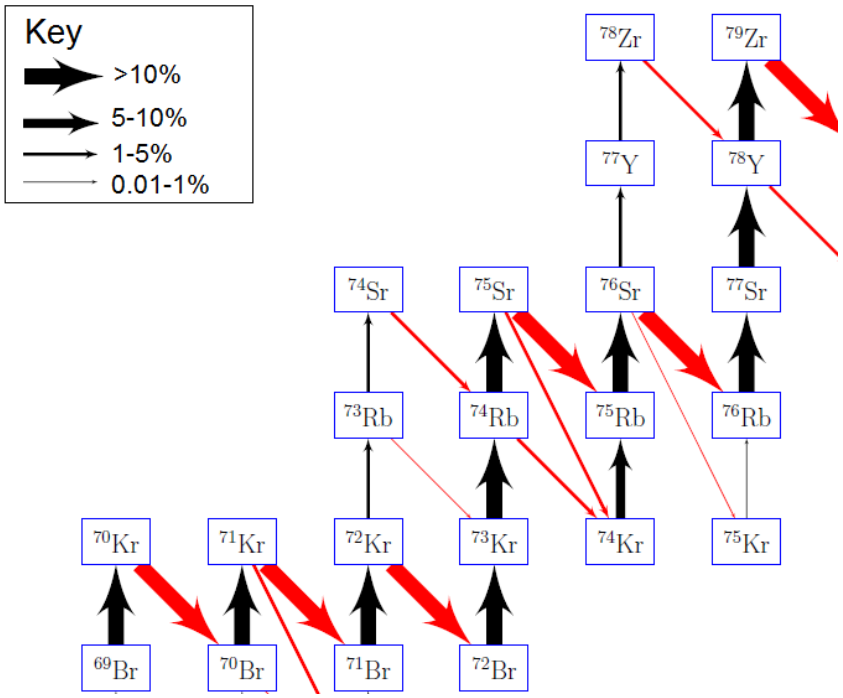

Figure 7.3: The pathway of the *rp*-process in the region of interest during a XRB at T_9=1.5, $\rho = 1.6\times10^6$ g/cm^{-3}. The line styles notation is the same as Fig. 7.1. Simulation modelled with S_p = 0 keV.

7.3.5 Simulation performed using the S_p value extracted from present work for ^{73}Rb

The effects of the ^{73}Rb proton-separation energy found in this work were investigated with the simulation was run with S_p = -800±70 keV and the upper and lower limits -870- and -730 keV, respectively, i.e. one σ limits for the errors. The results are similar to the prior subsections. The ^{74}Sr abundance indicates the processing occurs through two-proton capture. At S_p =-800 keV, as shown in Fig. 7.4, ^{73}Rb is still very unbound, which is reflected by its lack of production in the calculations.

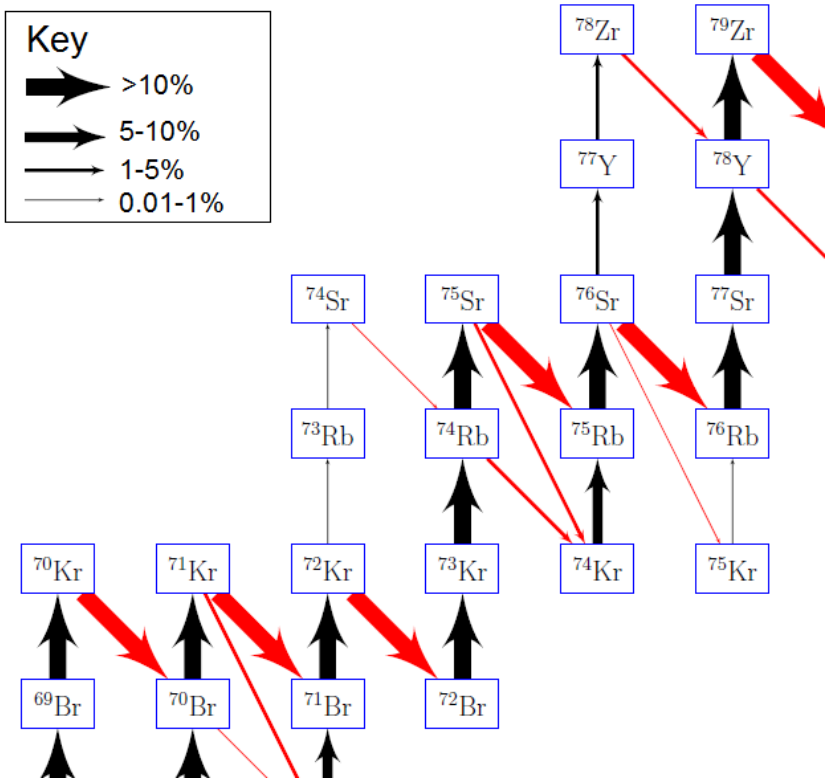

Figure 7.4: The pathway of the *rp*-process in the region of interest during a XRB at T_9=1.5, $\rho = 1.6\times10^6$ g/cm^{-3}. The line styles notation is the same as Fig. 7.1. The proton-separation energy measured in this work at S_p = -800 keV.

7.3.6 ^{72}Rb

The effects of the proton-separation energy of ^{72}Rb were probed. In the previous chapter, several counts of ^{72}Rb were found and proton emission calculations were performed. ^{72}Rb is proton-unbound. In contrast to the network calculations for ^{73}Rb, the proton-separation energy set at $S_p = 0$ keV, yields no pathway to ^{73}Sr being populated as shown in Fig. 7.5. The effects of ^{72}Rb being slightly bound were explored. At a proton-separation energy of $S_p = 0.5$ MeV there was a minor branch to ^{72}Rb, as shown in Fig. 7.6.

If ^{72}Rb was populated during the *rp*-process, it would still be unable to bypass the ^{72}Kr waiting point as a result of ^{73}Rb being proton unbound.

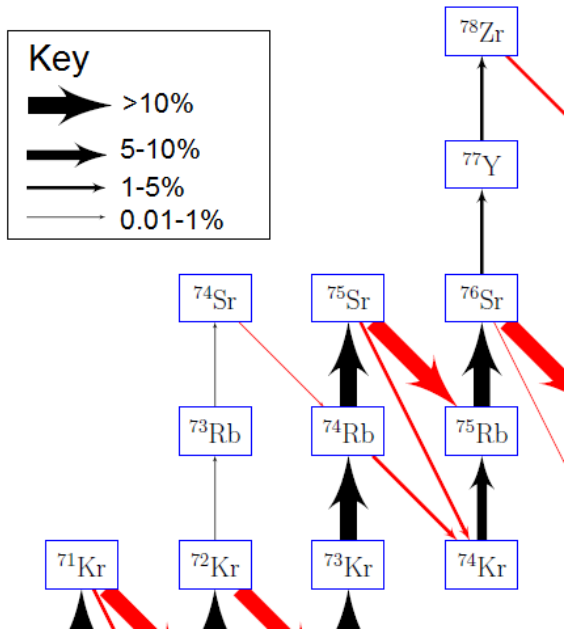

Figure 7.5: The pathway of the *rp*-process in the region of interest during a XRB at T_9=1.5, $\rho = 1.6\times10^6$ g/cm^{-3}. The line styles notation is the same as Fig. 7.1. Simulation modelled with $S_p = 0$ keV.

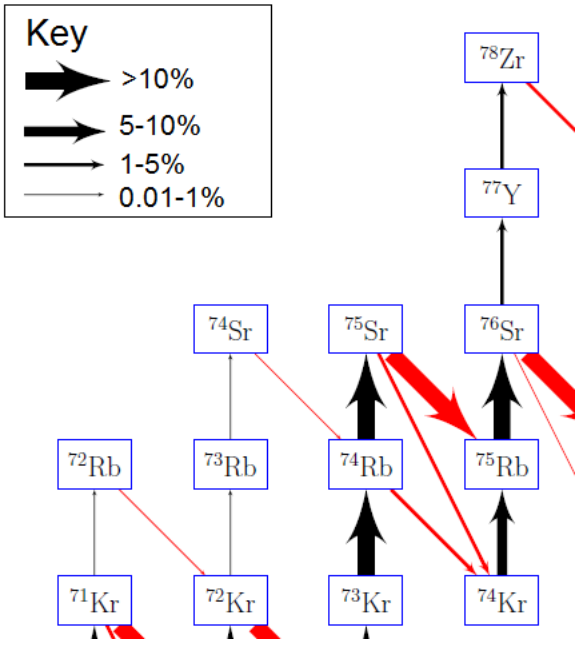

Figure 7.6: The pathway of the *rp*-process in the region of interest during a XRB at T_9=1.5, $\rho = 1.6\times10^6$ g/cm^{-3}. The line styles notation is the same as Fig. 7.1. Simulation modelled with $S_p = 0.5$ MeV.

7.3.7 Exotic proton drip-line

The T_z =-1/2 odd-Z nuclide, ^{77}Y half-life has been measured previously to be 57^{+22}_{-12} ms [131], and is consistent with essentially 100% β^+-decay. Given the $T_{\frac{1}{2}}(^{76}\mathrm{Y}) = 24^{+12}_{-6}$ ms and the observation of ^{77}Zr, it can be suggested that these nuclei are proton-bound and that they can be populated in the *rp*-process. The S_p for ^{76}Y and ^{77}Zr were investigated, to create a more exotic pathway, close to the drip-line. Current predictions of S_p are given in Table. 7.2.

Table 7.2: The predicted S_p of exotic nuclei explored in this work.

Nuclide	Separation energy, S_p, (MeV)
^{76}Y	-0.57 [145]
^{76}Y	-0.61 [87]
^{77}Zr	-0.21 [87]

In order to investigate the effects of the ^{76}Y proton-separation energy, simulations were run for $S_p = 0$ MeV, 0.5 MeV, 0.75 MeV and 1.0 MeV. The ^{76}Y branch was not populated at 0 MeV, at 0.5 MeV the branching moves to 0.1-1% and for 0.75 MeV 1-5% and whilst when set to 1 MeV a stronger branch occurs at over 10% flow.

The effects of the ^{77}Zr proton-separation energy were investigated with the simulation run for $S_p = 0.5$ and 1 MeV for ^{76}Y, and then 0.5 MeV, 0.75 MeV, 1.0 MeV and 1.25 MeV for ^{77}Zr. The ^{77}Zr branch was not populated at 0.5-1 MeV, at 1.25 MeV the branching is 5-10%. As shown in Fig. 7.7, the S_p for ^{76}Y would need to be at least 1.0 MeV and the S_p for ^{77}Zr would have to be at least 1.25 MeV for the *rp*-process to proceed in a more exotic manner.

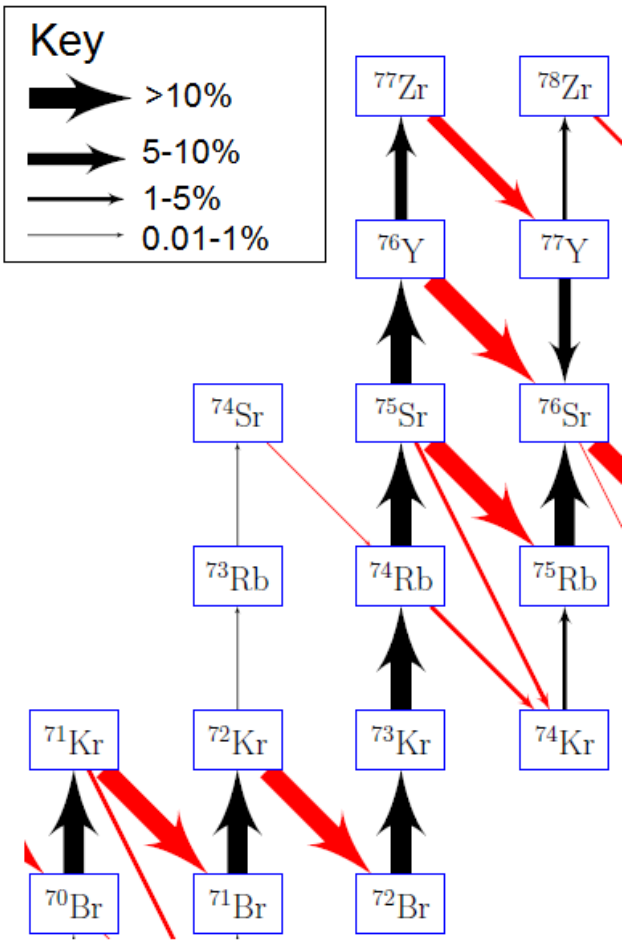

Figure 7.7: The pathway of the *rp*-process in the region of interest during a XRB at T_9=1.5, $\rho = 1.6\times10^6$ g/cm^{-3}. The line styles are the same as Fig. 7.1. To populate ^{76}Y and ^{77}Zr in the network calculations in this work, the proton-separation energies of ^{76}Y and ^{77}Zr were explored. The values were $S_p{}^{76}\mathrm{Y} = 1.0$ MeV and $S_p(^{77}\mathrm{Zr}) = 1.25$ MeV.

7.4 Effect of the newly measured half-lives on the *rp*-process

Rodríguez *et al.* [59] measured the mass of ^{72}Kr in order to determine its role in the *rp*-process. It was concluded that the ^{72}Kr lifetime will delay the burst duration with at least 80% of its β-decay half-life. In most models, the reduction in the proton capture rates will be less, as densities during the burst tend to drop somewhat below 10^6 g/cm^3 due to expansion, and the Hydrogen abundance tends to be reduced compared to the solar value, at the time the reaction flow reaches ^{72}Kr. Schatz *et al.* [165] found that varying the ^{74}Sr half-life between 10-100 ms varied the ^{72}Kr effective lifetime by about 10%. Therefore,

using the temperature T_9=1.5 K and density=10^6 g/cm^3 the effective lifetime can be given (following Ref. [59]) by:

$$T_{eff}(^{72}Kr) \;=\; 0.8 * T(^{72}Kr) + 0.2 * T(^{74}Sr). \tag{7.3}$$

The half-lives of ^{73}Sr ($T_{1/2}$=28^{+5}_{-4} ms), ^{76}Y ($T_{1/2}$= 24^{+12}_{-6} ms) and ^{74}Sr ($T_{1/2}$= 27.7(28) ms) measured in this work were used in the network calculations. The half-life of ^{72}Kr has been measured previously as 17.1(2) s [53]. As ^{73}Sr and ^{76}Y are not populated in the network path in this specific network calculation, there is no effect from the half-lives of these isotopes.

To investigate the effect of measured half-life for ^{74}Sr, the half-life was varied between 10-100 ms. The half-life was varied as a function of the proton-separation energy measured in this work, including an upper and lower limit of one σ limits of the S_p.

The flow is defined as the contribution per nucleon per second to the abundance of one of the product species in the reaction. The net flow is the difference between the forward flow and the reverse flow. The half-life of ^{74}Sr was varied between 10-100 ms, as shown in Table. 7.3, to investigate the resultant effect on the effective lifetime of ^{72}Kr with measured half-life of ^{74}Sr in this work. The proton-separation energy for ^{73}Rb of S_p = -800 keV, deduced from the present work, was used.

Table 7.3: The net reaction flow rate for bypassing ^{72}Kr as a function of the half-life of ^{74}Sr. Using the S_p=-800 keV found in this work, the half-life of ^{74}Sr was varied.

$T_{1/2}(^{74}Sr)$ (ms)	Net flow /nucleon/s
10	4.727×10^{-22}
27.7	1.361×10^{-21}
50	2.378×10^{-21}
75	3.579×10^{-21}
100	4.795×10^{-21}

It was found that by varying the ^{74}Sr half-life between 10-100 ms varied the ^{72}Kr effective lifetime by about 10% which agrees with the result obtained by Schatz *et al.* [165].

The proton-separation energy for ^{73}Rb was modelled at S_p =-730 keV, the lower limit of the S_p deduced from the present work. The results are shown in Table. 7.4. By varying the ^{74}Sr half-life the ^{72}Kr effective lifetime varied by about 9.8%.

Table 7.4: The net reaction flow rate for bypassing ^{72}Kr as a function of the half-life of ^{74}Sr. Using the S_p=-730 keV, as the lower limit of the S_p found in this work, the half-life of ^{74}Sr was varied.

$T_{1/2}(^{74}Sr)$ (ms)	Net flow /nucleon/s
10	1.03×10^{-21}
27.7	3.175×10^{-21}
50	5.549×10^{-21}
75	8.35×10^{-21}
100	1.117×10^{-20}

The proton-separation energy for ^{73}Rb was modelled at S_p =-870 keV, the upper limit of the S_p deduced from the present work. The results are shown in Table. 7.5. This resulted in the ^{72}Kr effective lifetime varying by about 9.9%.

Table 7.5: The net reaction flow rate for bypassing ^{72}Kr as a function of the half-life of ^{74}Sr. Using the S_p=-870 keV, as the upper limit found in this work, the half-life of ^{74}Sr was varied.

$T_{1/2}(^{74}Sr)$ (ms)	Net flow /nucleon/s
10	2.026×10^{-22}
27.7	5.831×10^{-22}
50	1.019×10^{-21}
75	1.534×10^{-21}
100	2.052×10^{-21}

Fig. 7.8 and Fig. 7.9 show the abundance distribution of Sr, with the half-life varied between 10-100 ms and for the measured S_p of ^{73}Rb of -800$\pm$70 keV, through an X-ray burst as a function of density and temperature, respectively. Shown in Fig. 7.8 is the density of the burst, which is initially ρ=1.1×10^{6}g/cm^{-3} and drops to 2.0×10^{5}g/cm^{-3} when the peak temperature of the burst T_9=2 is reached. Shown in Fig. 7.9 the burst has an initial temperature of T_9=1.5 and the temperature varies throughout the duration of the burst. The abundance of Sr varies through the duration of the burst, and it is effected by the half-life of ^{74}Sr. The nuclide ^{72}Kr remains, therefore, a strong waiting point in the *rp*-process during X-ray bursts delaying energy generation with at least 80% of its β-decay

half-life.

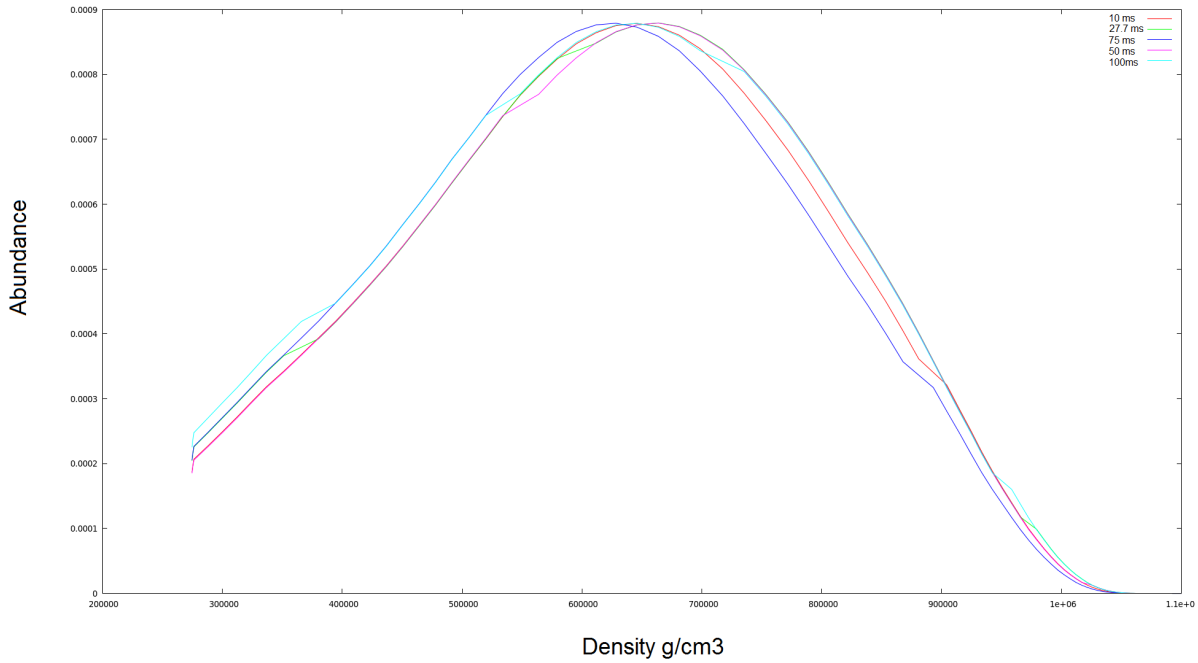

Figure 7.8: A graph of the abundance of Sr versus the density. The density is initially around 1.1×10^{6}g/cm^{-3} and drops to 2.0×10^{5}g/cm^{-3} when the peak temperature of T_9=2 is reached. The half-life of ^{74}Sr was varied between 10-100 ms for the measured S_p of ^{73}Rb of -800±70 keV. The light blue line represents a half-life, $T_{1/2}$=100 ms, the purple line is $T_{1/2}$=50 ms, the dark blue line is $T_{1/2}$=75 ms, red line is $T_{1/2}$=10 ms and light green is $T_{1/2}$=27.7 ms, the value measured in this work.

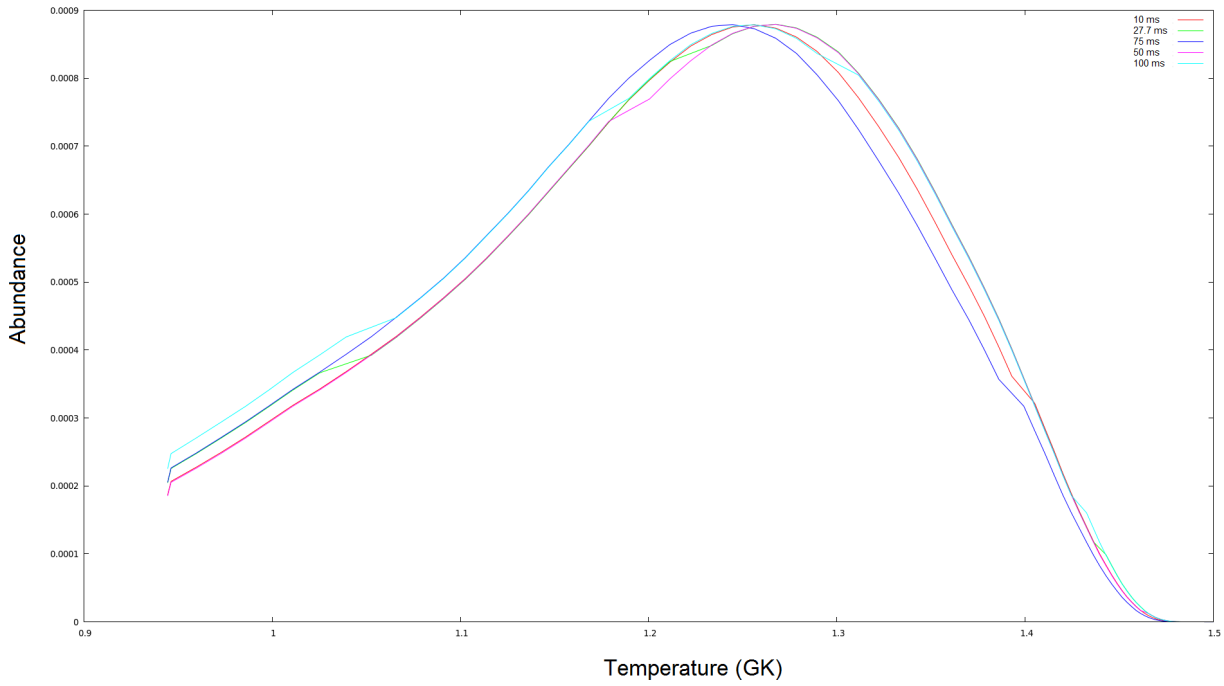

Figure 7.9: A graph of the abundance of Sr versus the temperature. An initial temperature of T_9=1.5 and varies through the burst. The half-life of ^{74}Sr was varied between 10-100 ms for the measured S_p of ^{73}Rb of -800±70 keV. The light blue line represents a half-life, $T_{1/2}$=100 ms, the purple line is $T_{1/2}$=50 ms, the dark blue line is $T_{1/2}$=75 ms, red line is $T_{1/2}$=10 ms and light green is $T_{1/2}$=27.7 ms, the value measured in this work.

7.5 Astrophysical impact

The β^+-decay half-life of ^{76}Y, $T_{1/2}=24^{+12}_{-6}$ ms, and the observation of ^{77}Zr, provides evidence that these nuclei are proton-bound and they could be populated in the *rp*-process. With the present estimate for the S_p value of ^{73}Rb being -800±70 keV, ^{73}Rb is still very unbound as reflected by the lack of its abundance. Work from the previous chapter had ^{73}Rb the S_p>600 keV, due to the estimate of the half-life. This the first "direct" experimental constraint of S_p with the β-proton summing effects accounted for and used in network calculations. From these results, the *rp*-process flux into two-proton capture is not larger than expected (i.e. ^{72}Kr is a strong waiting point). The previously used S_p=-710(100) keV comes from mirror symmetry plus Coulomb displacement energy calculations, and is therefore very theoretical. Also, there are questions on whether the uncertainty of 100 keV is realistic in a deformed region. There is a need for more accurate mass measurements

for the calculation of proton-separation energies in this region. Varying the ^{74}Sr half-life between 10-100 ms varied the ^{72}Kr effective lifetime by about 10%. However, as ^{73}Sr and ^{76}Y are not populated in the network calculations in this work, under these conditions the half-lives have no effect.

For the initial conditions in this X-ray burst simulation and the proton-separation energies and half-lives determined in this work, the abundance distribution of the uncertainties in proton-separation energy in these measurement are negligible. Therefore, to conclude, one can neglect the two-proton capture through ^{72}Kr in calculating the abundances and light curves for this type of X-ray burst. The nuclide ^{72}Kr remains, therefore, a strong waiting point in the *rp*-process during X-ray bursts delaying energy generation with at least 80% of its β-decay half-life and the path does not bypass the ^{72}Kr branch with 2-proton capture.

The mass region of A = 70–80 is a region of highly deformed nuclei, which makes the theoretical prediction of masses difficult and above ^{64}Ge there is limited experimental mass data available. To improve the accuracy of *rp*-process calculations, mass measurements to a precision of about 100 keV are crucial.

Chapter 8

Summary and conclusions

This thesis reports on the β- and γ-ray spectroscopy of proton-rich nuclei in the mass $\sim$70 region. The experiment was performed at the RIKEN Nishina Center, Japan, in the Radioactive Isotope Beam Factory (RIBF) as part of the EURICA campaign in June/July 2013. The nuclei of interest have been produced via fragmentation of a 345 MeV/nucleon ^{124}Xe primary beam on a 555 mg/cm^2 ^{9}Be target, producing a cocktail secondary beam. The nuclei of interest were then selected by the first stage of the BigRIPS and identified by a combination of its second stage and an ionisation chamber and transported to the final focal plane by the ZDS. The selected nuclei were implanted into the active stopper WAS3ABi in conjunction with EURICA.

The nuclide ^{72}Kr, with a β-decay half-life of 17.1(2) s, was thought to be a potential waiting point of the astrophysical *rp*-process. It was thought that, its lifetime in a stellar environment could be reduced by the two-proton capture reaction ^{72}Kr(p,γ)^{73}Rb(p,γ)^{74}Sr. The prime goal of the RIBF97 was to look for evidence of β-delayed proton decay from ^{73}Sr in order to try to establish the proton-separation energy, S_p, of ^{73}Rb. β-delayed proton emission provides a unique method of probing the proton-separation energy.

A β-delayed proton spectrum obtained was for ^{73}Sr, and the previously measured spectra of ^{71}Kr and ^{75}Sr were also measured for comparison. The β-delayed proton spectrum for ^{73}Sr was used to extract the proton-separation energy, S_p, of ^{73}Rb. There is tentative evidence for a low energy proton peak at 1055(90) keV. GEANT4 simulations were performed to account for the β-proton summing effects, yielding a value of -800$\pm$70 keV for the S_p of ^{73}Rb. The proton-separation energy of ^{73}Rb was used in the astrophysical *rp*-process calculations.

For ^{71}Kr a branching ratio of 3.8(1)% was obtained and for ^{75}Sr a branching ratio

of 6.3(6)%, both were found to be in good agreement with previous work. A search for β-delayed proton decays for ^{74}Sr and ^{76}Y was conducted but yielded no results, however the statistics for ^{76}Y were insufficient.

In the present work, the half-lives of several nuclei in this mass region have been measured using the χ^2 method and the Schmidt method. The results, where possible, have been compared to known half-lives in the region and, in general, were found to be in good agreement with previous measurements. To gain a complete picture of the two-proton capture branch for the ^{72}Kr waiting point, a goal of the experiment was to determine the half-life of ^{74}Sr. The half-lives of ^{73}Sr and ^{76}Y have been measured for the first time and the half-life of ^{74}Sr has been measured with higher precision.

The data recorded were used to search for new γ decaying isomers in the region. No new isomers were discovered, however, the lifetimes of several known isomers were remeasured and found to agree well with the values in the literature. Measurements of known lifetimes include the 534.8-keV γ ray in ^{69}Se using the Schmidt method was found to be 1400(20) ns and using exponential decay = 1389(20) ns. The mean-lifetime of the state decaying via the 39.4-keV γ ray in ^{69}Se was measured to be 2.9(1) μ. Also, γ-rays in ^{73}Kr resulting from the decay of the known 433.6-keV $9/2^+$ isomer were observed. The mean lifetime of the isomeric state in ^{73}Kr was obtained from a weighted average of the fit of the two transitions and was determined to be 156(31) ns. During the study of the isomeric decay of ^{73}Kr a new transition was observed at 102.7-keV.

To probe the proton drip-line, a search for new isotopes ^{75}Y and ^{77}Z was conducted, and to study the nature of the decay of ^{76}Y. The location of the drip-line is important interest for the *rp*-process. The experiment yielded one count of ^{77}Zr observed in BigRIPS, but there were no counts of ^{75}Y. The experiment yielded 14 observed counts of ^{72}Rb. An estimate of the half-life and an upper limit of the half-life for ^{72}Rb and ^{73}Rb, respectively were calculated. Based on these results, proton emission calculations were performed by L.S. Ferreria and E. Maglione and discussed in this work. The proton emission calculations were performed using a non-adiabatic quasi-particle model for ^{72}Rb and ^{73}Rb. The upper limit of $\sim$70 ns for ^{73}Rb, could be satisfied for a proton in a $1/2^-$ or $3/2^-$ state with a proton energy higher than 550 keV, assuming there is no change in the sign of the deformation between parent and daughter states involved in the decay. This is in good agreement with the AME2012 prediction of -570(100) keV [157].

In the case of ^{72}Rb, AME2012 predicted a larger value: -920(520) keV for the proton-

separation energy [157]. The error is very large, but if one assumes that the energy is 920 keV and without the change of sign in deformation, the only possibility seems to be the $g_{9/2}$ state, however there would be a very small spectroscopic factor, which is unlikely. If the decay is from the ground state to an excited state, this would lower the energy whilst if the decay is from an excited state, then the energy of the proton would increase. Since the error in the AME2012 [157] prediction is very large, for smaller energies, one could reproduce the half-life of 77(21) ns with $\nu f_{5/2} x \pi\ f_{5/2}$ (5+) state or a $\nu g_{9/2} x \pi\ g_{9/2}$ within a certain deformation range for ^{72}Rb.

This work investigated the impact of the new half-lives obtained for ^{73}Sr and ^{76}Y, and the higher precision half-live of ^{74}Sr, and the S_p of ^{73}Rb on the network calculations for the astrophysical *rp*-process. For the *rp*-process to proceed closer to the proton drip-line the S_p for ^{76}Y would need a proton-separation energy of ∼1 MeV, whilst for ^{77}Zr, the S_p would have to be ∼1.25 MeV. By varying the ^{74}Sr half-life between 10-100 ms as function of the S_p of ^{73}Rb, the effective lifetime of ^{72}Kr changed by about 10%. However, as ^{73}Sr and ^{76}Y are not populated in this network calculations under these conditions, the new half-lives have no effect. For the initial conditions in this X-ray burst simulation, the proton-separation energies and half-lives determined in this work, that the abundance distribution and the uncertainties in proton-separation energy in these measurement are negligible. Therefore, to conclude, one can neglect the two-proton capture through ^{72}Kr in calculating the abundances and light-curves for this type of X-ray burst. The nuclide ^{72}Kr remains, therefore, a strong waiting point in the *rp*-process during X-ray bursts delaying energy generation with at least 80% of its β-decay half-life and the path does not bypass the ^{72}Kr branch with two-proton capture.

The mass region of A = 70–80 is a region of highly deformed nuclei, which makes the theoretical prediction of masses difficult. Above ^{64}Ge there are limited experimental mass data available. To improve the accuracy of *rp*-process calculations mass measurements to a precision of about 100 keV are crucial.

8.1 Future work

Further work on the ^{73}Sr β-delayed proton spectrum is needed to further constrain the proton-separation energy, S_p, of ^{73}Rb. An investigation into β-delayed proton spectrum for ^{76}Y is needed, as the low statistics in this work could not yield a definite answer. This would further the knowledge for future network calculations. An experiment to further

investigate the β-delayed proton spectrum of ^{73}Sr has been approved by JAEA [166].

Further experiments to delineate the location of the proton drip-line in this region are clearly required. The proton-separation energy of ^{76}Y needs to be measured. Moller and Nix [145] predicted $T_{1/2}$=37.8 ms for the β-decay of ^{76}Y and calculated the proton-separation energy S_p=-0.57 MeV. Kaneko *et al.* [87] calculated single-proton-separation energies of ^{76}Y to be -0.61 MeV from shell-model calculations using the JUN45 shell-model effective interactions. This work measured the half-life to be $T_{1/2}= 24^{+12}_{-6}$ ms.

There is a need to further investigate the nature of ^{72}Rb and to measure the proton-separation energy, this is crucial for proton emission calculations and for *rp*-calculations. A search into the nature of ^{72}Sr is needed, to constrain the proton-separation energy of ^{72}Rb.

The nature of the ground state in the daughter of ^{72}Rb, ^{71}Kr, is needed to determine if it is $1/2^-$ or the $5/2^-$ state. An investigation of excited states of ^{71}Kr could provide the necessary additional information.

For ^{70}Kr, which should have been used for the core in the proton emission calculations, the 0^+ state is unknown. The 2^+ and 4^+ states are currently being investigated as part of another thesis.

Abbreviations

ADC Analog-to-Digital Converter

AME Atomic Mass Evaluation

AWE Audi-Wapstra extrapolation

BCS Bardeen-Cooper-Schrieffer

BigRIPS Big RIKEN Projectile Fragment Separator

CED Coulomb Energy Differences

CFD Constant-Fraction-Discriminator

DAQ Data Acquisition system

DGF Digital Gamma Finder

DSSSDs Double-Sided Silicon-Strip Detectors

EURICA EUroball at RIken Cluster Array

FRDM Finite-Range Drop Model

fRC Fixed-frequency Ring Cyclotron

HCNO hot CNO

HPGe High-Purity Germanium detectors

IAS Isobaric Analogue States

IRC Intermediate-stage Ring Cyclotron

ISOL Isotope Separation On Line

MUSIC Multi-Sampling Ionisation Chamber

PID Particle Identification

PPAC Parallel Plate Avalanche Counters

RI Radioactive Isotope

RIB Radioactive Ion Beams

RIBF Radioactive Isotope Beam Factory

RILAC2 RIKEN Heavy Ion LINAC 2

RRC RIKEN Ring Cyclotron

RTDs Room-Temperature Dipoles

SC-ECR Superconducting Electron Cyclotron Resonance

SP Single-Particle

STQs Superconducting Triplet Quadrupoles

SRC Superconducting Ring Cyclotron

TDC Time-to-Digital-Converter

TDCs short-range-TDC

TDCl long-range-TDC

TFA Timing-Filter-Amplifer

ToF Time-of-Flight

WAS3ABi Wide-range Active Silicon-Strip Stopper Array for Beta and ion detection

WKB Wentzel-Kramers-Brillouin

ZDS Zero Degree Separator

References

[1] M. Thoennessen, "Reaching the limits of nuclear stability," Reports on Progress in Physics **67**, 1187 (2004).

[2] N. Tajima and N. Suzuki, "Prolate dominance of nuclear shape caused by a strong interference between the effects of spin-orbit and l^2 terms of the Nilsson potential," Phys. Rev. C **64**, 037301 (2001).

[3] M. Bender, P. Bonche, and P.-H. Heenen, "Shape coexistence in neutron-deficient Kr isotopes: Constraints on the single-particle spectrum of self-consistent mean-field models from collective excitations," Phys. Rev. C **74**, 024312 (2006).

[4] E. Clément *et al.*, "Shape coexistence in neutron-deficient krypton isotopes," Phys. Rev. C **75**, 054313 (2007).

[5] M. Hasegawa, K. Kaneko, T. Mizusaki, and Y. Sun, "Phase transition in exotic nuclei along the line," Physics Letters B **656**, 51 (2007).

[6] W. Nazarewicz, J. Dudek, R. Bengtsson, T. Bengtsson, and I. Ragnarsson, "Microscopic study of the high-spin behaviour in selected A = 80 nuclei," Nuclear Physics A **435**, 397 (1985).

[7] P. Möller, A. Sierk, T. Ichikawa, and H. Sagawa, "Nuclear ground-state masses and deformations: Frdm (2012)," Atomic Data and Nuclear Data Tables **109**, 1 (2016).

[8] P. Van Duppen, "The euroschool lectures on physics with exotic beams, Vol. II," , 37 (2006).

[9] M. Bernas *et al.*, "Projectile fission at relativistic velocities: a novel and powerful source of neutron-rich isotopes well suited for in-flight isotopic separation," Physics Letters B **331**, 19 (1994).

[10] W. Mittig, A. Lèpine-Szily, and N. A. Orr, "Mass measurement far from stability," Annual Review of Nuclear and Particle Science **47**, 27 (1997).

[11] W. Heisenberg, "über den bau der atomkerne. i," Zeitschrift für Physik **77**, 1 (1932).

[12] E. Wigner, "On the consequences of the symmetry of the nuclear hamiltonian on the spectroscopy of nuclei," Phys. Rev. **51**, 106 (1937).

[13] M. Bentley and S. Lenzi, "Coulomb energy differences between high-spin states in isobaric multiplets," *Progress in Particle and Nuclear Physics, Vol 59, No 2*, , 497 (2007).

[14] J. Bardeen, L. N. Cooper, and J. R. Schrieffer, "Theory of superconductivity," Phys. Rev. **108**, 1175 (1957).

[15] A. L. Goodman, "Proton-neutron pairing in $Z = N$ nuclei with A =76 − 96," Phys. Rev. C **60**, 014311 (1999).

[16] B. Cederwall *et al.*, "Evidence for a spin-aligned neutron-proton paired phase from the level structure of ^{92}Pd," Nature **469**, 68 (2011).

[17] B. S. Nara Singh *et al.*, "16^+ spin-gap isomer in ^{96}Cd," Phys. Rev. Lett. **107**, 172502 (2011).

[18] B. S. Nara Singh *et al.*, "Influence of the *np* interaction on the β decay of ^{94}Pd," Phys. Rev. C **86**, 041301 (2012).

[19] A. V. Afanasjev and S. Frauendorf, "Description of rotating $N = Z$ nuclei in terms of isovector pairing," Phys. Rev. C **71**, 064318 (2005).

[20] K. Kaneko and M. Hasegawa, "Competition between isoscalar and isovector pairing correlations in $N = Z$ nuclei," Phys. Rev. C **69**, 061302 (2004).

[21] K. Krane, *Introductory Nuclear Physics* (Wiley, 1987).

[22] G. R. Choppin, J.-O. Liljenzin, and J. Rydberg, *Radiochemistry and Nuclear Chemistry (Third Edition)*, third edition ed. (Butterworth-Heinemann, Woburn, 2002).

[23] A. Bohr, B. R. Mottelson, and D. Pines, "Possible analogy between the excitation spectra of nuclei and those of the superconducting metallic state," Phys. Rev. **110**, 936 (1958).

[24] A. Lemasson *et al.*, "Observation of mutually enhanced collectivity in self-conjugate $^{\mathbf{76}}_{\mathbf{38}}\mathrm{Sr}_{\mathbf{38}}$," Phys. Rev. C **85**, 041303 (2012).

[25] A. M. Hurst *et al.*, "Measurement of the sign of the spectroscopic quadrupole moment for the 2_1^+ state in ^{70}Se: No evidence for oblate shape," Phys. Rev. Lett. **98**, 072501 (2007).

[26] K. Heyde and J. L. Wood, "Shape coexistence in atomic nuclei," Rev. Mod. Phys. **83**, 1467 (2011).

[27] A. Görgen and W. Korten, "Coulomb excitation studies of shape coexistence in atomic nuclei," Journal of Physics G: Nuclear and Particle Physics **43**, 024002 (2016).

[28] J. H. Hamilton, A. V. Ramayya, W. T. Pinkston, R. M. Ronningen, G. Garcia-Bermudez, H. K. Carter, R. L. Robinson, H. J. Kim, and R. O. Sayer, "Evidence for coexistence of spherical and deformed shapes in ^{72}Se," Phys. Rev. Lett. **32**, 239 (1974).

[29] E. Bouchez *et al.*, "New shape isomer in the self-conjugate nucleus ^{72}Kr," Phys. Rev. Lett. **90**, 082502 (2003).

[30] W. Nazarewicz, J. Erler, N. Birge, E. Kortelainen, E. Olsen, A. Perhac, and M. Stoitsov, "The limits of the nuclear landscape," Nature **486** (2012).

[31] S. Hofmann, W. Reisdorf, G. Münzenberg, F. P. Heßberger, J. R. H. Schneider, and P. Armbruster, "Proton radioactivity of ^{151}Lu," Zeitschrift für Physik A Atoms and Nuclei **305**, 111.

[32] O. Klepper, T. Batsch, S. Hofmann, R. Kirchner, W. Kurcewicz, W. Reisdorf, E. Roeckl, D. Schardt, and G. Nyman, "Direct and beta-delayed proton decay of very neutron-deficient rare-earth isotopes produced in the reaction ^{58}Ni+^{92}Mo," Zeitschrift für Physik A Atoms and Nuclei **305**, 125.

[33] M. Pfützner, M. Karny, L. V. Grigorenko, and K. Riisager, "Radioactive decays at limits of nuclear stability," Rev. Mod. Phys. **84**, 567 (2012).

[34] B. Blank and M. Borge, "Nuclear structure at the proton drip line: Advances with nuclear decay studies," Progress in Particle and Nuclear Physics **60**, 403 (2008).

[35] I. Čeliković *et al.*, "New isotopes and proton emitters crossing the drip line in the vicinity of ^{100}Sn," Phys. Rev. Lett. **116**, 162501 (2016).

[36] R. J. Carroll *et al.*, "Blurring the boundaries: Decays of multiparticle isomers at the proton drip line," Phys. Rev. Lett. **112**, 092501 (2014).

[37] H. Schatz, "Radioactive nuclei on accreting neutron stars," Nuclear Physics A **746**, 347 (2004), proceedings of the Sixth International Conference on Radioactive Nuclear Beams (RNB6).

[38] J. Grindlay, H. Gursky, H. Schnopper, D. R. Parsignault, J. Heise, A. C. Brinkman, and J. Schrijver, "Discovery of intense X-ray bursts from the globular cluster NGC 6624," Astrophysical Journal **205**, L127 (1976).

[39] R. D. Belian, J. P. Conner, and W. D. Evans, "The discovery of X-ray bursts from a region in the constellation Norma," Astrophysical Journal **206**, L135 (1976).

[40] S. E. Woosley and R. E. Taam, "Gamma-ray bursts from thermonuclear explosions on neutron stars," Nature **263**, 101 (1976).

[41] T. Strohmayer and L. Bildsten, "New views of thermonuclear bursts," in *Compact stellar X-ray sources*, edited by W. H. G. Lewin and M. van der Klis (2006) pp. 113–156.

[42] H. Schatz and K. E. Rehm, "X-ray binaries," Nucl. Phys. **A777**, 601 (2006).

[43] A. Parikh, J. José, G. Sala, and C. Iliadis, "Nucleosynthesis in Type I X-ray bursts," Progress in Particle and Nuclear Physics **69**, 225 (2013).

[44] H. Schatz *et al.*, "*rp*-process nucleosynthesis at extreme temperature and density conditions," Physics Reports **294**, 167 (1998).

[45] D. A. Hardy, "Astroart," (2013), [Online; accessed November-2015.].

[46] N. N. Weinberg, L. Bildsten, and H. Schatz, "Exposing the nuclear burning ashes of radius expansion Type I X-ray bursts," Astrophys. J. **639**, 1018 (2006).

[47] T. Shutt, "Private communication," .

[48] S. E. Woosley, A. Heger, A. Cumming, R. D. Hoffman, J. Pruet, T. Rauscher, J. L. Fisker, H. Schatz, B. A. Brown, and M. Wiescher, "Models for Type I X-ray bursts

with improved nuclear physics," The Astrophysical Journal Supplement Series **151**, 75 (2004).

[49] H. Schatz, A. Aprahamian, V. Barnard, L. Bildsten, A. Cumming, M. Ouellette, T. Rauscher, F.-K. Thielemann, and M. Wiescher, "End point of the *rp* process on accreting neutron stars," Phys. Rev. Lett. **86**, 3471 (2001).

[50] A. Aprahamian and Y. Sun, "Nuclear physics: Long live isomer research," Nature Physics **1**, 81 (2005).

[51] M. F. Mohar, D. Bazin, W. Benenson, D. J. Morrissey, N. A. Orr, B. M. Sherrill, D. Swan, J. A. Winger, A. C. Mueller, and D. Guillemaud-Mueller, "Identification of new nuclei near the proton-drip line for $31 \leq Z \leq 38$," Phys. Rev. Lett. **66**, 1571 (1991).

[52] R. Pfaff, D. J. Morrissey, W. Benenson, M. Fauerbach, M. Hellström, C. F. Powell, B. M. Sherrill, M. Steiner, and J. A. Winger, "Fragmentation of ^{78}Kr projectiles," Phys. Rev. C **53**, 1753 (1996).

[53] I. Piqueras *et al.*, "Beta-decay of the N = Z nucleus ^{72}Kr," The European Physical Journal A - Hadrons and Nuclei **16**, 313 (2003).

[54] A. M. Rogers *et al.*, "Ground-state proton decay of ^{69}Br and implications for the ^{68}Se astrophysical rapid proton-capture process waiting point," Phys. Rev. Lett. **106**, 252503 (2011a).

[55] A. M. Rogers *et al.*, "^{69}Kr β-delayed proton emission: A trojan horse for studying states in proton-unbound ^{69}Br," Phys. Rev. C **84**, 051306 (2011b).

[56] A. Wöhr *et al.*, "The *rp*-process waiting-point nucleus ^{68}Se and its astrophysical implications," Nuclear Physics A **742**, 349 (2004).

[57] M. D. Santo *et al.*, "β-delayed proton emission of ^{69}Kr and the ^{68}Se *rp*-process waiting point," Physics Letters B **738**, 453 (2014).

[58] J. A. Clark *et al.*, "Precise mass measurement of ^{68}Se, a waiting-point nuclide along the *rp* process," Phys. Rev. Lett. **92**, 192501 (2004).

[59] D. Rodríguez *et al.*, "Mass measurement on the *rp*-process waiting point ^{72}Kr," Phys. Rev. Lett. **93**, 161104 (2004).

[60] E. C. Simpson, "Interactive nuclide chart," [Online; 5 January 2016.].

[61] E. Fermi, "Versuch einer Theorie der β-Strahlen. I," Zeitschrift für Physik **88**, 161 (1934).

[62] B. Blank and M. Poszajczak, "Two-proton radioactivity," Reports on Progress in Physics **71**, 046301 (2008).

[63] R. K. Wallace and S. E. Woosley, "Explosive hydrogen burning," The Astrophysical Journal Supplement Series **45**, 389 (1981).

[64] S. Åberg, P. B. Semmes, and W. Nazarewicz, "Spherical proton emitters," Phys. Rev. C **56**, 1762 (1997).

[65] L. S. Ferreira, E. Maglione, and R. J. Liotta, "Nucleon resonances in deformed nuclei," Phys. Rev. Lett. **78**, 1640 (1997).

[66] E. Maglione, L. S. Ferreira, and R. J. Liotta, "Nucleon decay from deformed nuclei," Phys. Rev. Lett. **81**, 538 (1998).

[67] N. N. Bogoljubov, "On a new method in the theory of superconductivity," Il Nuovo Cimento (1955-1965) **7**, 794 (1958).

[68] G. Fiorin, E. Maglione, and L. S. Ferreira, "Theoretical description of deformed proton emitters: Nonadiabatic quasiparticle method," Phys. Rev. C **67**, 054302 (2003).

[69] D. Hodge, "Deformation of the proton emitter ^{113}Cs from electromagnetic transition and proton-emission rates," Phys. Rev. C **Accepted** (2016).

[70] M. J. Taylor *et al.*, "Oblately deformed isomeric proton-emitting state in ^{151}Lu," Phys. Rev. C **91**, 044322 (2015).

[71] L. M. Costa Lopes, L. S. Ferreira and E. Maglione., "Importance of coriolis interaction in deformed proton emitters," International Journal of Modern Physics E **15**, 1789 (2006).

[72] E. Maglione and L. S. Ferreira, "Fine structure in proton emission from deformed ^{131}Eu," Phys. Rev. C **61**, 047307 (2000).

[73] L. S. Ferreira and E. Maglione, "Odd-odd deformed proton emitters," Phys. Rev. Lett. **86**, 1721 (2001).

[74] M. Patial, P. Arumugam, A. K. Jain, E. Maglione, and L. S. Ferreira, "Nonadiabatic quasiparticle approach for deformed odd-odd nuclei and the proton emitter ^{130}Eu," Phys. Rev. C **88**, 054302 (2013).

[75] F.-K. Thielemann, K.-L. Kratz, B. Pfeiffer, T. Rauscher, L. van Wormer, and M. C. Wiescher, "Astrophysics and nuclei far from stabilitys," Nuclear Physics A **570**, 329 (1994).

[76] A. Parikh, J. José, and G. Sala, "Classical novae and Type I X-ray bursts: Challenges for the 21st century," AIP Advances **4**, 041002 (2014), http://dx.doi.org/10.1063/1.4863946.

[77] J.-U. Nabi and M. Böyükata, "β-decay half-lives and nuclear structure of exotic proton-rich waiting point nuclei under rp-process conditions," Nuclear Physics A **947**, 182 (2016).

[78] J. Pruet and G. M. Fuller, "Estimates of stellar weak interaction rates for nuclei in the mass range A = 65-80," The Astrophysical Journal Supplement Series **149**, 189 (2003).

[79] R. H. Cyburt *et al.*, "The jina reaclib database: Its recent updates and impact on type-I X-ray bursts," The Astrophysical Journal Supplement Series **189**, 240 (2010).

[80] T. Rauscher, "Non-smoker code," (2006).

[81] J. C. Batchelder, D. M. Moltz, T. J. Ognibene, M. W. Rowe, R. J. Tighe, and J. Cerny, "Beta-delayed proton decay of ^{73}Sr," Phys. Rev. C **48**, 2593 (1993).

[82] J. Huikari *et al.*, "Mirror decay of ^{75}Sr," Eur. Phys. J. A **16**, 359 (2003).

[83] J. Giovinazzo, P. Dessagne, and C. Mieh, "The delayed proton emission in the A$\sim$65-77 mass region, statistical aspects and structure effects," Nuclear Physics A **674**, 394 (2000).

[84] G. Lorusso, "Private communication," .

[85] B. A. Brown, R. R. C. Clement, H. Schatz, A. Volya, and W. A. Richter, "Proton drip-line calculations and the rp process," Phys. Rev. C **65**, 045802 (2002).

[86] G. Audi, A. Wapstra, and C. Thibault, "The Ame2003 atomic mass evaluation: (II). tables, graphs and references," Nuclear Physics A **729**, 337 (2003), the 2003 {NUBASE} and Atomic Mass Evaluations.

[87] K. Kaneko, Y. Sun, T. Mizusaki, and S. Tazaki, "Variation in displacement energies due to isospin-nonconserving forces," Phys. Rev. Lett. **110**, 172505 (2013).

[88] Y. Yano, "The {RIKEN} {RI} beam factory project: A status report," Nuclear Instruments and Methods in Physics Research Section B: Beam Interactions with Materials and Atoms **261**, 1009 (2007), the Application of Accelerators in Research and Industry Proceedings of the Nineteenth International Conference on The Application of Accelerators in Research and IndustryNineteenth International Conference on The Application of Accelerators in Research and Industry.

[89] H. Okuno, N. Fukunishi, and O. Kamigaito, "Progress of ribf accelerators," Progress of Theoretical and Experimental Physics **2012** (2012), 10.1093/ptep/pts046, http://ptep.oxfordjournals.org/content/2012/1/03C002.full.pdf+html .

[90] "Nishina center for accelerator-based science," (2014), [Online; accessed 22nd September-2014.].

[91] A. S. Nettleton, *A Study of the Fragmentation-Fission of* ^{238}U *on a* ^{9}Be *Target at 81 MeV/u*, Ph.D. thesis, Michigan State University (2011).

[92] T. Kubo *et al.*, "Bigrips separator and zerodegree spectrometer at riken ri beam factory," Progress of Theoretical and Experimental Physics **2012** (2012), 10.1093/ptep/pts064, http://ptep.oxfordjournals.org/content/2012/1/03C003.full.pdf+html .

[93] J. Tapproge, "Private communication," .

[94] N. Fukuda, T. Kubo, T. Ohnishi, N. Inabe, H. Takeda, D. Kameda, and H. Suzuki, "Identification and separation of radioactive isotope beams by the bigrips separator at the {RIKEN} {RI} beam factory," Nuclear Instruments and Methods in Physics Research Section B: Beam Interactions with Materials and Atoms **317, Part B**, 323 (2013), {XVIth} International Conference on ElectroMagnetic Isotope Separators and Techniques Related to their Applications, December 27, 2012 at Matsue, Japan.

[95] T. Kubo, "Nishina center for accelerator-based science," (2013), [Online; accessed March-2013.].

[96] G. Zhong-yan *et al.*, "The separation techniques for secondary beams at ribll," Acta Physica Sinica (Overseas Edition) **8**, 21 (1999).

[97] H. Kumagai, A. Ozawa, N. Fukuda, K. Sümmerer, and I. Tanihata, "Delay-line {PPAC} for high-energy light ions," Nuclear Instruments and Methods in Physics Research Section A: Accelerators, Spectrometers, Detectors and Associated Equipment **470**, 562 (2001).

[98] R. Schneider and A. Stolz, *Technical Manual Ionization Chamber MUSIC80*, Tech. Rep. (Technical report, Technische Universität München, 2000).

[99] P.-A. Söderström *et al.*, "Installation and commissioning of {EURICA} euroball-riken cluster array," Nuclear Instruments and Methods in Physics Research Section B: Beam Interactions with Materials and Atoms **317, Part B**, 649 (2013), {XVIth} International Conference on ElectroMagnetic Isotope Separators and Techniques Related to their Applications, December 27, 2012 at Matsue, Japan.

[100] S. Nishimura, "Beta-gamma spectroscopy at ribf," Progress of Theoretical and Experimental Physics **2012** (2012), 10.1093/ptep/pts078, http://ptep.oxfordjournals.org/content/2012/1/03C006.full.pdf+html .

[101] "The E(U)RICA project," Letter of Intent Submitted to the Gammapool Owners Committee .

[102] S. Nishimura, RIKEN Accelerator Progress Report **46** (2013).

[103] S. Nishimura and J. Wu, "Private communication," .

[104] S. Nishimura, RIKEN Accelerator Progress Report **41** (2008).

[105] O. Tarasov and D. Bazin, "Lise++: Radioactive beam production with in-flight separators," Nuclear Instruments and Methods in Physics Research Section B: Beam Interactions with Materials and Atoms **266**, 4657 (2008), proceedings of the {XVth} International Conference on Electromagnetic Isotope Separators and Techniques Related to their Applications.

[106] H. Baba, T. Ichihara, T. Ohnishi, S. Takeuchi, K. Yoshida, K. Watanabe, S. Ohta, and S. S, RIKEN Accel. Progr. Rep. **43** (2009).

[107] H. Baba, T. Ichihara, T. Ohnishi, S. Takeuchi, K. Yoshida, Y. Watanabe, S. Ota, and S. Shimoura, "New data acquisition system for the {RIKEN} radioactive isotope beam factory," Nuclear Instruments and Methods in Physics Research Section A: Accelerators, Spectrometers, Detectors and Associated Equipment **616**, 65 (2010).

[108] H. G. Essel and N. Kurz, "The general purpose data acquisition system mbs," IEEE Transactions on Nuclear Science **47**, 337 (2000).

[109] H. G. Essel, J. Hoffmann, N. Kurz, R. S. Mayer, W. Ott, and D. Schall, "The new data acquisition system at gsi," IEEE Transactions on Nuclear Science **43**, 132 (1996).

[110] Z. Y. Xu, *Beta-decay spectroscopy on neutron-rich nuclei in a range of Z=26–32*, Ph.D. thesis, University of Tokyo (2014).

[111] R. Brun and F. Rademakers, "{ROOT} an object oriented data analysis framework," Nuclear Instruments and Methods in Physics Research Section A: Accelerators, Spectrometers, Detectors and Associated Equipment **389**, 81 (1997), new Computing Techniques in Physics Research V.

[112] J. Adamczewski-Musch, M.Al-Turany, D.Bertini, H.G.Essel, S.Linev, "The go4 analysis framework introduction v4.6," (2013), [Online; 18 May 2016.].

[113] T. Isobe, "Ribfdaq tools/analysis/anaroot," (2013), [Online; 18 May 2016.].

[114] H. Suzuki, "Private communication," .

[115] J. Taprogge, *Decay Spectroscopy of Neutron-Rich Cadmium Isotopes*, Ph.D. thesis, Universidad Autonoma de Madrid (2015).

[116] Z. Y. Xu *et al.*, "β-decay half-lives of ^{76,77}Co, ^{79,80}Ni, and ^{81}Cu: Experimental indication of a doubly magic ^{78}Ni," Phys. Rev. Lett. **113**, 032505 (2014).

[117] J. Wu, "92 β-decay half-lives of neutron-rich $_{55}$Cs to $_{67}$Ho: Experimental feedback and evaluation of the r-process rare-earth peak formation," (2016).

[118] Z. Podolyák, P. Regan, P. Walker, M. Caamáno, K. Gladnishki, J. Gerl, M. Hellström, P. Mayet, M. Pfützner, and M. Mineva, "Heavy nuclei studied in projectile fragmentation," Nuclear Physics A **722**, C273 (2003).

[119] K. H. Schmidt, C. C. Sahm, K. Pielenz, and H. G. Clerc, "Some remarks on the error analysis in the case of poor statistics," Zeitschrift für Physik A Atoms and Nuclei **316**, 19.

[120] K. H. Schmidt, "A new test for random events of an exponential distribution," Eur. Phys. J. A **8**, 141 (2000).

[121] H. Bateman, Cambr. Phil Soc. Proc. **423** (1910).

[122] J. Cetnar, "General solution of bateman equations for nuclear transmutations," Annals of Nuclear Energy **33**, 640 (2006).

[123] J. Berkson, "Minimum chi-square, not maximum likelihood!" Ann. Statist. **8**, 457 (1980).

[124] F. James and M. Roos., *MINUIT, function minimization and error analysis.* (CERN D506 (Long Writeup).).

[125] K. Gregorich, "Maximum likelihood decay curve fits by the simplex method," Nuclear Instruments and Methods in Physics Research Section A: Accelerators, Spectrometers, Detectors and Associated Equipment **302**, 135 (1991).

[126] R. J. Barlow, *A Guide to the Use of Statistical Methods in the Physical Sciences* (Wiley, 1989).

[127] R. J. Barlow, "A note on delta ln l=-1/2 errors," arXiv preprint physics/0403046 (2004).

[128] K. R. Pohl, D. F. Winchell, J. W. Arrison, and D. P. Balamuth, "Isomeric transitions in ^{69}Se and the spin of the ground state," Phys. Rev. C **51**, 519 (1995).

[129] R. H. Burch, C. A. Gagliardi, and R. E. Tribble, "Lifetimes of N=Z nuclei ^{66}As and ^{70}Br," Phys. Rev. C **38**, 1365 (1988).

[130] B. O. ten Brink, R. D. Vis, A. W. B. Kalshoven, and H. Verheul, "The decay of $^{70}_{33}Se_{37}$," Zeitschrift für Physik **270**, 83 (1974).

[131] P. Kienle *et al.*, "Synthesis and half lives of heavy nuclei relevant for the *rp*-process," Progress in Particle and Nuclear Physics **46**, 73 (2001).

[132] T. Faestermann *et al.*, "Decay studies of N = Z nuclei from ^{75}Sr to ^{102}Sn," The European Physical Journal A - Hadrons and Nuclei **15**, 185 (2002).

[133] E. Wefers *et al.*, "Decay properties of the heaviest N $\sim$ Z nuclei," (2007), preprint.

[134] M. Oinonen *et al.*, "β decay of the proton-rich $T_z = -1/2$ nucleus, ^{71}Kr," Phys. Rev. C **56**, 745 (1997).

[135] E. Hagberg, J. Hardy, H. Schmeing, H. Evans, U. Schrewe, V. Koslowsky, K. Sharma, and E. Clifford, "The decay of a new nuclide: ^{71}Br," Nuclear Physics A **383**, 109 (1982).

[136] G. C. Ball *et al.*, "Precise half-life measurement for the superallowed $0^+ \rightarrow 0^+$ β emitter ^{74}Rb: First results from the new radioactive beam facility (ISAC) at TRIUMF," Phys. Rev. Lett. **86**, 1454 (2001).

[137] H. Schmeing, J. Hardy, R. Graham, and J. Geiger, "The decay of ^{74}Kr," Nuclear Physics A **242**, 232 (1975).

[138] B. D. Kern, K. S. Toth, D. M. Moltz, J. Lin, F. T. Avignone, H. Noma, and G. A. Leander, "Beta decay of ^{75}Rb to low-lying levels in ^{75}Kr," Phys. Rev. C **28**, 2168 (1983).

[139] J. D'Auria, L. Carraz, P. Hansen, B. Jonson, S. Mattsson, H. Ravn, M. Skarestad, and L. Westgaard, "The N = Z nuclide ^{74}Rb with T, Iπ = 1, 0^+," Physics Letters B **66**, 233 (1977).

[140] D. D. Bogdanov, I. Voborzhil, A. V. Demyanov, V. A. Karnaukhov, and L. A. Petrov, "Decay of ^{75}Rb and ^{76}Rb," Izv.Akad.Nauk **SSSR**, Ser.Fiz. 39, 2029 (1975).

[141] H. Ravn, S. Sundell, L. Westgaard, and E. Roeckl, "Short-lived isotopes of alkali and alkaline-earth elements studied by on-line isotope separator techniques," Journal of Inorganic and Nuclear Chemistry **37**, 383 (1975).

[142] B. Blank *et al.*, "New isotopes from ^{78}Kr fragmentation and the ending point of the astrophysical rapid-proton-capture process," Phys. Rev. Lett. **74**, 4611 (1995).

[143] J. Henderson *et al.*, "Spectroscopy on the proton drip-line: Probing the structure dependence of isospin nonconserving interactions," Phys. Rev. C **90**, 051303 (2014).

[144] J. A. Winger, D. Bazin, W. Benenson, M. F. Mohar, D. J. Morrissey, N. A. Orr, B. M. Sherrill, D. Swan, A. C. Mueller, and D. Guillemaud-Mueller, "Identification of new nuclei near the proton-drip line for 31 $\leq$ Z $\leq$ 38," Bull.Am.Phys.Soc. **36**, No.4, 1333, I10 12 (1991).

[145] P. Moller, J. Nix, and K.-L. Kratz, "Nuclear properties for astrophysical and radioactive-ion-beam applications," Atomic Data and Nuclear Data Tables **66**, 131 (1997).

[146] J. Henderson, *Decay tagging of neutron-deficient* ^{73,74}*Sr*, Ph.D. thesis, University of York (2014).

[147] D. Jenkins, Private communication.

[148] S. Agostinelli *et al.*, "Geant4a simulation toolkit," Nuclear Instruments and Methods in Physics Research Section A: Accelerators, Spectrometers, Detectors and Associated Equipment **506**, 250 (2003).

[149] N. Warr, A. Blazhev, and K. Moschner, "Simulations of the simba array towards the determination of Qβ values," EPJ Web of Conferences **93**, 07008 (2015).

[150] S. Freund *et al.*, "Identification of excited levels in the N=Z+1 nucleus ^{73}Kr," Physics Letters B **302**, 167 (1993).

[151] C. Chandler *et al.*, "Observation of isomeric states in neutron deficient $A \sim 80$ nuclei following the projectile fragmentation of ^{92}Mo," Phys. Rev. C **61**, 044309 (2000).

[152] M. Satteson *et al.*, "Identification of transitions in ^{73}Kr and the search for large oblate deformation," Journal of Physics G: Nuclear and Particle Physics **16**, L27 (1990).

[153] S. M. Fischer, T. Anderson, P. Kerns, G. Mesoloras, D. Svelnys, C. J. Lister, D. P. Balamuth, P. A. Hausladen, and D. G. Sarantites, "Shape coexistence in ^{71}Br and the question of the ground-state spin of ^{71}Kr," Phys. Rev. C **72**, 024321 (2005).

[154] D. Jenkins, "Waiting points in the astrophysical rp process: how unbound are ^{69}Br and ^{73}Rb?" Physical Review C **78**, 1 (2008), 2008 The American Physical Society.

[155] N. S. Kelsall *et al.*, "Testing mean-field models near the $N = Z$ line: γ-ray spectroscopy of the $T_z = \frac{1}{2}$ nucleus ^{73}Kr," Phys. Rev. C **65**, 044331 (2002).

[156] H. Suzuki *et al.*, "Production cross section measurements of radioactive isotopes by BigRIPS separator at RIKEN RI Beam Factory," *Proceedings, 16th International Conference on Electromagnetic Isotope Separators and Techniques Related to their Applications (EMIS 2012)*, Nucl. Instrum. Meth. **B317**, 756 (2013), 1310.5945 .

[157] G. Audi, M. Wang, A. Wapstra, F. Kondev, M. MacCormick, X. Xu, and B. Pfeiffer, "The Ame2012 atomic mass evaluation," Chinese Physics C **36**, 1287 (2012).

[158] C. J. Gallagher and S. A. Moszkowski, "Coupling of angular momenta in odd-odd nuclei," Phys. Rev. **111**, 1282 (1958).

[159] L. S. Ferreira, E. Maglione, and D. E. P. Fernandes, "Dependence of the decay widths for proton emission on the single particle potential," Phys. Rev. C **65**, 024323 (2002).

[160] G. de Angelis *et al.*, "Coulomb energy differences between isobaric analogue states in ^{70}Br and ^{70}Se," Eur. Phys. J. A **12**, 51 (2001).

[161] A. Parikh, J. José, F. Moreno, and C. Iliadis, "The sensitivity of nucleosynthesis in Type I X-ray bursts to thermonuclear reaction-rate variations," New Astronomy Reviews **52**, 409 (2008a).

[162] A. Parikh, J. José, F. Moreno, and C. Iliadis, "The effects of variations in nuclear processes on Type I X-ray burst nucleosynthesis," The Astrophysical Journal Supplement Series **178**, 110 (2008b).

[163] B. S. Meyer, "Nucnet tools," (2011), [Online; 18 January 2015.].

[164] P. Möller, W. D. Myers, H. Sagawa, and S. Yoshida, "New finite-range droplet mass model and equation-of-state parameters," Phys. Rev. Lett. **108**, 052501 (2012).

[165] H. Schatz, "The importance of nuclear masses in the astrophysical rp-process," International Journal of Mass Spectrometry **251**, 293 (2006).

[166] D. Jenkins, Private communication.